Università Roma Tre

Dipartimento Scienze Geologiche

Scuola Dottorale in Geologia dell'Ambiente e Geodinamica

XXII ciclo

Emplacement temperature and flow direction analysis of large dimension calderas ignimbrites: the Cerro Galán and Toconquis Group ignimbrites (Puna plateau, NW Argentina)

Candidata: Chiara Lesti

Tutor: Massimo Mattei

Co-tutor: Guido Giordano

1. Abstract

Estimates of pyroclastic flow emplacement temperatures in the Cerro Galàn ignimbrite and Toconquis Group ignimbrites and flow directions were determined using thermal remanent magnetization (TRM) of lithic clasts embedded within the deposits and the anisotropy of magnetic susceptibility, respectively. These ignimbrites belong to the Cerro Galàn volcanic system, one of the largest calderas in the world, in the Puna plateau, NW Argentina.

Temperature estimates for the 2.16 ± 0.16 Ma Cerro Galán ignimbrite are retrieved from 40 sites in 14 localities (176 measured clasts), distributed at different distances from the caldera and different stratigraphic heights. Additionally, temperature estimates were obtained from 27 sample sites (125 measured clasts) in seven ignimbrite units forming the older Toconquis Group (5.60±0.20 - 4.51±0.11 Ma), mainly outcropping along a type-section at Rio Las Pitas, Vega Real Grande.

Flow directions are defined in 35 sites (403 measures specimens), distributed again at different distances and azimuth from the caldera and at different stratigraphic heights along the same section. The flow direction assessment was carried out on the Cerro Galàn ignimbrite and not on the older units, as the outcrops of the Toconquis Group are limited in extension mainly to the west of the caldera.

The paleomagnetic data obtained by progressive thermal demagnetization (PTD), show that most of the clasts of the Cerro Galán ignimbrite have one single magnetic component, oriented close to the expected geomagnetic field at the time of emplacement. Results show therefore that most of the clasts acquired a new magnetization oriented parallel to the magnetic field at the moment of the ignimbrite deposition, suggesting that the clasts were heated up to or above the highest blocking temperature (T_b) of the magnetic minerals (T_b=580°C for magnetite; T_b=600-630°C for titano-hematite).

We obtained similar emplacement temperature estimations for five out of six volcanic units belonging to the Toconquis Group, with the exception of one unit (Lower Merihuaca), where we found two distinct magnetic components. The estimation of emplacement temperatures in this latter case is constrained between 580°-610°C.

The study of the AMS was performed in order to analyse the ignimbrite fabric and to evaluate the flow structure and emplacement mechanism, relating the magnetic fabric to the paleotopography.

Flow directions are defined in 35 sites (403 measures specimens), distributed at different distances and azimuth from the caldera and at different stratigraphic heights along the same

section. The comparison of magnetic fabric with mineralogical fabric is also examined to assess the reliability of the AMS as flow direction indicator.

AMS results show a strong uniformity throughout the ignimbrite, with the exception of sites where the topographic control on the emplacement mechanism is higher. Flow directions results show a radial pattern around the caldera, in proximal sites, while in distal sites the directions are deflected by the paleotopography.

The strong control of the paleotopography revealed in this study, together with field evidences of low level of turbulence and high emplacement temperatures estimation found, indicate that the flow was highly concentrated throughout the flow path.

We conclude that the Cerro Galán ignimbrite and Toconquis Group ignimbrites were emplaced at temperatures equal to or higher than 620°C and that in distal sites the flow, besides having the capacity of travel up to 80 K_m, follows passively the paleotopography. The homogeneity of high temperatures from proximal to distal facies, and the behaviour in presence of topographic obstacles in distal sites, provide constraints for an emplacement model for the Cerro Galán ignimbrite, marked by a relatively low eruption column, low levels of turbulence during deposition, air entrainment, surface-water interaction, and a high level of topographic confinement, all ensuring minimal heat loss and high concentration flow.

2. Introduction

This study is part of an international project focused on the characterization of the facies architecture and of the emplacement processes of the Cerro Galàn Ignimbrite, Argentina, applying paleomagnetic methods and analysis of the magnetic fabric. The Cerro Galán volcanic system (Puna plateau) in northwest Argentina has been the site of at least 9 large to very large volume pyroclastic eruptions over the past 6 Ma (Folkes et al., submitted-a). Sparks et al. (1985) were the first authors to describe the stratigraphy, volcanology and age of these deposits. They recognized that the last ignimbrite, called Cerro Galán ignimbrite (CGI), formed the present caldera and represents the most voluminous eruption of the Cerro Galán volcanic system with the most distal outcrop at ~74 km to the north of the current topographic margin. The older ignimbrite deposits, grouped under the name of Toconquis Group, were likely related to an older caldera (Folkes et al. submitted-a), and have a smaller, though more poorly constrained volume than the Cerro Galán ignimbrite.

These ignimbrites are ideal M8 magnitude ignimbrites to study for a number of factors, above all the arid climate that allows the exposure of nearly continuous outcrop and the

analysis of the evolution of the fabric from proximal to distal sites; the erosion that acted during the last 2 Ma exposed high sections trough the deposit, that is very well preserved.

2.1. Large scale eruptions

Large scale explosive eruptions, producing very large volume pyroclastic flows that rapidly travel to great distances from the eruptive centre (volcanic explosivity index VEI>7) are the most dangerous eruptions.

These eruptions have not been witnessed in historical times and are, therefore, relatively poorly understood. To better understand the emplacement dynamics of these flows, we must therefore either extrapolate from historic observations of small to moderate volume pyroclastic flows, or use indirect measurement techniques and models.

Pyroclastic flows are fluidized mixtures of hot gas, pumices, crystals, rock debris and fine ash, forming variably turbulent flows able to reach far distances at high velocity.

Historical small to intermediate volume pyroclastic flows are known as one of the most destructive natural events, as reported for the 79 AD eruption of Vesuvius, Italy, (Sigurdsson et al. 1985; Cioni et al. 1992), the 1883 eruption at Krakatau, Indonesia (Simkin and Fiske 1983); the 1902 Mt Pelee, Martinique, where 30,000 people were killed (Lacroix 1904; Fisher and Heiken 1982). At Mt St Helens, USA in 1980, 57 persons lost their lives, though the volcano was constantly monitored (Lipman and Mullineaux 1981), as at Mt Unzen, Japan, where a better knowledge of the emplacement behaviour of the 1991 pyroclastic flows could have avoided the 43 people lost.

From the Ordovician to Pleistocene, 47 large volume eruptions are known, of which 42 in the last 36 Ma (Mason et al. 2004). These are M8 events except the one that produced the Fish Canyon Tuff , in the USA, which is an M9 event (Lipman 1997).

The quantification of the magnitude of an eruption is described in literature with different approaches, either on the volume of the deposit (in km^3) or on the mass of erupted tephra (in kg).

One of the most used indexes is the VEI (volcanic explosivity index) by Newhall and Self 1982), which is a semi-quantitative logarithmic scale of eruption size, based on a combination of erupted tephra volume and eruption plume height. On this scale, the largest events (VEI ≥ 8) are defined as eruptions with bulk tephra volumes >1.000 km^3. The magnitude scale M by Pyle 1995) is instead based on the erupted mass. An M8 event, defined as an event with an erupted mass comprised between 10^{15} and 10^{16} kg can vary in volume between 400 and 10.000 km^3, depending on the bulk density of the deposit (which may range from 1.000–2.500 kg m^{-3}).

The last two VEI 8 eruptions reported by Mason et al. 2004) occurred at 74 ka b.p. with the M8.8 eruption of the Younger Toba Tuff from Toba, Sumatra (Rose and Chesner 1987), and at 26.5 ka b.p., with the M8.1 Oruanui eruption, New Zealand (Wilson 2001).
The consequences of events of such scale remain poorly constrained, but the impact on the climate of the Earth may be as severe as a 'volcanic winter' (Rampino and Self 1992).
The understanding of the emplacement mechanism of pyroclastic flows, through the modelling of the transport and the depositional systems, is crucial in terms of risk assessment.

2.2. Transportation and depositional processes in pyroclastic flows

Two main models have been developed on transport and depositional processes in pyroclastic flows on the basis of the direct observation of historical events and on the study of the ignimbrites recorded in the geological record: the *en masse* or *plug flow* model of Sparks 1976), and the *progressive aggradation* model of Fisher 1966) and Branney and Kokelaar 1992; Branney and Kokelaar 2002).
A pyroclastic flow deposit is concordantly divided in three main facies (Sparks et al. 1973): a basal layer 1 that originate from the turbulent front and margins of the flow; the layer 2 which originates from the 'body of the flow', and the uppermost layer 3 originated from the low particle concentration, turbulent, trailing ash cloud. The main ignimbrite may show complex internal vertical and lateral variations, including massive and chaotic divisions, poorly stratified to stratified divisions, as well as normal and reverse grading of both lithic and pumice clasts forming lithic and pumice concentrations zones at various heights.

The two models are concordant on the origin of layer 1 and 3, but are in contrast on the depositional mechanism of the 'body' layer 2.
In the plug flow model the pyroclastic flows are non-turbulent, high-density fluidised flows (Sparks 1976; Miller and Smith 1977; Sparks et al. 1978). As the pyroclastic flow decelerates, it degasses, deflates, causing frictional interlocking of grains, and comes to a stop, more or less at once (Sparks 1976). In this model, the lithic rich layers 2bL and the pumice rich layers 2bP are interpreted as a hydraulic settling of the lithics and at the same time floating of the pumices in the 'body' of the flow. The body of the flow may be turbulent near vent, but in distal regions it is probably laminar. The flow is capable of surmounting topographic obstacles because of it momentum (Sparks et al. 1978) but, as the flow is dense and non turbulent, it would continue as a whole, with no separation between transport and depositional system. The implication of such model is that time lines throughout the deposits are almost vertical, i.e. the earliest erupted material is deposited at the front, whereas the rest progressively at the rear (e.g. Giordano 1998). Given the usual travel-time of pyroclastic

flows (minutes to tens of minutes), large volume ignimbrites necessarily have to originate by a succession of individual events, as incremental (Walker et al. 1995).

In the progressive aggradation model, or expanded flow model, pyroclastic flows are dominantly turbulent, highly dilute and low particle density current (Branney and Kokelaar 1992; Druitt 1992; Druitt 1998). Deposition occurs continuously when particles from the main part of the flow drop into a thin, basal, low velocity, laminar, boundary layer, onto the aggrading depositional surface (Fisher 1966; Branney and Kokelaar 1992; Branney and Kokelaar 2002). The implication of such model is that time lines throughout the deposits are almost subhorizontal, i.e. the earliest erupted material is deposited at the bottom, whereas the rest progressively on top (e.g. Giordano 1998). Given the usual travel-time of pyroclastic flows this model allows for any thickness to be deposited under sustained currents also for large volume ignimbrites. Vertical variations in deposit characteristics such as the normal and reverse grading of lithics and pumices are attributed to changes in flow conditions and in intensity of energy released at the vent. Lithic concentration zones high in an ignimbrite, vertical compositional zonation in juvenile clasts, also support progressive or incremental aggradation. The flow in this model is capable to surmount of topographic barriers because it is thicker than the obstacle (e.g. Fisher et al. 1993). In this setting the flow can decouple, and a higher density strata could develop at the base (Valentine 1987). Topographic obstacles can block the dense basal flow that will move downhill, while the upper, still dilute part of the flow surmounts the topographic obstacle, as documented at the Soufri`ere Hills Volcano, Montserrat (e.g. Cole et al. 1998; Calder et al. 1999).

The underestimation of this phenomenon caused several casualties in the 1991 Mt. Unzen eruption (Nakada and Fujii 1993).

While ignimbrite deposits can only record the very last stage of the depositional stage of a pyroclastic flow, the current approach is to attempt retrieving information from the depositional facies to interpret the fluid dynamics of the flow.

Also along the path, external influence, like the change in the substrate topography, or internal changes in physical parameters like particle concentration, temperature of the gas-particle mixture, fluidization, can modify the rheological behaviour (Freundt and Bursik 2001).

Furthermore, the changes of eruption dynamics, which involve waxing and waning of the eruption rate and of flows, as well as the interplay with the topography may lead to complex progradational and retrogradational phases, resulting in forestepping-backtepping stacking patterns of the internal architecture of ignimbrites (DeRita et al. 1998; Giordano 1998).

2.3. Emplacement temperatures

Determination of pyroclastic flow emplacement temperature can provide a strong constraint on the transport and depositional system (Porreca et al. 2003a; McClelland et al. 2004; Gurioli et al. 2005; Porreca et al. 2006; Giordano et al. 2008). The emplacement temperature of a pyroclastic flow is related to a complex combination of factors such as the initial magmatic temperature, adiabatic decompression, transport path through the atmosphere (including whether the eruption column is buoyant, or boiling-over), adiabatic decompression, and heat loss from the flow during lateral transport (e.g. Bardot, 2000) due to the interaction of the flow with air and water (e.g. Cas and Wright 1987, Branney and Kokelaar 2002).

Conditions at the vent and along flow, such as mass flux and velocity, influence the capability of the flow to entrain air, which in turn, together with the grain size distribution, control the runout distance (Bursik and Woods 1996). The physical parameters on which mobility depends are still debated, but air entrainment (and consequently temperature) is certainly a good candidate, together with eruption rate, grain size distribution, hill slope, and topographic confinement (Bursik and Woods 1996).

The temperature of emplacement of pyroclastic flow deposits therefore represents one of the most important measurable physical parameters, which can be related to the pyroclastic flow mobility, with important implications for hazard assessment.

Paleomagnetic methods represent a reliable tools for determining emplacement temperature in ancient ignimbrites (McClelland et al. 2004). Many studies have been performed applying paleomagnetic methodology, beginning with the pioneering study of Aramaki and Akimoto 1957) that used thermal remanent magnetization (TRM) on the bulk ignimbrite deposit to estimate the emplacement temperature.

The same technique was then extended to lithic clasts incorporated into ignimbrites (Wright 1978; Hoblitt and Kellogg 1979; Kent et al. 1981; McClelland and Druitt 1989; Bardot 2000; Porreca et al. 2003a; McClelland et al. 2004; Porreca et al. 2006) and to pumice clasts (McClelland et al. 2004). Using thermal magnetization of lithic clasts, emplacement temperatures have been estimated for several well-known small to large volume ignimbrites, including the 79 AD eruption of Vesuvius (180-380°C, 7 km from the vent, Cioni et al. 2004; 140-300°C within and around Pompeii, Zanella et al. 2007), the 1630 BC eruption of Santorini (200-≥580°C McClelland and Druitt 1989; 400-≥580°C at 11 km from vent, Bardot 2000), the 1883 AD eruption of Krakatau (475-550°C, subaqueous pyroclastic flow 8 km from the vent; Mandeville et al. 1994), and the 1.8 Ka eruption of Taupo (150-≥580°C at

more than 40 km from vent, McClelland et al. 2004). The lowest reported emplacement temperatures are interpreted to have resulted from interaction with external water (<100°C, McClelland et al. 2004; <140°C, Porreca et al. 2006), air (Cioni et al. 2004) and urban structures (Gurioli et al. 2005, Zanella et al. 2007).

Temperature estimates along the flow path provide additional information about the degree and extent of heat loss along the flow and the extent of flow interaction with external media (water and air). McClelland et al. (2004) estimated equilibrium emplacement temperatures at 400°-500°C for the 1.8 Ka Taupo eruption (bulk volume 30 km^3), up to 50 km from the source. In contrast, in proximal facies less than 30 km from the source, the emplacement temperature was evaluated to be between 150° and 300°C. This variation was interpreted, in combination with field evidence, as being due to be due to interaction of early, proximal flows with lake water that occupied the old caldera depression.

From direct measurements of 1980 Mount St. Helens activity, Banks and Hoblitt 1981) found that the ash cloud temperature dropped initially, while in the ash column, but temperature was largely maintained in the pyroclastic flow. They found an initial drop in temperature of 100°C, from a magmatic temperature of 950°C (Banks and Hoblitt 1981, and references therein) during the first air interaction phase in the convecting column, and a second drop to about 700°C in the first hundreds of meters from the vent. The temperature of the pyroclastic flow then remained constant up to 8 km from the source.

Furthermore, the temperature of the pyroclastic flow at the moment of deposition has also strong influences on post emplacement processes, such as welding. The glassy material, once deposited, may still show ductile behavior that can develop, along a steep topography, features consistent with rheomorphic flows.

The welding process occurs through sintering, compaction and flattening of the pyroclasts, depending on various parameters, which are still in debate. Compositional changes, load of the overlying material, volatile content, grain size population, lithic content are all factors that variably determine the occurrence of welding (e.g. Freundt 1998; Branney and Kokelaar 2002). Quane and Russell (2005) ranked welding intensity in six ranks (I-VI), defined by discrete ranges in physical properties (including porosity, density, point load strength, uniaxial compressive strength, pumice lapilli oblateness and microfabric orientation) and macroscopic and microscopic textural characteristics. Petrographic characteristics vary from the unconsolidated, incoherent ash matrix, with randomly oriented pumice lapilli lacking any deformation of Rank I to the obsidian-like vitrophyre with eutaxitic texture and obsidian like *fiamme* of Rank VI.

Welding structures, being related to ductile behavior of glassy shards, are strongly dependent on glass transition temperature of the materials, and therefore are particularly useful in defining upper-boundary temperature limit for non-welded deposits.

Determination of paleo-emplacement temperatures for very large volume pyroclastic flow deposits, including temperature variations with transport distance, has not yet been determined.

2.4. Magnetic fabric and flow directions

Another strong constraint, besides temperature estimation, on which studies about density currents have been based, is the fabric analysis of the different facies of pyroclastic flow deposits, which may help characterizing the evolution of the pyroclastic flow in space and time.

The fabric of an ignimbrite is therefore related to the sum of various different factors acting during the deposition from a pyroclastic flow, such as the grain size distribution of each component, the density of the gas-particle mixture, the behaviour of the depositional and transport systems and of the boundary layer between them (Cas and Wright 1987; Branney and Kokelaar 1992; Branney and Kokelaar 2002).

The analysis of the magnetic fabric of an ignimbrite, based on the study of the anisotropy of magnetic susceptibility (AMS), is considered a reliable tool as a proxy of the rock fabric (Ellwood 1982; Rochette et al. 1992; Porreca et al. 2003a; Giordano et al. 2008; LaBerge et al. 2008; Pioli et al. 2008). The AMS is related to the anisotropy of the shape and structure of the magnetic crystals or to the spatial arrangement of the crystal. As each analysis is based on samples of 10 cm^3 the results are more representative than a single thin section, less time consuming and allows the fabric analysis in visually isotropic rocks (e.g. Rochette et al. 1992). Anyhow, the direct comparison between the AMS and petrofabric are quite scarce (Rochette et al. 1992; Plenier et al. 2005).

The analysis of the magnetic fabric have been applied on different settings such as on plutons (e.g. Grégoire et al. 1998; Talbot et al. 2000), dykes (Raposo 1997; Rapalini and de Luchi 2000; Aubourg et al. 2002; Porreca et al. 2003a; Porreca et al. 2003b), lava flows (Herrero-Bervera et al. 2002; Cañón-Tapia and Castro 2004), and volcanic avalanches (Schneider and Fisher 1991).

Ignimbrites flow directions are usually determined by measuring the preferred orientation or imbrication of elongate elements carried in the flow itself or picked up along the flow path, such as crystals, lithic fragments or pumices (e.g. Suzuki and Ui 1982; Schmincke and Swanson 1967), welding fabric (Kamata and Mimura 1983) or tree logs orientation (Froggatt

et al. 1981). The use of welding lineation can be misleading in the determination of flow direction as it can be produced by stretching of *fiamme* during secondary mass flowage (e.g. Wright 1980).

In volcanic environment the AMS method have been applied mainly to infer the source of a deposit and in the analysis of flow direction and (Ellwood 1982; Incoronato et al. 1983; Knight et al. 1986; MacDonald and Palmer 1990; Hillhouse and Wells 1991; Seaman et al. 1991; Ort 1993; MacDonald et al. 1998; Ort et al. 1999).

The AMS have been applied also to retrieve information about transport and depositional processes (Fisher et al. 1993; Le Pennec et al. 1998; Palmer and MacDonald 1999; Porreca et al. 2003a; Porreca et al. 2003b; Gurioli et al. 2007; Giordano et al. 2008). Baer et al. (1997) related the ignimbrite directions with respect to topographic obstacles, to the turbulence of the flow and to the coupling between the transport and the depositional system.

In this work are presented the results and implication of the emplacement temperatures and flow directions determination carried out on the Cerro Galàn ignimbrites, NE Argentina. The emplacement temperatures were estimated on the Cerro Galán ignimbrite and on the other older ignimbrites belonging to the Toconquis Group by means of paleomagnetic techniques applied on accessory and/or accidental lithic clasts embedded within the deposits. The thermal structure of these deposits, from proximal to distal locations, and at different stratigraphic heights, were studied in order to constrain the transport and emplacement mechanisms and define the extent of interaction with external “cooling” factors such as the atmosphere, ground water, surface water, and ground surface in an arid environment. Moreover we define the magnetic fabric and the flow directions at various azimuth around the caldera, in proximal and distal sites and at different stratigraphic heights by the analysis of the anisotropy the magnetic susceptibility of the ignimbrite matrix.

Paleomagnetic methodologies are therefore applied to help understand emplacement conditions and transport dynamics in very large volume pyroclastic flows.

3. Geological setting and sedimentological features of the Cerro Galán ignimbrites

The Cerro Galán caldera is one of the largest calderas in the world, with a 38 x 26 km N-S elongated structure, located in the southern margin of the Puna plateau in NW Argentina and ~200 km south of the extensive Altiplano-Puna Volcanic complex (APVC; de Silva 1989) (Fig. 3.1). The caldera lies on a major N-S trending graben fault zone, the Diablillos-Galán Fault Zone (Coira et al. 1993, Kay et al 2008), at the intersection with a major NW trending regional Archibarca lineament (Salfity 1984; Viramonte et al. 1984). The caldera is characterized by a large central resurgent dome that exposes the uplifted intra-caldera Cerro Galán ignimbrite, and several post-ignimbrite lava domes (Sparks et al. 1985).

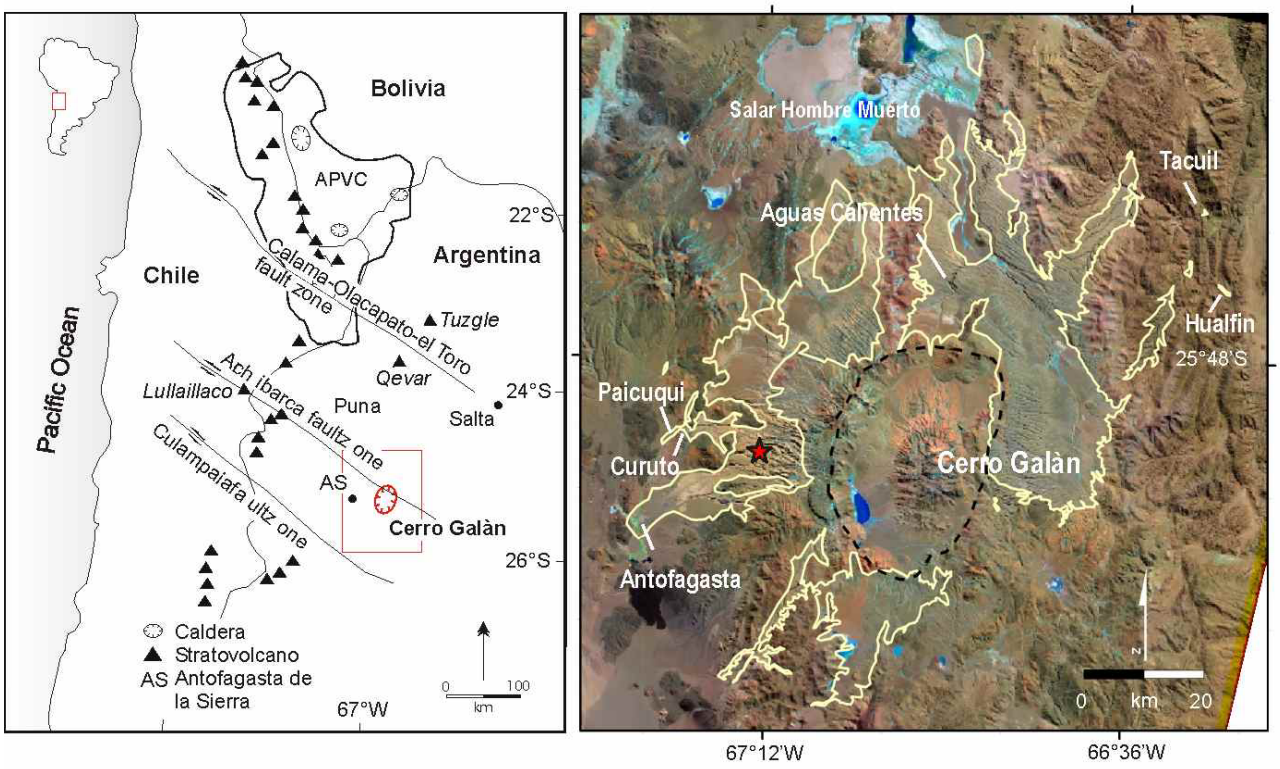

Fig. 3.1 - Location of Cerro Galán caldera in the Puna plateau, north-western Argentina. a) main structural features of central Andes (modified after Riller et al. 2001). APVC: Altiplano Puna Volcanic Complex; b) Cerro Galàn area (enlargement of red square in a). Color composition of Landsat ETM+ (band 7, 4, 2). The Cerro Galàn ignimbrite is contoured in light brown; the black solid lines represent the inferred caldera collapse faults (Folks et al submitted-a); the dashed line follows the topographic caldera rim. Red star: location of Fig. 2a section.

The regional stratigraphy, described in early works by Francis et al. 1983 and Sparks et al. 1985) has been recently revised (Folkes et al. submitted-a) and is summarized in Table 3.1. Nine distinct outflow ignimbrites are recognized, including two newly identified ignimbrite units in the Toconquis Group (the Pitas and Vega ignimbrites).

Early ignimbrites of the Toconquis Group are underlain by fall deposits, whereas the Cerro Galàn ignimbrite is not. The seven ignimbrites belonging to the Toconquis Group (5.60-4.51 Ma), exposed in a 200m section at Rio Las Pitas, Vega Real Grande (Fig. 3.2a) are largely massive and chaotic, ash-matrix supported, crystal-rich (up to 50 vol.%) and generally lithic poor (<5 vol.%), except for the Vega ignimbrite which bear up to 25% of lithics. All the ignimbrites are pumice rich (20-40%), and the Pitas and Real Grande ignimbrites contain pumice concentration zones with individual pumice clasts up to 1m in diameter. All the Toconquis Group ignimbrites lack welding textures. The currently-preserved areal extent of the Toconquis Group ignimbrites is about 260 km^2, with a total volume of 630 km^3 (DRE) inferred by Folkes et al. submitted-a). The highly welded Cueva Negra unit, present only on the eastern flanks of the caldera, is not investigated by this study.

	Ignimbrite	$^{40}Ar/^{39}Ar$ Age
Toconquis Group	Cerro Galan	2.56+-0.05
	Quiescence Period 1.1 Ma	
	Cueva Negra	3.68+-0.08
	Quiescence Period 0.8 Ma	
	Vega	4.51+-0.11
	Real Grande	4.64+-0.08
	Pitas	4.84+-0.04
	Quiescence Period 0.65 Ma	
	UpperMerihuaca	5.49+-0.11
	MiddleMerihuaca	5.56+-0.10
	LowerMerihuaca	5.60+-0.20
	Blanco	/

Table 3.1 - Cerro Galán system stratigraphy and $^{40}Ar/^{39}Ar$ analyses (Folkes et al., 2009, submitted Bull Volc)

The Cerro Galán ignimbrite is the most recent and voluminous ignimbrite (~550 km^3 DRE), erupted at 2.16 Ma (Folkes et al. submitted-b)from the Cerro Galán caldera. The CGI outflow sheet extends to 35 km in all directions from the present caldera, with a maximum runout distance of 74 km to the north of the current topographic margin, where the deposit is 15 m thick (Gonzales, 1984). The CGI covers a preserved areal extent of 2160 km^2.

Although rarely visible, the relationship with the underlying topography is valley-ponding (Fig. 3.2b). Vapor phase alteration and columnar jointing are common, especially where the ignimbrites are confined in paleovalleys (Wright et al. submitted-a, and Fig. 3.2c). No veneer facies have been described associated with the CGI (Cas et al. submitted), and the relationship with paleotopography is commonly *onlap*. The ignimbrite is rhyodacitic in composition, largely characterized by massive facies and up to 200 m thick; it is extremely crystal-rich (35-45 % of matrix volume), pumice-poor (<10 %) and lithic-poor (<5 %) (Fig. 3.2d-e).

Petrographic analyses carried out by Folkes et al. submitted-b) show a mineral assemblage consisting in plagioclase > biotite > quartz > apatite > magnetite > ilmenite > zircon > titanite > monazite, in decreasing order of abundance. Amphibole and sanidine are also present in minor proportion.

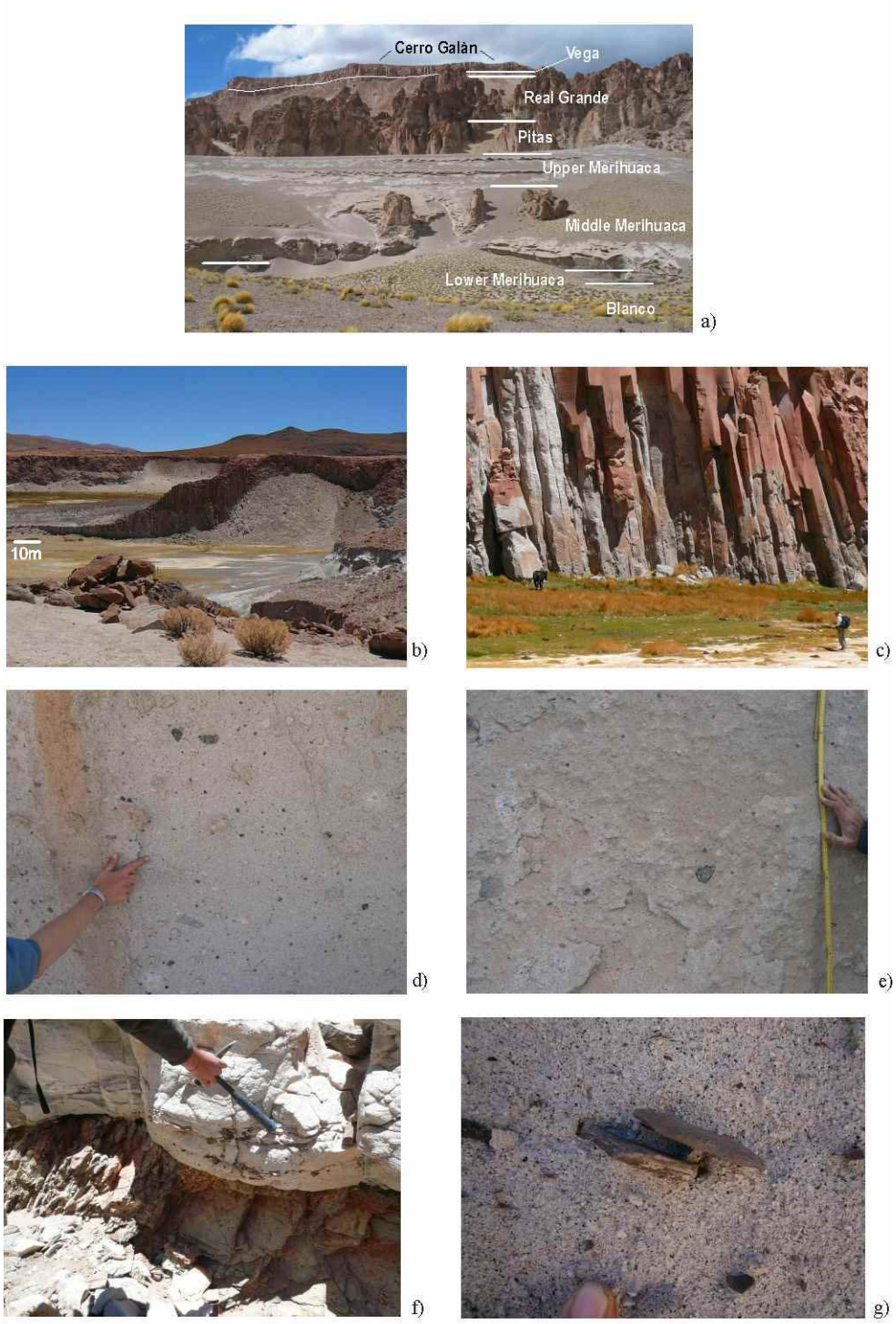

Fig 3.2 - a) Toconquis Group and Cerro Galán ignimbrite at the Rio Las Pitas locality, Vega Real Grande section (yellow star in Fig 1); b) Valley pond facies of CGI. Note the flat topped surface (Curuto locality, 27 km west of the caldera); c) columnar jointing at Curuto; d-e) typical facies of CGI from the base (d) to the top (e) characterized by low pumice (<10 %) and lithic (<5 %) content (Aguas Calientes locality, sites 0031 and 0035; cfr. Tab 3); f) CGI basal contact with the underlying Ordovician metasediments (Curuto locality). Note the relevant presence of rip-up clasts; g) enlargement of previous picture showing imbricated rip-up clasts. Cited localities are in Fig 3.1b

Regarding the magnetic mineralogy assemblage, Fe-Ti oxides represent the majority of opaque minerals, comprising between 0.9 – 1.6 % of the total juvenile clast volumes. This population consists exclusively of magnetite (Usp_{10-19}) and ilmenite (Hem_{21-25}) (Folkes et al. submitted-b).

Petrographic analyses show an up–sequence decrease in crystal content in the most recent ignimbrites (vesicle-free; from 55% to 45%), a decrease in amphibole and possibly biotite. Chemical analyses indicate a remarkable overlap in the composition of all ignimbrites with 69-71% SiO_2, 5-8% K_2O, 1-1.5% MgO (Folkes et al. submitted-b). Geothermometry and geobarometry indicate that magma had pre-eruptive temperatures between 770° and 900°C at pressures of 1.4-2.7 kbar (i.e. max 10 km depth). The CGI magmatic temperatures are constrained at 790°-830°C. Evaluation of viscosity of melt (crystal free) at conditions reasonable for the CGI (density of rhyodacitic magma at 2.46 g/cm^3; 3-4%H_2O; 3 kb; 800°-850°C) give figures of 10^6-10^7 Pa-s (Folkes et al. submitted-b).

4. Temperature estimation by paleomagnetic method

In this section are described the paleomagnetic principles and techniques applied to define the emplacement temperatures of the Cerro Galàn and Toconquis formation ignimbrites. The analyses were carried out on the accidental or accessory lithics embedded in the ignimbrites during the emplacement process.

Laboratory applications were carried out at the Paleomagnetism laboratory at Geological Science Department, Roma 3 University, and at the Swiss Federal Institute of Technology (ETH), in Zurich, in collaboration with Prof. Ann Hirt.

4.1. Methodology

The emplacement temperature of pyroclastic flows can be estimated using paleomagnetic methodologies performed on lithic clasts embedded within pyroclastic deposits (McClelland and Druitt 1989). Lithic fragments can be present in various amounts in pyroclastic density currents, either picked up from magma chamber or conduit walls (accessory lithics), or ripped up along the flow path (accidental lithics). If clasts contain magnetic minerals, generally Fe-Ti oxides, and are heated up, then they can acquire a new magnetization, as a function of the heating temperature. Magnetic minerals are classified into three major groups depending on how they respond to an external magnetic field: diamagnetic, paramagnetic and ferromagnetic. In diamagnetic minerals an applied external field determines magnetic moment in the opposite direction of the external field, which disappears when the field is removed.

The susceptibility, which is the proportional parameter between the applied field and the resulting momentum, is proportional to the applied field and negative. All the materials are diamagnetic, but as the answer is weak, it is masked by paramagnetic or ferromagnetic behavior, when present. Typical diamagnetic minerals are quartz and calcite. Paramagnetic minerals show a magnetic moment parallel to the direction of the applied field that disappears as the field is removed, as in the case of diamagnetic minerals. The susceptibility of paramagnetic minerals is positive and depends on the temperature. The magnetization of a paramagnetic material increase with the applied up to the saturation, but it is contrasted by the internal thermal energy following the Curie law:

K=C\T

where K is the susceptibility, T the absolute temperature and C the Curie constant, which is characteristic for each material.

Ferromagnetic minerals give rise to a magnetic field even in the absence of an applied field, due to the internal. This magnetization is called remanent or spontaneous magnetization and it is caused by strong interactions between neighboring spins at atomic level. The susceptibility of a ferromagnetic substance depends on the temperature as in the paramagnetic case, following the Curie-Weiss law:

$K=C\backslash T-T_c$

where K is the susceptibility, T the absolute temperature, C the Curie constant and Tc the Curie constant, characteristic of each crystal type. Above the T_c, the interactions disappear entirely and the material becomes paramagnetic.

When lithic clasts are incorporated into high temperature pyroclastic flows, i.e. higher than the Curie temperature of the magnetic minerals present in the lithic clasts (e.g. 580°C for magnetite), the original magnetization will be completely removed. A new magnetization, oriented parallel to the Earth's magnetic field at the time of emplacement, will be acquired by the clast when its temperature decreases below the blocking temperature (T_b). The T_b is the temperature below which the relaxation of the magnetization becomes slow compared to the investigated time scale, i.e. the TRM is frozen in at T_b during cooling in the presence of a magnetic field (e.g. Dunlop and Özdemir 1997). Therefore, in clasts embedded in a high temperature pyroclastic density current, a single magnetic component will be detected, which is parallel in all clasts (Fig.4.1a).

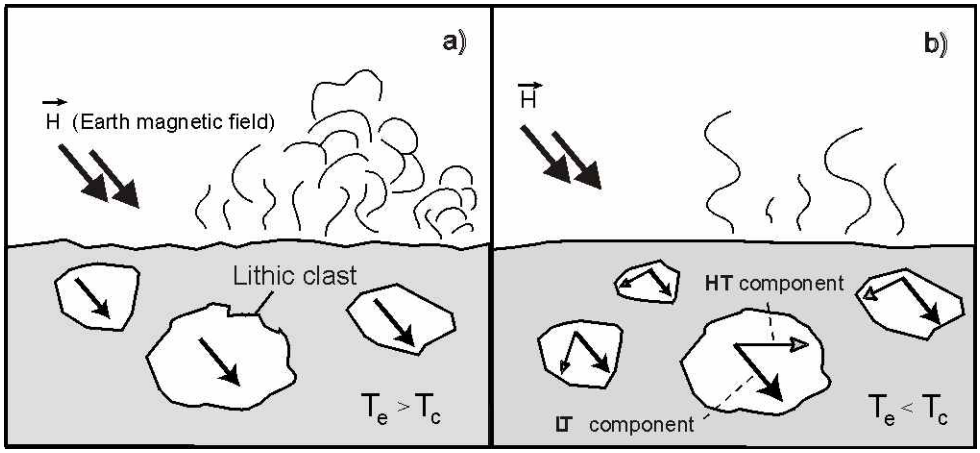

Fig 4.1 - Schematic representation of re-magnetization processes in lithic clasts. a) The ignimbrite emplacement temperature T_e is higher than the Curie temperature ($T_e > T_c$) of the magnetic minerals of the lithic clast. The clast will carry a single component magnetization vector oriented along the Earth magnetic field present during cooling; b) the emplacement temperature is lower than the Curie temperature ($T_e < T_c$). The clast will carry two components: a randomly oriented high temperature (HT) component and a low temperature (LT) component oriented along the Earth magnetic field (modified after Porreca et al 2008)

When lithic clasts are incorporated into a pyroclastic flow at an intermediate temperature, between the ambient and Curie temperature of the magnetic minerals present in the clasts, they will lose a portion of their original magnetization. This occurs at the unblocking temperature (T_{ub}) of the magnetic minerals present in the clast, which, for rapidly cooled flows, is the temperature at which the TRM is lost during laboratory heating. This unblocking temperature is equal to or lower than the maximum temperature of the deposit. During the cooling of the deposit, the clast will acquire a new partial thermoremanence (pTRM), which will partially overprint the original magnetization. In this case, the clast will be characterized by the presence of two components of magnetization: an original, randomly oriented high temperature component and a young low temperature component that is homogenously oriented parallel to the Earth's magnetic field at the time of the deposit emplacement (Fig. 4.1b).

The progressive demagnetization technique emulates the natural processes in the opposite direction, heating the samples from ambient to the Curie temperature (T_c) and measuring the magnetic remanence at each step. The demagnetized clasts can present one or two components of magnetization. In the case of two components of magnetization, the

intersection temperature of the two components is an estimate of the emplacement temperature, whereas in the case of single component oriented parallel to the expected magnetic field, the emplacement temperature will be higher than the unblocking temperature (T_{ub}) for each clast.

To validate the use of paleomagnetic techniques for determination of ignimbrite emplacement temperatures, a statistical analysis of clast orientations must be completed and the potential presence of an overprinting magnetic signature must be evaluated. The process of blocking and unblocking of the magnetization of a lithic clast is a probabilistic process. Grains that are unblocked during the natural heating process may not be similarly unblocked during laboratory heating due the difference in time scale between the natural and laboratory processes. In this case, it is important to demagnetize a large number of clasts to produce reliable, significant statistics.

Furthermore, the paleomagnetic signature can be altered by the effects of chemical overprinting (chemical remanent magnetization, CRM) due to field or laboratory alteration, (McClelland-Brown 1982; McClelland and Druitt 1989) and by the exposure to the Earth's magnetic field at ambient temperature for a long time (viscous remanent magnetization, VRM). Either or both processes can take place in some clasts, producing new magnetic components that may be erroneously interpreted as partial thermal magnetizations (pTRM) and could lead to false temperature estimations. Moreover, both the CRM and the VRM magnetizations vary strongly as a function of various parameters, such as magnetic mineralogy and grain size. Lithic clasts in the Cerro Galan ignimbrite are very heterogeneous in lithology, and the origin of low-T components could vary for each case.

In order to identify the main magnetic carriers and recognize possible chemical magnetic overprint, we have performed a series of rock magnetic measurements on selected samples, which will be described in the next sections.

Finally, in order to distinguish between VRM and pTRM, we follow the approach of Bardot and McClelland (2000) in using the magnetite nomograph by Pullaiah et al. (1975) to determine the relationship between the unblocking temperature (T_{ub}) of a VRM as a function of time. The Pullaiah nomograms refer to SD magnetite, and in the presence of MD magnetite the T_{ub} is underestimated. Anyhow they equally provide a minimum value for the emplacement temperature. The relationship is expressed as:

$$T_{ub} = 75+15 \log (\text{acquisition time in years}) \quad (1)$$

and is valid for magnetite-bearing components with acquisition times between 10^2 and 10^6 years. Being the investigated ignimbrites more than 2 Ma old, they have been subjected to a continuous geomagnetic field for the last 780 Ka (i.e. during Brunhes epoch). In this case, the T_{ub} of VRM is limited to this period and therefore, following the relationship given by Bardot and McClelland (2000), it can not be higher than 165ºC.

Therefore, all the low-temperature components with T_b<165°C may be potentially due to VRM and are therefore not considered here for temperature estimations. Components with T_b>165°C are valid for estimation of partial thermal remagnetization (pTRM).

4.2. Lithics sampling and TRM laboratory procedures

The sampling strategy was planned to evaluate changes in flow emplacement temperature with distance from the vent and with vertical position in the flow deposits. We sampled a total

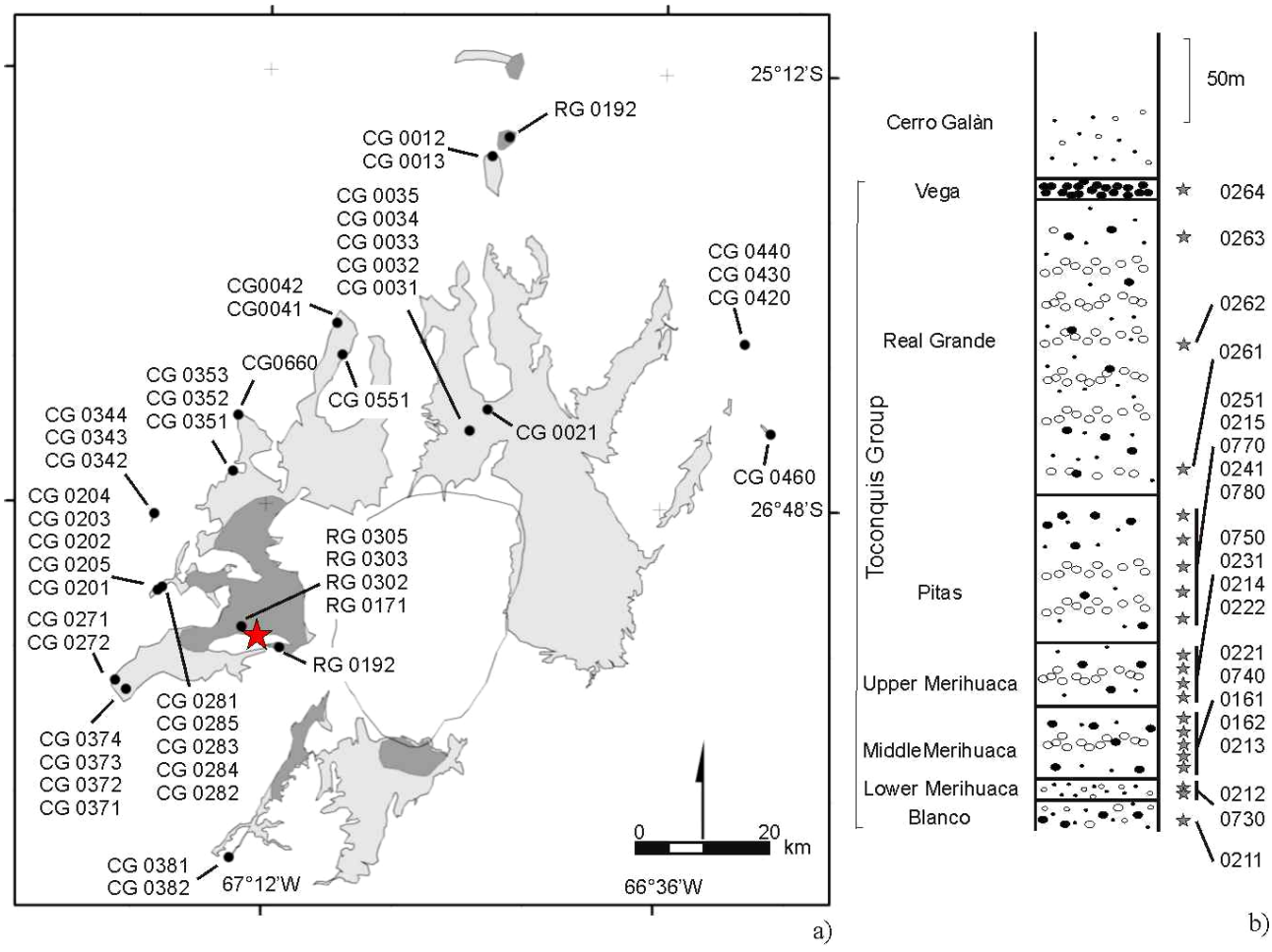

Fig. 4.2 - Sampling site locations. a) The areal extent of the Cerro Galán ignimbrite is shown in light gray; in dark gray is the areal extent of the underlying Real Grande ignimbrite. CG: Cerro Galán ignimbrite; RG: Real Grande ignimbrite;. b) Stratigraphic log of the >250m section at Rio Las Pitas, Vega Real Grande section (red star symbol); sampling sites along the log are represented by gray stars

of 301 oriented clasts from 18 localities (Tables 4.1-4.2); 125 samples were from the Toconquis Group and 176 from the Cerro Galán ignimbrite. The samples were collected from proximal to distal localities (up to 52 km), and, in the case of the CGI, at variable azimuth from the vent (Fig. 4.2). The Toconquis Group ignimbrites were largely sampled at Rio de las Pitas, Vega Real Grande (star in Fig. 4.2a), located 12 km west of the caldera in a >250 m thick section of ignimbrites.

In particular, the Real Grande ignimbrite was sampled at Vega Real Grande and in other three localities, i.e. 500 m NW and SE Vega Real Grande, along Rio de las Pitas, and on the eastern slopes of Cerro Ratones, 55 km N of the caldera (Fig 4.2a). For clarification, we use the word *locality* to identify a single point on a 1:25.000 map while a *site* is an outcrop of about 1 m^2, where lithic clasts were sampled.

Samples were collected at different heights in the CGI in order to identify temperature stratifications. At Aguas Calientes, a proximal locality N of the caldera, five sites (0031-0035) were sampled vertically from a 58 m thick section; in Antofagasta 4 sites were sampled from a 15 m thick section (0371-0374) and at Puntas Gordas and Los Nacimientos, 3 sites were sampled from 35 and 20 m thick sections, respectively (0342-0344 and 0351-0353 respectively). Site locations are in Fig. 4a and sections height and distances from caldera rim are reported in Tab. 4.2, for each site. At Paycuqui, five sites were sampled at each of two sections (0201-0205 and 0281-0285). Finally, three sites were sampled in the CGI subunits at the distal locality of Tacuil (sites 0420, 0430 and 0440). The clast population is variable in lithology, including dominant plagioclase-phyric dacite clasts, found in almost all outcrops, and subordinate metavolcanics, metasediments, quartzites and amphibolites. In most cases, the lithic clast lithologies reflect the lithologies of the substrate upon which the ignimbrite was emplaced. The substrate is dominated by slightly deformed Ordovician rocks (metavolcanics, mica-schists, and low grade metasediments) in the western sector and by lower Paleozoic crystalline units in the eastern sector (granitoids and orthogneisses; Kay et al. 2008). Plagioclase-phyric dacites (ppd) are not encountered in outcrop outside the caldera, and its ubiquitous presence can be related to a proximal emplacement of dacitic lavas around the caldera or to an intracaldera dome.

We therefore conclude that, excluding ppd clasts, lithic clasts are mostly accidental, ripped up from the ground surface during transport of the flow, and the proportion of clasts that are inferred to originate from the chamber walls or the conduit margins is small. This association is particularly useful for TRM studies of the emplacement temperatures of ignimbrites, because the acquired TRM of accidental clasts is related to the pyroclastic flow temperature

and not to lengthy pre-heating in the conduit. Lava clasts and metavolcanics were preferentially sampled over other lithic types because they are more common and provide more reliable paleomagnetic results than other lithologies; they represent 60% and 20% of the total sampled lithologies, respectively. Average clast sizes in the deposit range from 0.5 to 10-15 cm.

At each site we sampled from 3 to 10 clasts (Tables 4.1, 4.2), except in case of very low lithic percentages (<1% of deposit) where less than 3 clasts were sampled. The strike and dip of each clast were measured in the field with a magnetic compass. The magnetic deviation induced by the deposit on the compass was tested and was determined not to influence the paleomagnetic study, i.e. the identification of the number of components of magnetization and their orientations with respect to the geocentric axial dipole (GAD) geomagnetic field. Most of the clasts were not larger than 4 cm, with an average diameter of ~1.5 cm. For some larger clasts (5 to 20 cm in diameter), subsamples were cut from the core and rim to evaluate the presence of a temperature gradient within biggest clasts. The oriented clasts (or subsamples of clasts) were embedded in white non-magnetic plasticine, which was placed into a rigid plastic cylinder with standard dimensions (diameter ϕ=25 mm, height h=22.5 mm) in the laboratory, following the procedure adopted by Cioni et al. (2004). Paleomagnetic analyses and rock magnetic analyses were performed at the Paleomagnetic Laboratory of University of Roma Tre; rock magnetic analyses of some representative samples were also carried at the Paleomagnetic Laboratory of ETH-Zurich.

In order to identify the mineralogy of the main magnetic carriers and to assess whether any mineralogical alteration has affected our temperature estimates, we have performed rock magnetic analyses on 15 representative samples (except thermomagnetic analyses, which were performed on 14 samples). The analyzed samples were obtained by eight dacites, four metavolcanics, two metasediments and a quartzite clast. Rock magnetic measurements include (*a*) determination of isothermal remanent magnetization (IRM), that allows the definition of the saturation field and the coercivity of remanence (H_{cr}); (*b*) thermal unblocking of a composite three-component isothermal remanent magnetization (composite IRM), that allows to identify the contribution of the soft, medium and hard coercivity mineral fractions, and the relative mineralogical phases; and (*c*) thermomagnetic analysis of high-temperature magnetic susceptibility measured in air, in order to identify the Curie Temperature of the main magnetic carriers and to detect any mineralogical alteration during heating. The rock analyses are performed on powdered samples, and only six out of fifteen lithic clasts were large enough to allow the cutting of samples both for rock analysis and TRM analysis.

The conditions for determination of isothermal remanent magnetization (IRM) include a progressive increase in the imposed magnetizing field, using an ASC-Impulse Magnetizer, and the measurements of the remanent magnetization at each incremental step by a JR-6A spinner Magnetometer. Samples were firstly saturated in a 2000 mT magnetic field along the -z sample direction and then an IRM was acquired stepwise, in nine steps from 50 mT to 2000 mT, in an antipodal field (+z). This procedure provides information on the field needed to saturate the magnetization as well as the coercivity of remanence ($H_{cr'}$). The three-component IRM was then thermally demagnetized in thirteen steps on the same samples, according to the procedure reported by Lowrie (1990). Maximum, intermediate, and minimum magnetic fields of 120 mT, 600 mT, and, 1700 mT respectively, were applied to the x, y, and z axes of the samples.

In order to define the Curie temperature of the magnetic minerals and to exclude the presence of thermal mineralogical alteration, magnetic susceptibility was measured as a function of temperature in air, from room temperature to 700°C, in a heating-cooling cycle on ~2cm^3 of powdered sample. This kind of measurement was made using AGICO CS-2 furnace apparatus.

Finally, the textural relationships between magnetic and not-magnetic mineral phases were determined using thin sections of eight representative lithic samples, selecting the most common lithologies (dacite, metavolcanics, metasediments, and quartzites).

The natural remanent magnetization (NRM) was measured using a JR-6A Spinner Magnetometer on 301 specimens. Six of these specimens were also analyzed for magnetic rock determination and in other five clasts two specimens were obtained from each one, at the rim and core of the clast. Thermal demagnetization was carried out using an external field shielded furnace with residual fields <10nT in 13 to 17 thermal steps, reducing the temperature steps from 50° to 20°C at higher temperature. Magnetic susceptibility was also measured at each thermal step by the KLY-3 Kappabridge instrument to detect any possible mineralogical changes during the heating process.

Magnetic remanence data were plotted on a Zijderveld orthogonal demagnetization diagram (Zijderveld 1967) and the Remasoft 3.0 software was used to identify the principal magnetic components (Chadima and Hrouda 2006). The number of remanence components was defined by evaluating maximum angular deviation (MAD) values of the each single vector. A maximum of 10° was accepted as a limit of reproducible result for a single component. Paleomagnetic mean directions for each site and ignimbrite unit are made applying Fisher statistics (Fisher 1953). The best estimates of the dispersion, k, and the

direction reliability evaluated at the 95% confidence level, α_{95}, have been also calculated for each ignimbrite unit.

4.3. Lithics magnetic mineralogy - results

The acquired IRM curves for our samples show a rapid increase in IRM over the low magnetic field range (Fig. 4.3). Furthermore, the magnetic saturation (where the normalized IRM value equals 1.0) of most samples is reached at fields lower than 600-800 mT (Fig. 4.3). This behaviour is characteristic of low-coercivity magnetic grains, such as titanomagnetite and/or magnetite (e.g. Dunlop and Özdemir 1997). In addition, the remanent coercivity (H_{cr}) values of these samples ranges from 35 to 75 mT (Fig. 4.3), which typically represent values of low-coercivity minerals (Dunlop and Özdemir 1997). In contrast, four samples do not reach magnetic saturation at the maximum applied field (2000 mT), suggesting that these samples also contain high-coercivity minerals, such as hematite. The remanent coercivity of these four samples is respectively 40, 75, 65 and 52 mT.

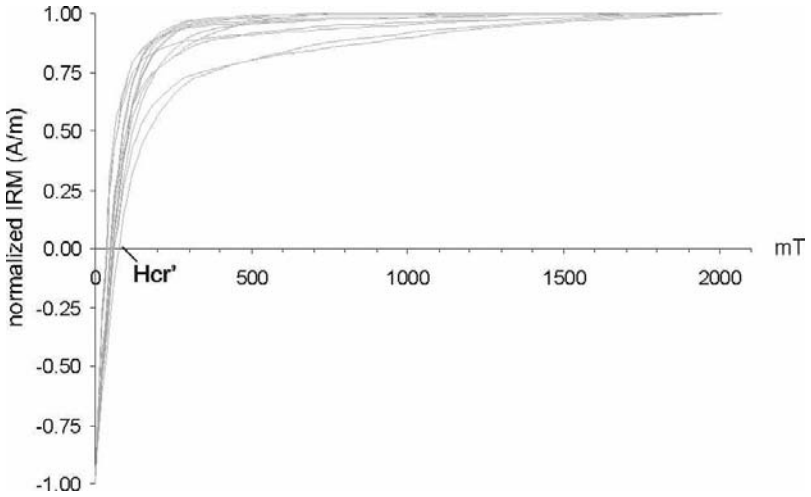

Fig. 4.3 - Isothermal remanent magnetization (IRM) analyzed in fifteen representative samples. 95% saturation is reached at 350-400mT in most of the analyzed samples except in four samples that do not reach

Using thermal decay of composite IRM and thermal demagnetization we confirm the predominance of low-coercivity minerals. The IRM values of the x, y, and z components (soft, medium, and hard fractions) indicate the relative proportion of each component. Figure 4.4 shows that the soft fraction (coercivity <0.2T) predominates in all samples. Using thermal demagnetization, we find that this low-coercivity component is stable up to 580°C, indicating that magnetite is the main magnetic carrier (e.g. Dunlop and Özdemir 1997; Fig. 4.4a). Some samples are characterized by drops at both 580°C and between 350°C and 400°C (fig. 4.4b), suggesting the presence of magnetite/Ti-poor titanomagnetite and probably maghemite, respectively. Metasediment samples are characterized by a soft fraction decay at ~300°C, which could be related to the presence of iron sulphides (e.g. Weaver et al., 2002; fig. 4.4d and the relative thermomagnetic curve in Fig. 4.5f). Iron sulphides can be present as

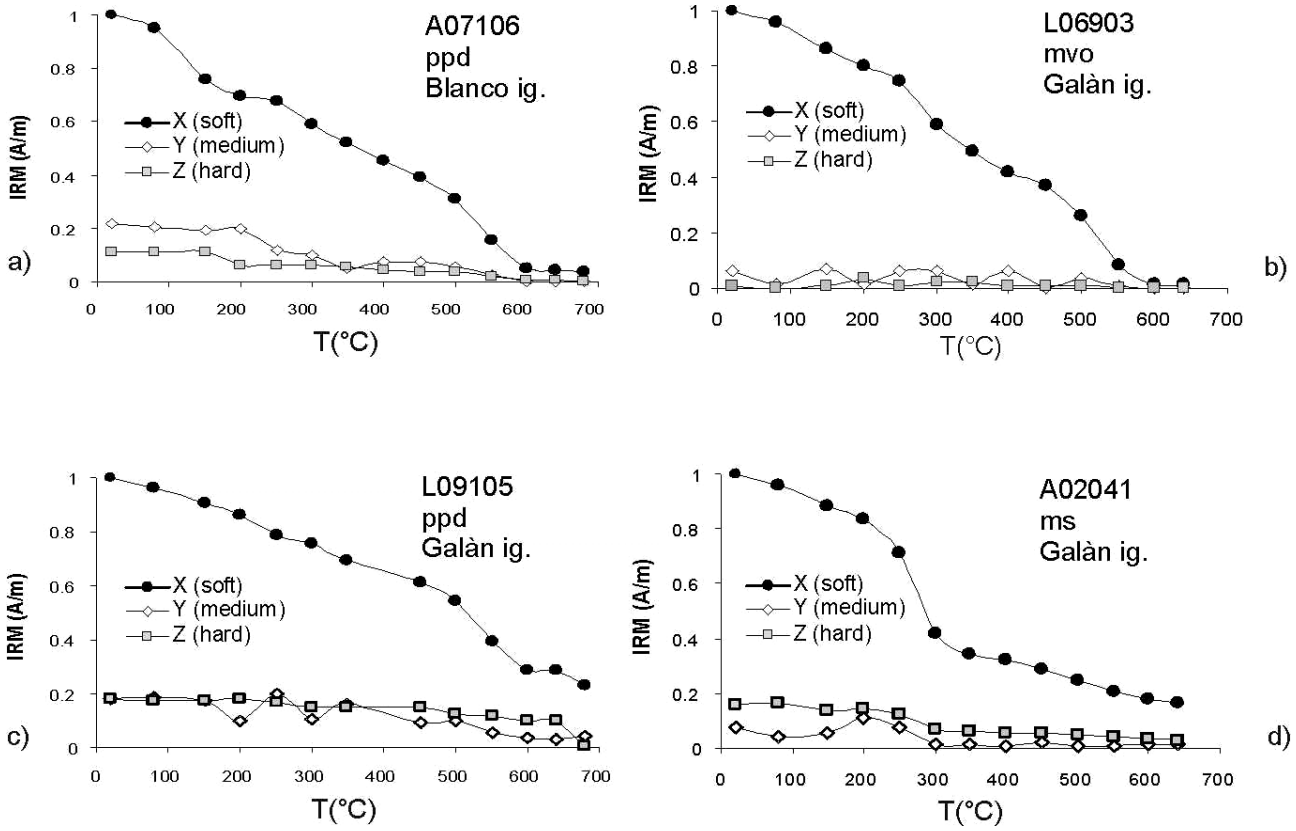

Fig 4.4 - Representative composite IRM decay for four samples. The soft fraction prevails in all the fifteen analyzed samples. a) Soft fraction decay at 580°C is indicative of the presence of magnetite; b) smooth step at 300-400°C in the soft fraction can be indicative of maghemite and titanomagnetite c) the hard fraction is at about 20% of the soft fraction and decays at about 680°C revealing low content of hematite; d) the soft fraction decay by 40% at about 300°C can reveal the presence of iron sulphides as secondary magnetic mineral in metasediments. ppd: plagioclase phyric dacite; mvo: meta-volcanic Ordovician; ms: mica-schist

secondary minerals in metasediments as the shown sample (e.g. Weaver et al. 2002; Fig. 4.4d). The proportionally minor medium and hard fractions (up to 20% of soft fraction) generally remain stable up to 680°C (Fig. 4.4c), suggesting the presence of hematite in some samples.

The thermomagnetic curves made on 14 clasts confirm the presence of different minerals as a function of clast lithology (fig. 4.5a-f). One sample did not give reliable results. In the rest of the analyzed samples, the heating and the cooling curves are reversible, except in three samples. In these three samples, from different lithologies, the susceptibility of the cooling curve is remarkably higher than the heating curve, indicating that some oxidation has occurred during the heating process (e.g. fig. 4.5f). In twelve samples, the susceptibility drops to zero between 580-600°C, which is the Curie temperature of magnetite (fig. 4.5a-c). Five samples also show a susceptibility deflection at 300-400°C, indicating the presence of another, low T_b magnetic carrier, likely maghemite (fig. 4.5d). In two dacite samples, the

susceptibility drop occurs between 600°C and 620°C, confirming the presence of hematite as a magnetic carrier (fig. 4.5e).

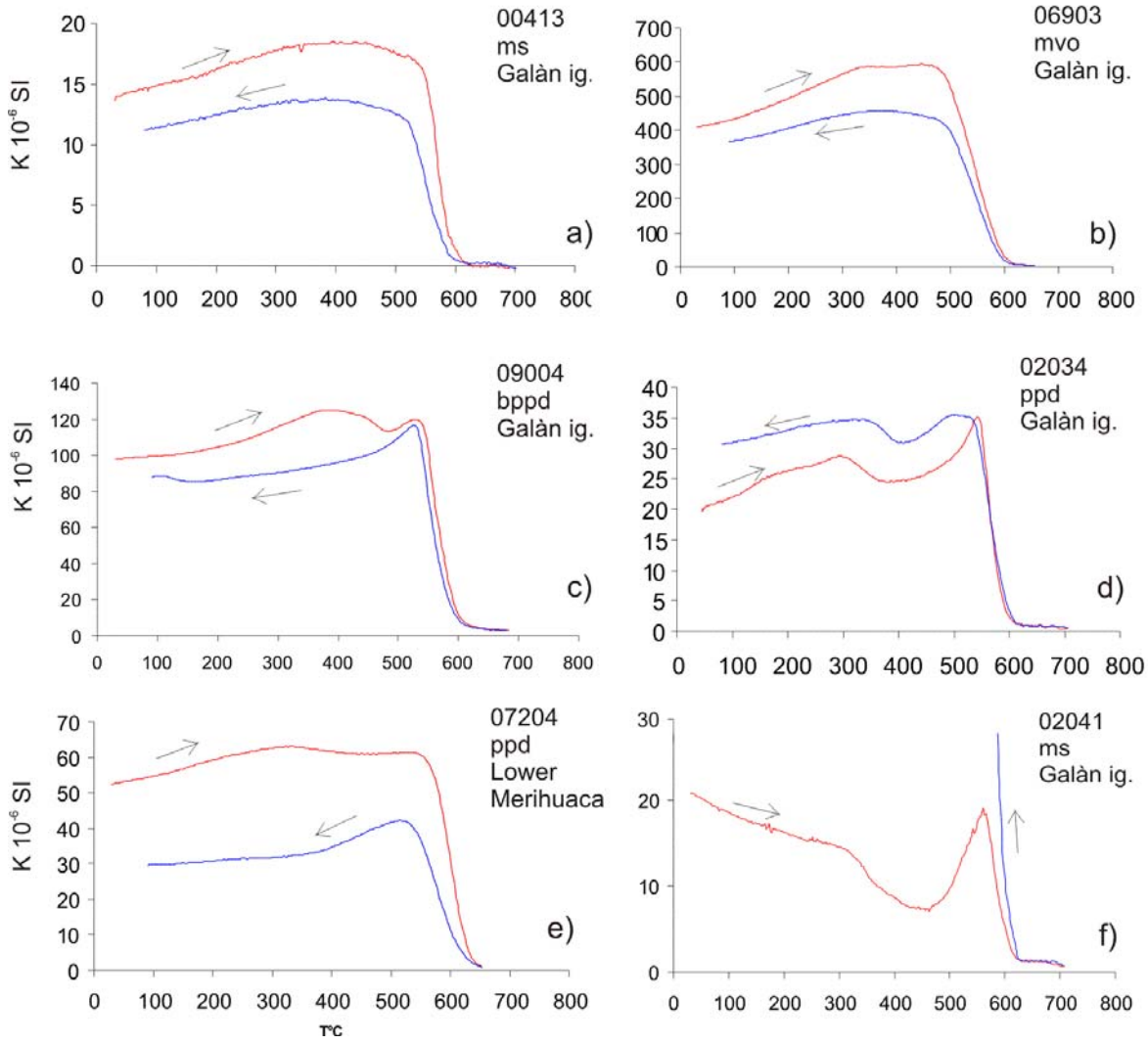

Fig. 4.5 - Representative thermomagnetic curves. Most of the fourteen analyzed samples show good correlation between heating and cooling curves, indicating that there is no mineral formation during the heating process; steep decays represent Curie temperatures of magnetic minerals; a-b) Curie temperatures at 580°C indicate the presence of magnetite; c-d) deflection at 300-400°C can indicate the presence of maghemite; this behavior occurred in three dacites and two metavolcanics; e) Curie temperature at 620°C indicate the presence of hematite; f) peak at 580°C in the heating curve and abrupt increase in the cooling curve suggest new mineralogical phase growing during heating; this behaviour is shown by two samples. ppd: plagioclase-phyric dacite; bppd: black plagioclase-phyric dacite; mvo: meta-volcanic Ordovician; ms: mica-schist

4.4. Thermal Remanent Magnetization (TRM) data

The natural remanent magnetization (NRM) of all the analyzed samples, normalized to the standard 10 cm^3 volume specimen, is highly variable, ranging from $2.4x10^{-3}$ to 79 A/m, where dacite samples show slightly higher values than other lithic types.

The remanent magnetization is usually removed at temperature >580°C and the paleomagnetic behaviour is stable in most cases. Four samples from the Toconquis Group and twenty samples from Cerro Galán Ignimbrite (Appendix I and II) show an instable behaviour and therefore have not been considered in the statistics.

To discriminate between the magnetic signatures of different clasts, we classified the specimens by the number of magnetic components and their orientation, following the demagnetization pattern classification reported in McClelland et al. (2004) but using different class names. Class A specimens show a single magnetization component vector. Class B specimens show two components, one stable at high temperatures (HT component) and one at low temperatures (LT component). The LT component is consistent with the geocentric axial dipole (GAD) geomagnetic field, whereas the HT component is randomly oriented. The GAD at Cerro Galán today has an inclination of -22°; the 2.56 Ma Cerro Galán Ignimbrite (Folkes et al. this issue-a) is expected to have had a reversed polarity, producing positive inclination. For the Toconquis Group the expected magnetic polarity is variable for each unit; taking into account biotite $^{40}Ar/^{39}Ar$ ages of Folkes et al. (this issue-a), Blanco, Lower, Middle and Upper Merihuaca, and Vega Ignimbrites should have reverse polarity, whereas the Pitas and Real Grande Ignimbrites should have normal polarity (based on polarity subchrons of Gradstein et al. 2004).

4.4.1. TRM results for the Toconquis Group ignimbrites

The Toconquis Group includes seven ignimbrite units; each of them was analyzed by thermal demagnetization of lithic clasts. The NRM intensity varies from $2.4x10^{-3}$ to 0.2 A/m, with very few samples showing values up to 3 A/m. Individual sample results are shown in Appendix I, while composite results for each Toconquis unit are described below (Fig. 4.6; Tab. 4.3).

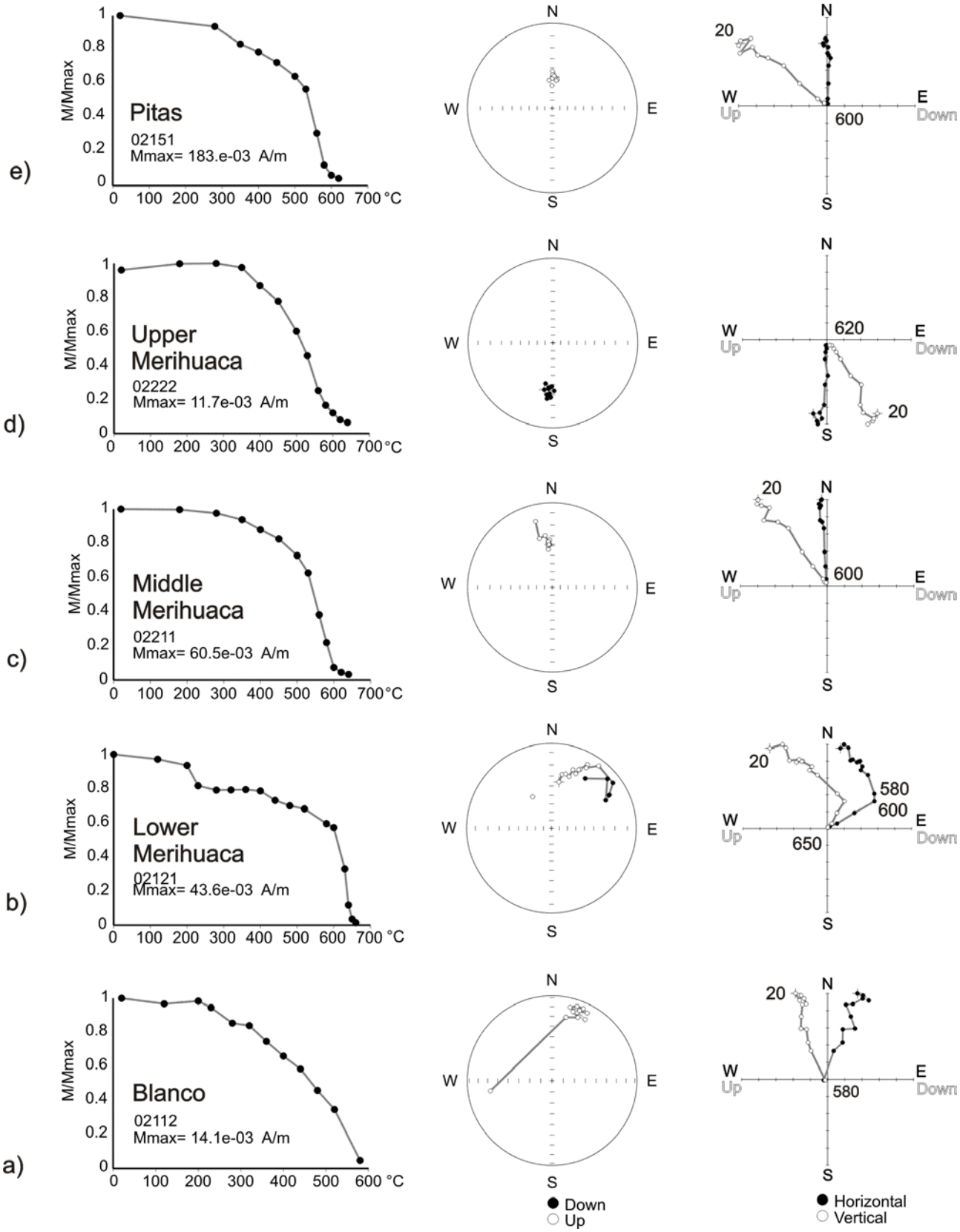

Fig. 4.6 - Thermal demagnetization data for some representative samples of Toconquis Group units (a-g). For each sample, intensity decay, equal area stereonet and Zijderveld diagrams are shown. (left) normalized intensity decay curve; (middle) equal area projection (solid dots: lower hemisphere; open dots: upper hemisphere); (right) orthogonal plots (Declination: black dots on the horizontal plane; apparent Inclination: white dots on the vertical plane). Sample references in Appendix I

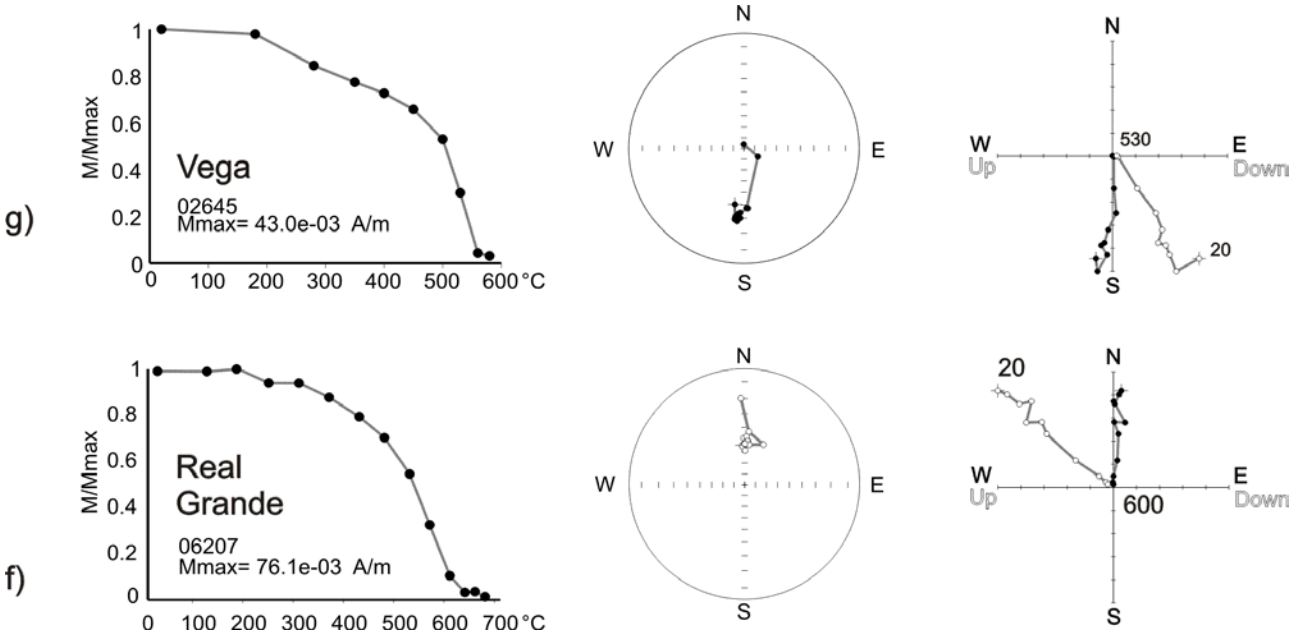

Fig. 4.6 - continued

In the Blanco ignimbrite all seven demagnetized samples show a single magnetic component vector stable up to 580°C (Fig. 4.6a). Sub-samples from the core and rim of a 10 cm clast were also analyzed and both of the sub-samples show a single normally directed component, completely demagnetized (T_{ub}) at 520°C. This component is upward oriented in all clasts and its direction is almost close to the present geomagnetic field, thereby all clasts in the Blanco ignimbrite are classified Class A. The mean paleomagnetic direction for this unit is D=26.3°; I=-22°; (Fig. 4.7a). The high angle of α_{95} is due to poor number of analyzed clasts.

In the Lower Merihuaca ignimbrite, sixteen clasts were demagnetized. Half of these clasts show a single magnetic component, while the other half shows two magnetic components. The single component samples are completely demagnetized at temperatures between 530°C and 630°C and their direction is close to the current magnetic field (class A), with normal polarity. The mean paleomagnetic direction is D=6.3°, I=-45.4° (Fig. 4.7b). In the samples with two components of magnetization (Fig. 4.6b), the LT component is upward oriented with D=8.4° and I=-45.6° (Fig. 4.7c), whereas the HT component is randomly oriented (Fig. 4.7d). These samples are grouped as class B and the temperatures of separation between LT and HT components vary within a small range from 580° to 610°C. The emplacement temperature of the Lower Merihuaca unit can therefore be constrained in a range of 30°, while for all the other units the estimates are for a *minimum* emplacement temperature.

The twenty-six lithics sampled in the Middle Merihuaca ignimbrite show low NRM, less than 0.1 A/m. One sample did not give reliable results and therefore it was not used for

statistics. Twenty-four samples show a single component demagnetization vector (class A, Fig. 4.6c), while one sample shows two components (class B). Most of class A clasts are completely demagnetized at 580°C and their mean paleomagnetic direction is D=8 ° I=-44.9° (Fig. 4.7e).

In the Upper Merihuaca ignimbrite, twenty samples were thermally demagnetized, with four samples failing to yield stable demagnetization trajectories. Fifteen samples show a single component of magnetization oriented downward (i.e. reverse polarity), demagnetized between 580° and 620°C. The clasts are therefore classified as class A (Fig. 4.6d), and the orientation of the mean direction of this component is D=193.3°, I=49.9° (Fig. 4.7f). One sample shows two component demagnetization vectors. In this sample the temperature of separation between LT and HT components is in the range of 530-560°C and totally demagnetized at 590°C.

The Pitas ignimbrite was studied by the thermal demagnetization of twenty-five lithics. With one exception, all clasts were demagnetized at temperatures between 580°C and 640°C and show a single vector component (class A, Fig. 4.6e) directed D=15°, I=-42° (Fig. 4.7g).

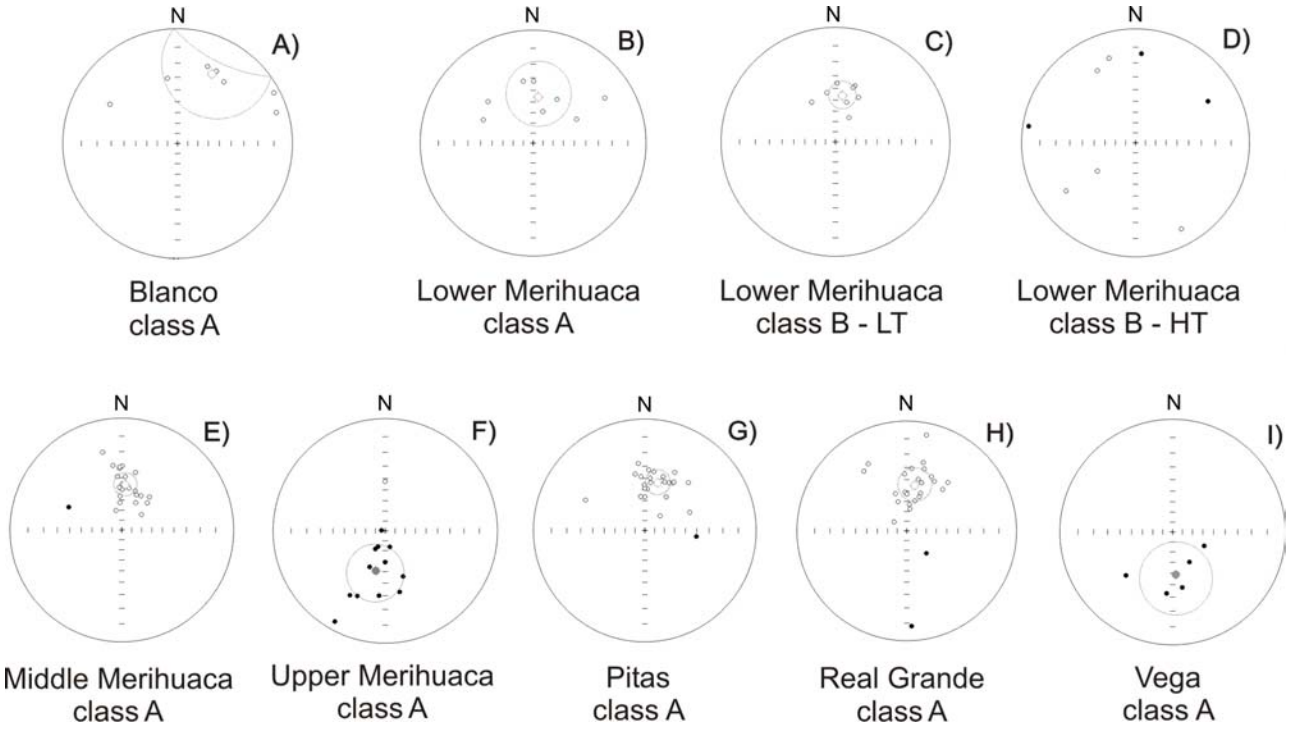

Fig. 4.7 - Equal area stereonets of mean remanence directions of the Toconquis Group units (a-I). Open symbols are vectors projected into the upper hemisphere; filled symbols represent vectors projected onto the lower hemisphere. Small and large gray circles gray symbols are mean paleomagnetic directions and α_{95} ellipses

The remaining sample is stable up to 650°C and shows two components of magnetization. The LT component, stable up to 610°C is directed D=30° I=-38°.

In the Real Grande ignimbrite, twenty-six samples were demagnetized. All the lithics show a single component demagnetization vector (class A, Fig. 4.6f), stable between 520°C and 630°C and oriented at D=9.7°, I=-44° (Fig. 4.7h).

Finally, the five lithic clasts sampled in the Vega ignimbrite show a single component demagnetization vector (class A, Fig. 4.6g) directed downward at D=175.8°, I= 48.6°(Fig. 4.7i) and stable up to 560°C.

unit	N	Nr	class	Dec. °	Inc. °	α_{95} °	R	k
Cerro Galan	176	150	A	182.9	49.9	5	128	7
Vega	5	5	A	175.8	48.6	31	4	7
Real Grande	26	26	A	9.7	-44.4	15	21	5
Pitas	25	24	A	15.0	-42.2	11	22	8
Upper Merihuaca	20	16	A	196.2	44.8	21	12	4
Middle Merihuaca	26	25	A	8.1	-45.1	10	22	10
Lower Merihuaca	16	8	A	6.3	-45.4	28	7	5
			B-Low Tb	8.4	-45.6	12	8	23
			B-High Tb	311.5	-26.1	98	3	1
Blanco	7	7	A	26.3	-22	35	5	4

Table 4.3 - Group statistics for Cerro Galán and Toconquis Group ignimbrites. Number of samples (N); number of reliable samples (Nr); classification (class); paleomagnetic mean direction (Dec; Inc), semi-angle of 95% confidence (a95), resultant length vector (R), and dispersion (k) are reported for each unit.

4.4.2. TRM results for the Cerro Galán ignimbrite

The NRM of the 176 analyzed lithic clasts from the Cerro Galán Ignimbrite range between $4x10^{-3}$ and 79 A/m. The principal component analysis applied to the thermal demagnetization results identified magnetization components with MAD usually less than 5°.

Most of the analyzed specimens, 150 out of 176 demagnetized clasts, show a single component demagnetization vector (class A; Fig. 4.8a-c). The mean direction of this component, shown in Figure 4.9, is well defined and oriented D=182.3° I=48.7°. The minimum and maximum demagnetization temperatures are 440° and 680°C respectively, but most of the samples (97%) are completely demagnetized between 520° and 620°C. Twenty-six specimens were not considered in the mean direction evaluation, as they showed anomalous demagnetization paths or did not demagnetize.

Four lithic clasts from the Cerro Galán ignimbrite were analyzed by TRM analysis at the rim and at the core (Fig. 4.10). In two clasts the core results are not reliable, while the external part show single component demagnetization vector, completely demagnetized at 600°C and

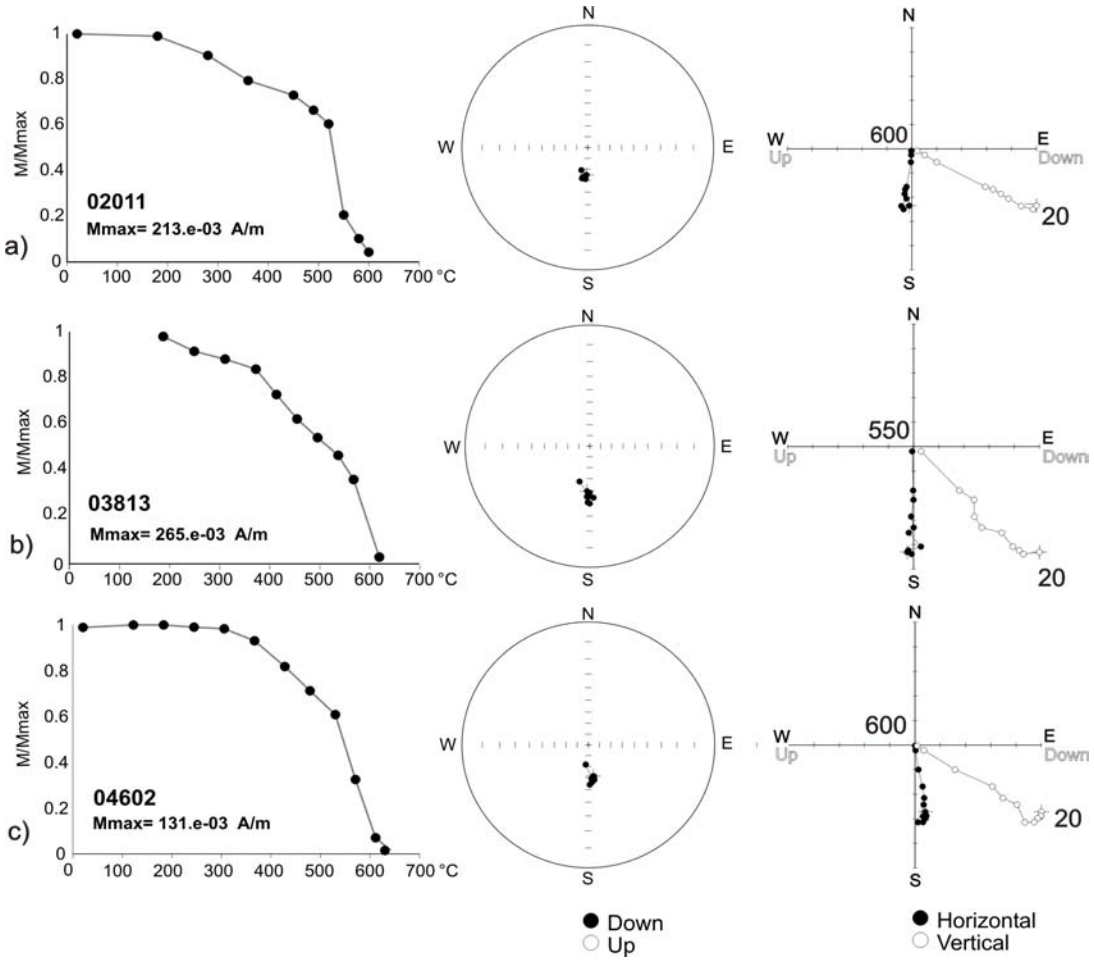

Fig. 4.8 - Representative intensity decay, equal area stereonet, and Z-plots of Cerro Galán ignimbrite TRM analysis. a-c) single component (class A) demagnetization vectors. Symbols as in

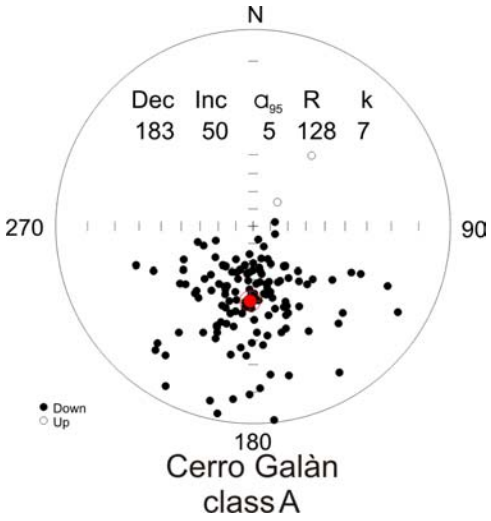

Fig. 4.9 - Equal area stereonets of the remanence directions of the Cerro Galán ignimbrite. Symbols as in Fig 9

550°C respectively. The other three samples show exactly the same behaviour at the core and rim, completely demagnetized between 580°C and 600°C with a single component demagnetization vector.

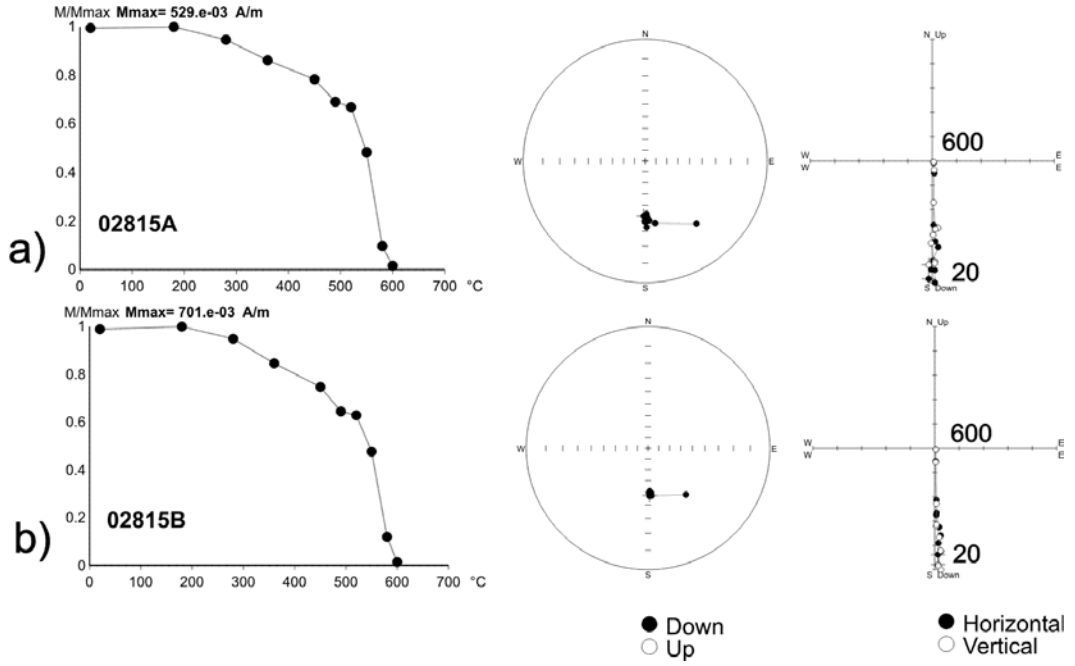

Fig. 4.10 - TRM analyses from the core (a) and the rim (b) of a single lithic clast. The similarity of the single component vector directions and the demagnetization curve show that the thermal behaviour is homogeneous throughout the clast.

4.5. Ages and polarity

The paleomagnetic directions obtained by the TRM analysis for the Cerro Galàn ignimbrite and the Toconquis group, were compared with the Ar/Ar ages determined on the biotite (Folkes et al, submitted) and the results are compared in the paleomagnetic scale of Gradstein et al. 2004) (Fig. 4.11). The Ar/Ar ages of the Merihuaca Fm correspond to the reverse C3r chron, which is concordant with the paleomagnetic results for the Upper Merihuaca ignimbrite, but discordant for the Lower and Middle Merihuaca. The Pitas ignimbrite show an

Ar/Ar age that is concordant with the paleomagnetic results, corresponding to the normal subchron C3n3n. The Real Grande and Vega ignimbrites correspond within error to the paleomagnetic results, assigning the ignimbrites to the subchrons C3n2n (normal) and C3n1r (reverse), respectively. The Ar/Ar ages for the Cerro Galàn Ignimbrite coincide with the reverseC2r chron.

The dense sampling along the Vega Real Grande section supported the recognition of two units not documented by the previous field works (Francis et al. 1983; Sparks et al. 1985), the Pitas ignimbrite and Vega ignimbrite (Folkes et al. submitted)

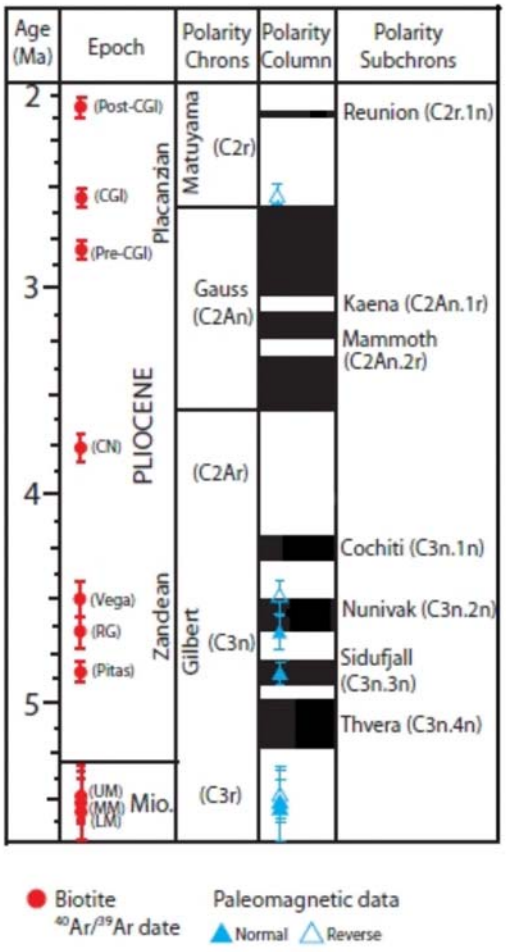

unit	Ar/Ar ages (Ma)	polarity
Galan	2.16 ± 0.16	reverse
Cueva Negra	3.37 ± 0.116	/
Vega	4.07 ± 0.11	reverse
Real Grande	4.24 ± 0.06	normal
Pitas	4.54 ± 0.06	normal
Upper Merihuaca	4.96 ± 0.02	reverse
Middle Merihuaca	5.12 ± 0.11	normal
Lower Merihuaca	5.14 ± 0.09	normal
Blanco		normal

(Folkes et al, submitted Bull Volc.)

Fig. 4.11 - paleomagnetic results. In red the biotite ages with error bars; in blue the TRM results for the Toconquis formation and Cerro Galàn ignimbrite. Paleomagnetic scale by Gradstein et al., 2004.

4.6. Estimation of the emplacement temperature

As described above all the ignimbrites of the Toconquis Group and the Galán ignimbrite, except the Lower Merihuaca unit, show a predominance of class A clasts, with unblocking temperatures ranging mostly between 520° and 620°C. Lower Merihuaca class B clasts allowed constraining the emplacement temperature of this unit between 580° and 610°C.

The temperature estimation at each single site is evaluated on the basis of clast classification. Clasts with viscous remanent magnetization (VRM) are either classified as class A or B on the basis of the behaviour at higher demagnetization step, and therefore we refer to the behaviour of the other components to set the emplacement temperature.

In class A clasts (with a single component of magnetization), the magnetization is stable up to the maximum blocking temperature of its magnetic minerals and its orientation does not change during heating process. This suggests that the clasts were heated to temperatures equal or higher than their maximum blocking temperatures. Emplacement temperatures that exceed the Curie temperatures of magnetic minerals present in the clasts cannot be defined by paleomagnetic techniques. For this reason, we estimate a minimum emplacement temperature on the basis of the laboratory unblocking temperature T_{ub}, which mirrors the Curie temperature distribution of class A clasts.

The fact that also the clasts locally ripped up from the substrate are in class A allows us to confirm that they were heated at temperatures higher than Curie temperatures during transport and after emplacement of ignimbrite, something which instead could be questioned for accessory lithics, since they may have been pre-heated within the conduit and may not reflect emplacement temperatures.

For those sites dominantly containing B clasts, the estimation of the emplacement temperature is constrained between the maximum temperature of the LT component and the minimum temperature of the HT component (McClelland and Druitt 1989). In the Lower Merihuaca ignimbrite, the separation of LT and HT components occurs in a very narrow interval, leading us to estimate an emplacement temperature between 580° and 610°C. In the same site, clasts with higher temperatures belonging to class A were probably heated at vent before being incorporated in the pyroclastic flow, preserving very high temperature at emplacement.

The frequency distribution of the T_{ub} for all clasts from Cerro Galán ignimbrite is reported in Fig. 4.12a. The majority of the T_{ub} values (60%) are in the range between 540° and 580°C, indicating that the main magnetic carrier is magnetite (T_c=580°C) or Ti-magnetite, as the unblocking temperature is not only characteristic of the mineralogy, but also of magnetic

grain size (not investigated in this study) as shown by magnetic mineralogy analysis. The remaining 40% is equally distributed in the range of 500-540° and 600-620°C, indicating that the magnetic carriers in these clasts are titano-magnetite and hematite, respectively. We can therefore conclude that Cerro Galán ignimbrite was emplaced at temperature higher than the maximum unblocking temperature T_{ub} of the samples, which is 620°C.

There is no variation of the T_{ub} with distance from the caldera (R^2 =0.3; Fig. 4.12b). Furthermore, T_{ub} does not vary with lithology, as shown in Fig. 4.12c. Modal T_{ub} values lie

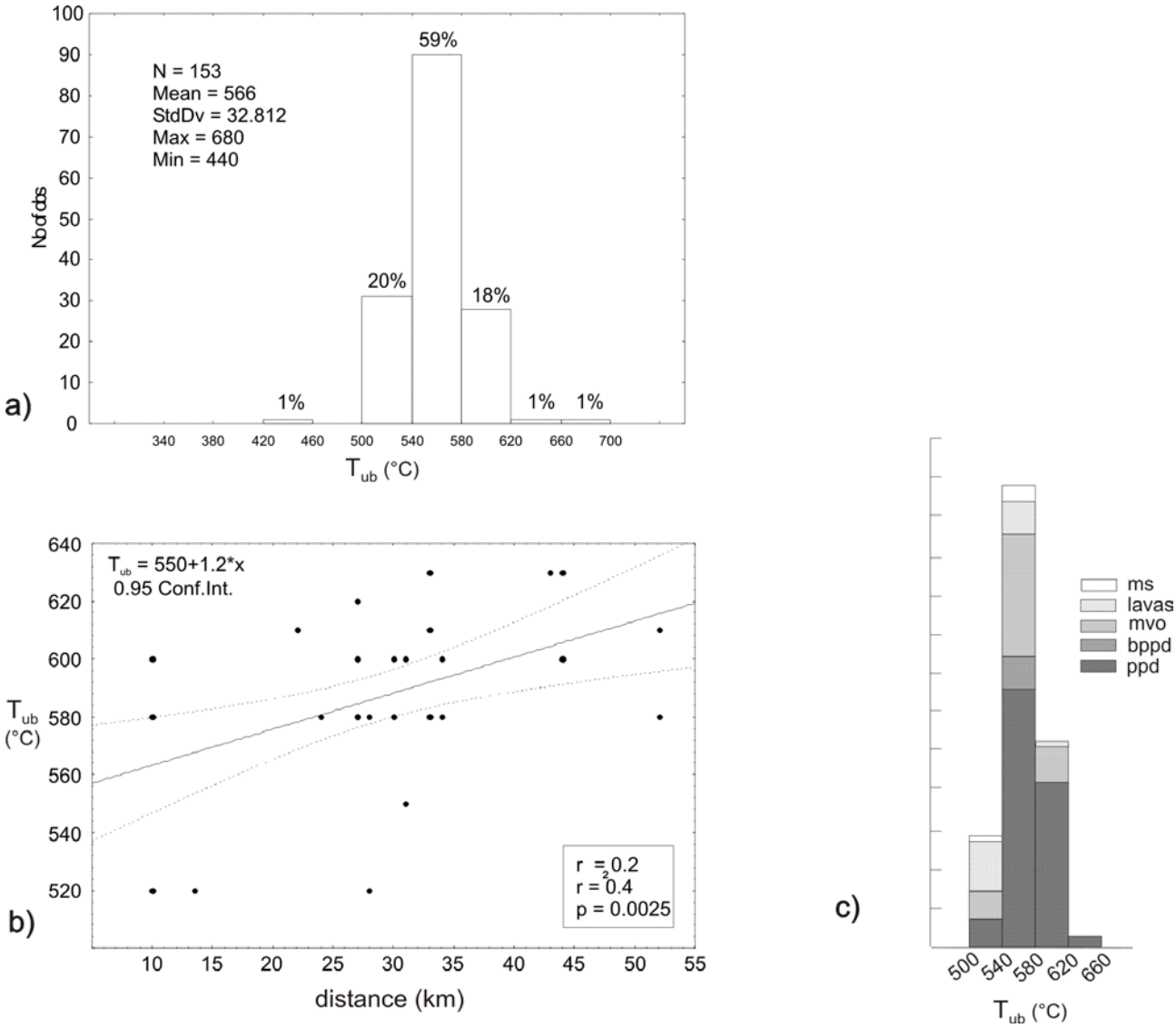

Fig. 4.12 - a) Frequency histogram of unblocking temperatures (T_{ub}) for CGI. Most of the analyzed samples show unblocking temperatures between 540-580°C; b) unblocking temperatures variation with distance; the best fit linear regression gives a slope of 1.2, but the values scatter is wide (r^2 varies between 0-1 for individual points), the correlation coefficient is low (r varies between 0-1 for individual points); and statistical significance is high (p << 0.1%); c) unblocking temperatures variation for the most representative lithologies. ppd: plagioclase-phyric dacite; bppd: black plagioclase-phyric dacite; mvo: meta-volcanic Ordovician; ms: mica-schist

between 540-580°C for all lithologies (in black dacites all T_{ub} values lie between 540-580°C), except for generic lava clasts (which exclude the plagioclase-phyric dacites), in which the mode of T_{ub} values lies in the 500-540°C interval. As reported in the sampling section, plagioclase-phyric dacites (ppd) is the most common lithology between the accidental clasts, though it is not encountered in outcrop outside the caldera. Its origin could be both from proximal lava outflows, ensuring low temperature before ignimbrite emplacement, or possibly from intracaldera dome or conduit. In this case the initial temperature of the clasts could have been higher than ambient temperature. This occurrence does not affect the results anyway, as the ppd unblocking temperatures and demagnetization vector directions are the same as the other lithologies.

The distribution of minimum emplacement temperatures of the Cerro Galán ignimbrite and Real Grande ignimbrite is shown in Fig. 4.13a.

Site emplacement temperatures are evaluated as the maximum T_{ub} among the measured clasts sampled at each site.

Fig. 4.13b shows T_{ubs} for the Toconquis Group units. Unit emplacement temperatures are defined as the maximum site T_{ub} obtained for the unit, except for Lower Merihuaca where the emplacement temperature (T_e) interval is reported.

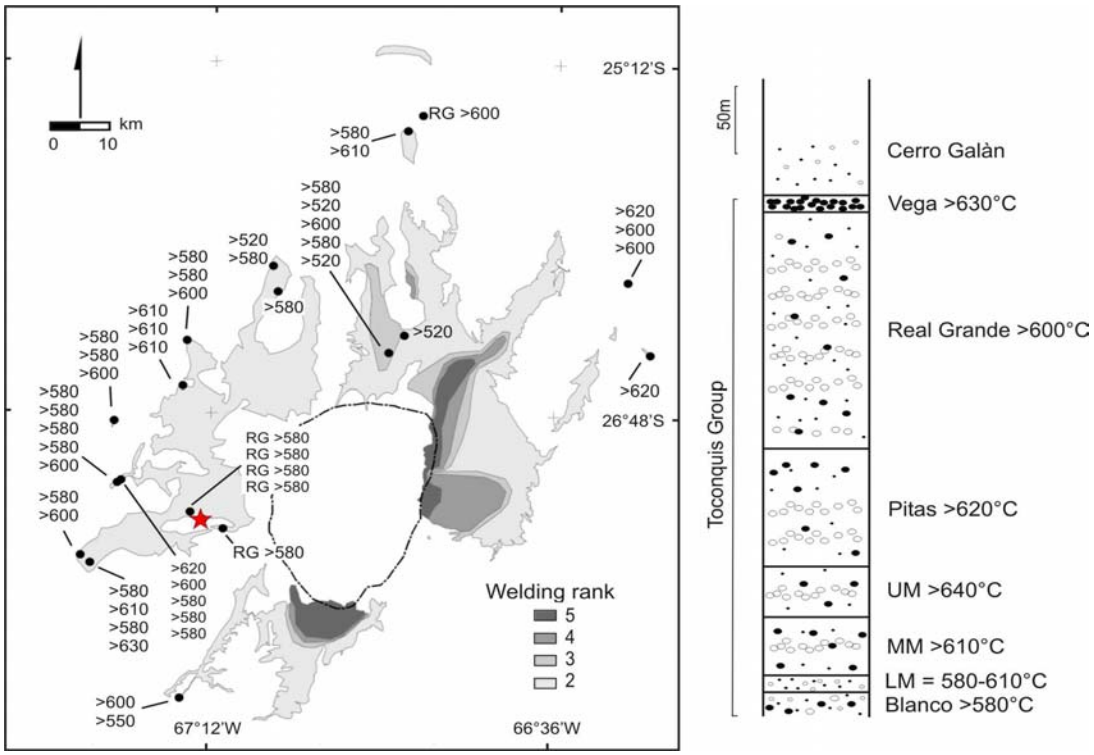

Fig. 4.13 - a) Site unblocking temperature (T_{ub}) areal distribution for Cerro Galán ignimbrite and Real Grande (RG) ignimbrite. Sites ID as in Fig. 4. Welding ranks for Cerro Galán ignimbrite (Ranks II-V) are represented in four gray levels, according to the ranking scheme of Quane and Russell (2004). Note as the highest ranking values (IV-V) are limited to the eastern side of the

5. Flow direction determination by the anisotropy of magnetic susceptibility

In this section are described the paleomagnetic principles and techniques applied to define the magnetic fabric and flow direction of the Cerro Galàn ignimbrite. The analyses were carried out on matrix samples.

Laboratory applications were carried out at the Paleomagnetism Laboratory at Geological Science Department, Roma Tre University, and at the Swiss Federal Institute of Technology (ETH), in Zurich, in collaboration with Prof. Ann Hirt.

5.1. Methodology

The magnetic susceptibility is defined as the proportional parameter between the magnetization of a material and an external applied magnetic field. The magnetization M (in A/m) of the material is proportional to the applied field (in A/m) through the susceptibility parameter **k**.

The induced magnetization is not isotropic, but varies, changing the applied field orientation, as a function of the shape (shape anisotropy) or as a function of the principal crystallographic axis directions (magneto-crystal anisotropy). For this reason the susceptibility is not a scalar, but is defined as a second rank symmetric tensor, and is represented as a rotational ellipsoid, where the principal axes are $K_{max}>K_{int}>K_{min}$ (Fig. 5.1). The plane defined by K_{max} and K_{int} and perpendicular to K_{min} is the magnetic foliation ($F= K_{int}/K_{min}$), while the magnetic lineation ($L= K_{max}/K_{int}$) lies along the K_{max}. The ellipsoid is also described by a series of parameters that define the anisotropy degree (P and Pj) and the shape of the ellipsoid (T). The ellipsoid is perfectly prolate when T=-1 ($K_{max}>K_{int}$ and K_{min}) and perfectly oblate when T=1 (K_{max} and $K_{int}>K_{min}$), while T= 0 correspond to a triaxial ellipsoid.

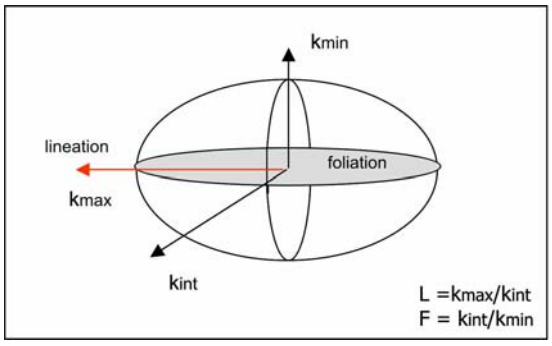

Fig. 5.1 - Schematic representation of the anisotropy of magnetic susceptibility.

The method used to determine the flow direction investigating the anisotropy of magnetic susceptibility (AMS), rely on that commonly the magnetic foliation (F) is parallel to the layering of the rock, that could be stratification, bedding, and that in presence of a moderate flow the orientation of the anisotropy ellipsoid reflects the imbrication of the clasts. Bates and Jackson (1980) defined imbrication as a sedimentary fabric characterized by disk-shaped or elongate fragments dipping in a preferred direction at an angle to the bedding. It is commonly

displayed by pebbles on a stream bed, where flowing water tilts the pebbles with flat surfaces dipping upstream. Early works by Schmincke and Swanson 1967), followed by numerous applications, showed that imbrication of pumices and elongated crystals, is a useful tool for determining the flow direction of pyroclastic flow deposits (Kamata and Mimura 1983).

In the AMS ellipsoid this pattern is shown by the clustering of the k_{min} around the vertical direction and by an up-flow dipping of the magnetic foliation, with respect to the paleotopography. Relating the ellipsoid orientation, interpreted as mechanical imbrication of magnetic minerals in the flow, to the paleotopography gradient, it is possible to retrieve the flow directions. The lineation is usually parallel to the foliation dip but in many cases it was found to be perpendicular to the foliation dip and to flow directions inferred by field indicators (Cagnoli and Tarling, 1997; Rochette et al, 1999; Ort et al, 2003 and references therein). This particular setting is probably due to a mechanical rolling in a high velocity gradient (Rochette et al, 1999), as often reported in sedimentary settings, or to an exchange between similar K_{max} and K_{int}.

The reliability of the AMS methodology to infer flow directions is based on the capability of the magnetic fabric to represent the overall fabric of the ignimbrite. The magnetic mineralogy has to reflect the mineralogical fabric of the ash matrix, to be used as indicator of the flow behaviour. Moreover, the AMS is generally measured in low applied field (10-500 mT) and all the magnetic minerals contribute to the low field susceptibility. To correctly interpret the low field AMS (AMS_{LF}) it is necessary to set in which way each component of the magnetic paragenesis contributes to the AMS anisotropy. If the magnetic paragenesis is oriented following different patterns, the low field AMS would reflect the average of different mechanical behaviour, misleading the results in terms of rock fabric.

5.2. Matrix sampling and AMS laboratory procedures

The study of the flow direction of the Cerro Galàn Ignimbrite was performed on the ignimbrite matrix by the AMS analysis on 403 core specimens, at 35 sites around the Cerro Galàn caldera (Fig. 5.2). On average 12 specimens per site were analyzed, with a maximum of 35 and a minimum of 6. In this paper the term ‘specimen’ is referred to a single piece of a core, measuring 10 cm^3 in volume and 2.4 cm in diameter; a ‘site’ is an outcrop of about 1 m^2 where 7-12 core were drilled; a ‘locality’ is single point on a 1:25.000 map. Specimens are identified by the site number and the core number, and by a letter if more than one sample is obtained from the same core; AMS site numbering is not continuous, as sampling for TRM analysis was conducted simultaneously.

Drilling was carried out by an ASC 280E petrol-powered portable drill on-site (in 25 sites) or afterwards, on oriented block samples (sites 11, 42, 45, 51, 66, 81, 83, 84,104 and 105). The rim gear is made of amagnetic material and it is continuously cooled by water.

The sampled facies were massive with low content of lithic and pumices and high crystal content, generally showing subhorizontal fabric of biotite. The ignimbrite show low degree of

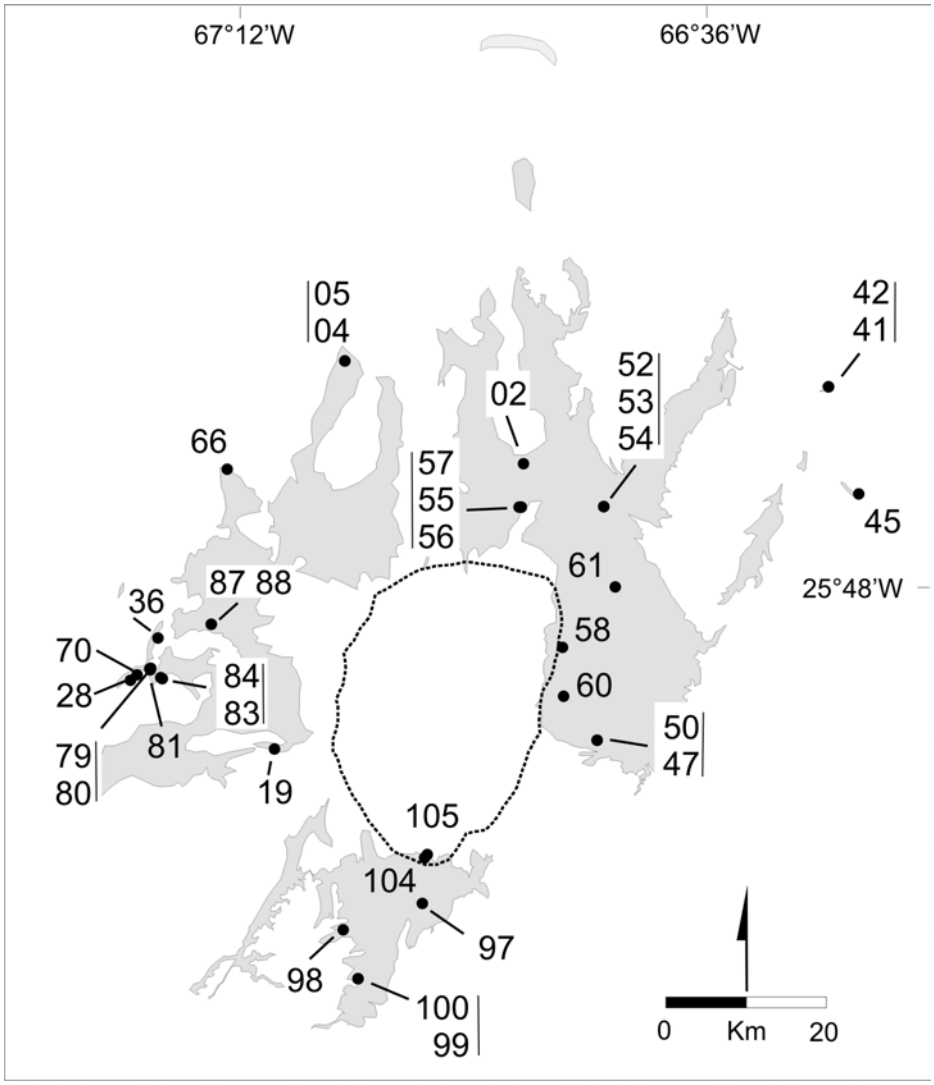

Fig. 5.2 - AMS sampling site location. The areal extent of the Cerro Galán ignimbrite is shown in light gray. Sampling sites located along a stratigraphic section are sided by a vertical line.

welding (Wright et al, submitted) except in the eastern and southern proximal facies, and it is incoherent at the base. For this reason, especially in the western outcrops, sampling was carried out preferably at the base of the columnar jointing, where the facies are more lithified.

At six localities, two or three sites were sampled along vertical section: Bingo Section (sites 52-54) and Diamante Runup (55-57) were sampled at the outcropping base, at

intermediate highs and at the (erosional) top of the section; base and top section were sampled at Dique Trapiche (4inf and 4sup), and S Laguna Grande (99-100). At Curuto (sites 79-80) and Ojos de Curuto (83-84) sampling was carried out at the ridge top and at the correspondent valley floor.

The matrix AMS and the bulk susceptibility were measured by a KLY-3S *kappabridge* at the paleomagnetic laboratory at Roma Tre University. The KLY-3S measures the susceptibility of a spinning specimen fixed in the rotator, applying an external field of 300 Am^{-1} in intensity, with a sensitivity of $2x10^{-8}$ (SI). The specimen rotates with small speed of 0.5 r.p.s. inside the coil, subsequently about the three specimen axes. From these data, the deviatoric susceptibility tensor is computed. This tensor carries information only on anisotropic component of the specimens. For obtaining complete susceptibility tensor one complementary measurement of bulk susceptibility is carried out. The software SUSAR (v. 4.0, 2001) combines the measurements made in the three perpendicular planes and the bulk value to create a complete susceptibility tensor. The errors in the tensor determination are estimated using a method based on multivariate statistics principle.

The results are projected on an equal area projection using the Jelinek 1978) statistics, by the ANISOFT software (v. 4.2,Chadima and Jelinek 2009).

The low field AMS is an estimate of the anisotropy given by the total magnetic paragenesis, both paramagnetic and ferrimagnetic. It is necessary to define the contribution of each mineralogical phase to describe the magnetic fabric. In order to set the magnetic carriers of the Cerro Galàn ignimbrite, selected samples were submitted to high-field AMS analyses, IRM and composite IRM, and thermomagnetic analyses. Selected thin sections were also analyzed by optical and SEM microscope.

The high field AMS (AMS_{HF}) allows the discrimination between the ferromagnetic and paramagnetic contribution to the overall magnetic behaviour. The magnetic torque that acts on a sample is dependent on the magnetic properties of the minerals present in the sample in different ways; it is proportional to the applied field as B^2 for paramagnetic and ferromagnetic minerals, and it is constant above the saturating field of ferromagnetic minerals. Twenty-four specimens were analyzed by the high-field torque magnetometer at the ETH paleomagnetic laboratory in Zurich, following the Martin-Hernandez and Hirt 2001) method. The torque magnetometer measures the deviatoric susceptibility of rocks and minerals in fields up to 1.5 T and it is controlled by a LabVIEW-program. The torque is measured in three mutually perpendicular planes of a rotating sample, every 20°, in four or six incremental fields (each 200mT starting from 900mT or each 100mT starting from 1000mT). Specimens were selected

to maximize the distribution around the caldera and to look for different behaviour between distal and proximal facies and between base and top section facies.

To define the ferromagnetic minerals IRM and thermal decay of composite IRM were performed on one specimen per site, except site 4 and 47, i.e. 33 specimens in total. Samples were firstly saturated along the -z specimen direction by the ASC Impulse Magnetizer at 2T, and then stepwise remagnetized along +z direction by 9 incremental steps, increasing the voltage interval at each step up to an impulse of 2T. The isothermal remanent magnetization was measured by the AGICO JR-6A spinner magnetometer after each magnetization step. The samples were then magnetized along the three directions x y z following the method by Lowrie 1990) to analyze the composite IRM thermal decay. Impulses of 70, 600 and 1100 mT were imposed to each specimen in order to magnetize the soft, medium and hard fraction along the three specimen directions x y z, respectively. The specimens were then thermally demagnetized using an external field shielded furnace with residual fields <10nT, by 13 incremental steps. The remanent magnetization was measured after each step by the JR-6A spinner magnetometer, and the bulk susceptibility was measured by the KLY-3S *kappabridge* to verify if any mineralogical alteration occurred during heating.

Furthermore, magnetic susceptibility was measured as a function of temperature, from room temperature to 700°C in a heating-cooling cycle, on ~2cm3 of powdered sample, using a CS-3 furnace apparatus connected with the KLY-3S *Kappabridge*. This analysis was made on selected specimens from 10 different sites in order to define the magnetic mineralogy and verify any mineralogical change with temperature.

Finally, the overall mineralogy was investigated on 10 representative oriented thin-sections by optical microscope and on 3 thin sections by SEM microscope. Thin-sections were made along the magnetic foliation plane (K_{max}-K_{int}) determined by AMS analyses. Six to ten zoomed pictures were taken randomly from each thin-section on the optical microscope and image analyses were performed on a representative picture for each thin-section. After treatment by the software ImageJ (v 1.141 by Wayne 2008), the output b/w pictures were analyzed by the intercept method (Launeau and Robin 1996) in order to make a comparison between the direction of the magnetic lineation (K_{max}) and the mineralogical alignment. The intercept method is based on counting the number of segments determined within a set of objects cut by a set of parallel scan lines along a series of directions on a 360° grid and the results are represented by the Fourier series approximation on rose diagram, where it is possible to determine principal directions. As in Plenier et al. 2005) the comparison is only indicative, and does not want to be representative of the overall flow direction, but can be

used to evaluate the reliability of the AMS results as indicative of the overall fabric of the ignimbrite.

5.3. Matrix magnetic mineralogy - results

The magnetic paragenesis is fundamental to correctly interpret the results of the main methodologies applied in this study.

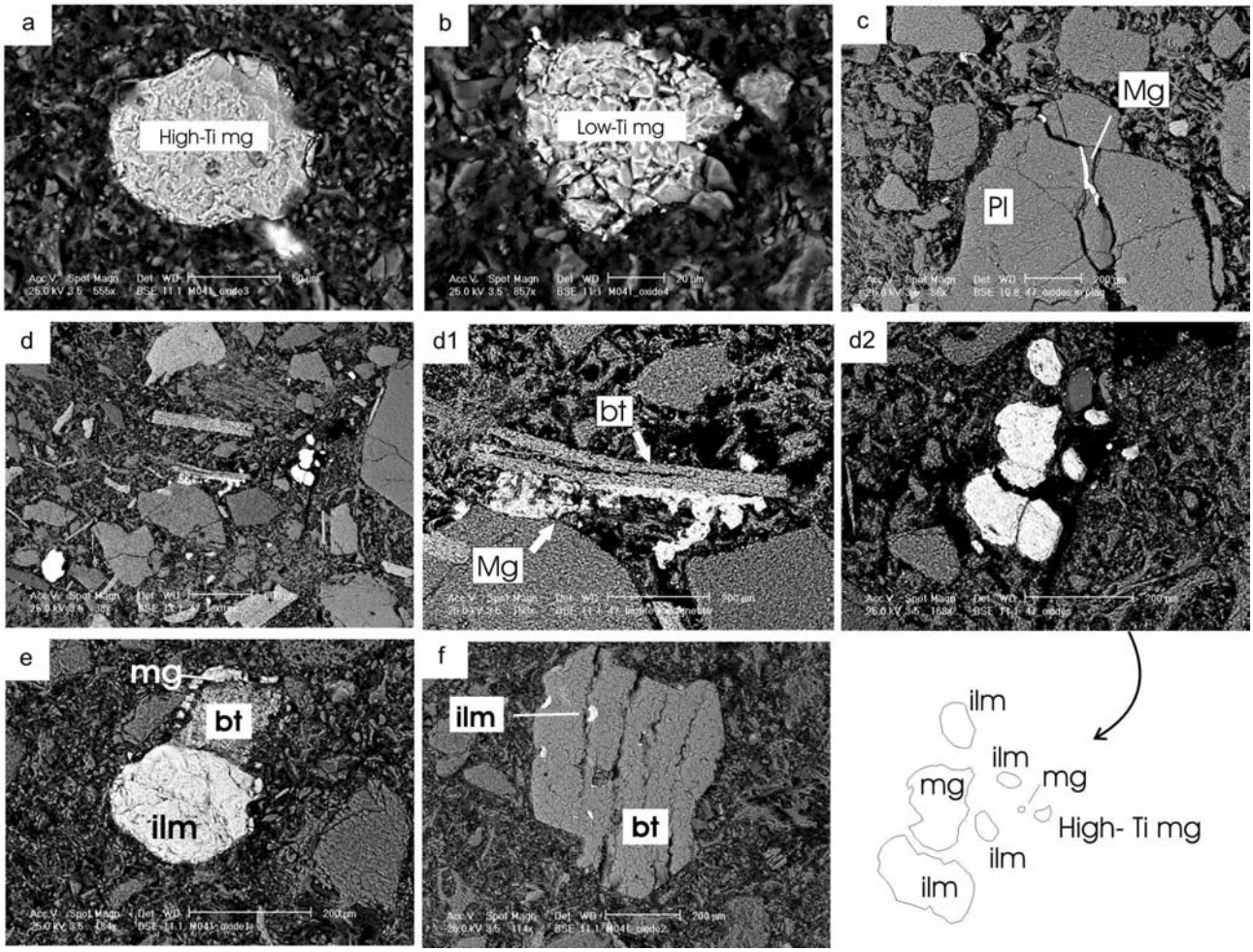

Fig. 5.3 - Thin sections SEM images. The image plane corresponds to the AMS foliation plane. a-b) spherules of magnetite with different titanium content; c) magnetite infilling discontinuities in a plagioclase crystal; d) coaxial growth of magnetite mimicking biotite shape (enlargement in d1) and spherules of ilmenite and magnetite with various amount of Ti in solid solution (enlargement in d2); e) ilmenite grain and overgrowth of magnetite along the biotite margins; f) ilmenite intergrowth in biotite.

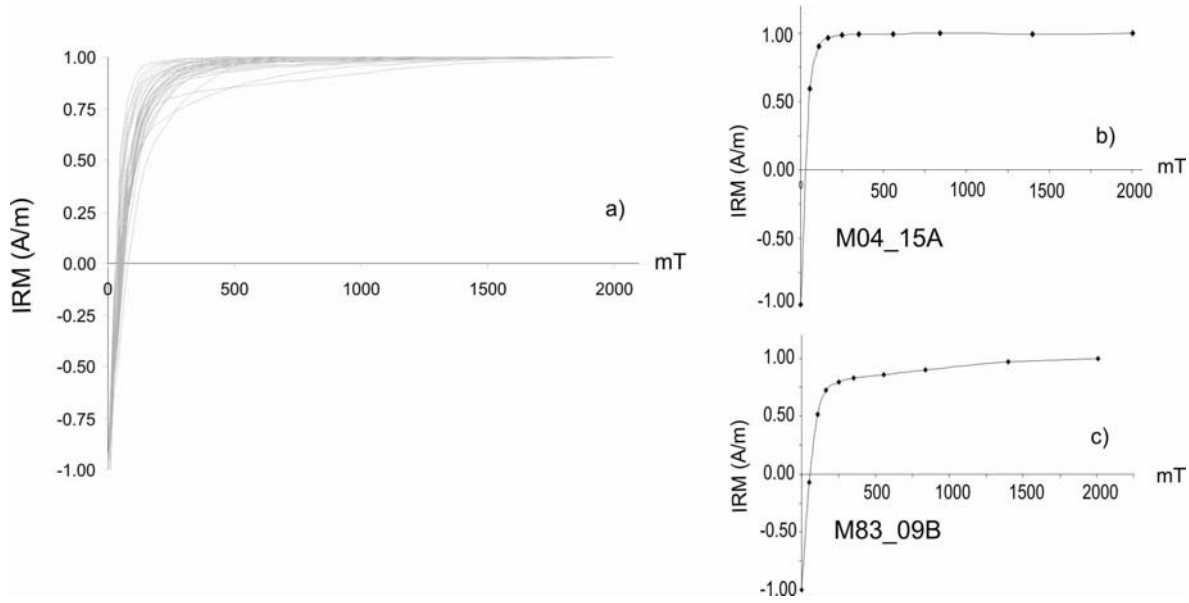

Fig. 5.4 - a) Isothermal remanent magnetization (IRM) analyzed in 33 representative samples. 95% saturation is reached at 350-400mT in most of the analyzed samples, as in shown in sample M04_15A (Fig 4b); three samples did not reach saturation at the maximum applied field (2T), as shown by the curve in Fig 4c. The IRM procedure followed in this study provides information on the field needed to saturate the magnetization as well as the coercivity of remanence. The overall remanent coercivity H_{cr}, is between 30 and 79 mT.

The main components of the Cerro Galàn ignimbrite are plagioclase, biotite, and quartz with minor hornblende, apatite, zircon and Fe-Ti oxides. Plagioclase, quartz, apatite and zircon are diamagnetic and do not contribute substantially to the bulk magnetic susceptibility. Biotite and hornblende are paramagnetic minerals, while Fe-Ti oxides show ferromagnetic (*sensu lato*) behavior.

The ferromagnetic fraction, analyzed by qualitative microprobe connected to the SEM, is composed by ilmenite and magnetite low or high in Ti, dispersed in the matrix as spherules 100-200 μ in diameter, or showing a mimetic growth coaxial with primary paramagnetic fabric, along the crystals margins or fractures (Fig 5.3). There is no evident pattern in the distribution of the spherules, therefore are the oxides mimicking the crystals that drive the AMS_{LF}.

The results of the isothermal demagnetization (IRM) show that most of the samples saturate at low fields, between 250 and 550mT (min 160 and max 850mT), with an H_{cr} field between 40 and 60mT (Fig 5.4). Low saturation and low H_{cr} indicate a prevalence of low coercivity minerals like magnetite, ilmenite and Ti-magnetite. Three specimens, from sites 4, 36 and 88, saturates at higher field (1400mT) and show a higher H_{cr} field (up to 79 mT) for the presence of a higher coercivity phase as hematite.

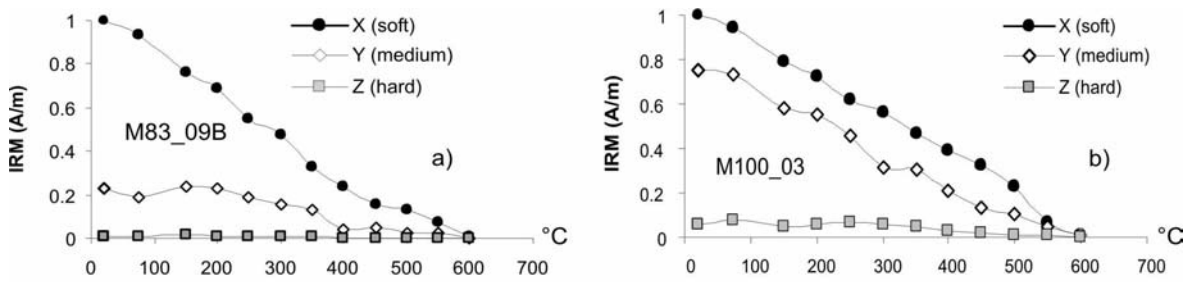

Fig. 5.5 - Representative thermal decay of composite IRM for 2 samples. The soft fraction prevails in all the 33 analyzed samples. a) Soft fraction decay at 580°C is indicative of the presence of magnetite; b) the hard fraction always less than 20% of the soft fraction

The predominance of low coercivity fraction is confirmed also by the thermal decay of the composite IRM analysis. The field that magnetized the soft fraction was set very low to isolate the magnetite and ilmenite, while in the medium fraction are comprised phases with various amount of Ti in solid solution. The soft fraction (magnetite and ilmenite) is prevailing in almost all samples (Fig. 5.5). The hard fraction, in all the analyzed specimens, is absent or very low, up to a maximum of 15% in few samples.

The thermomagnetic curves (Fig. 5.6) show that there is no modification of magnetic mineralogy when the samples are heated, as the heating and cooling curves are correspondent.

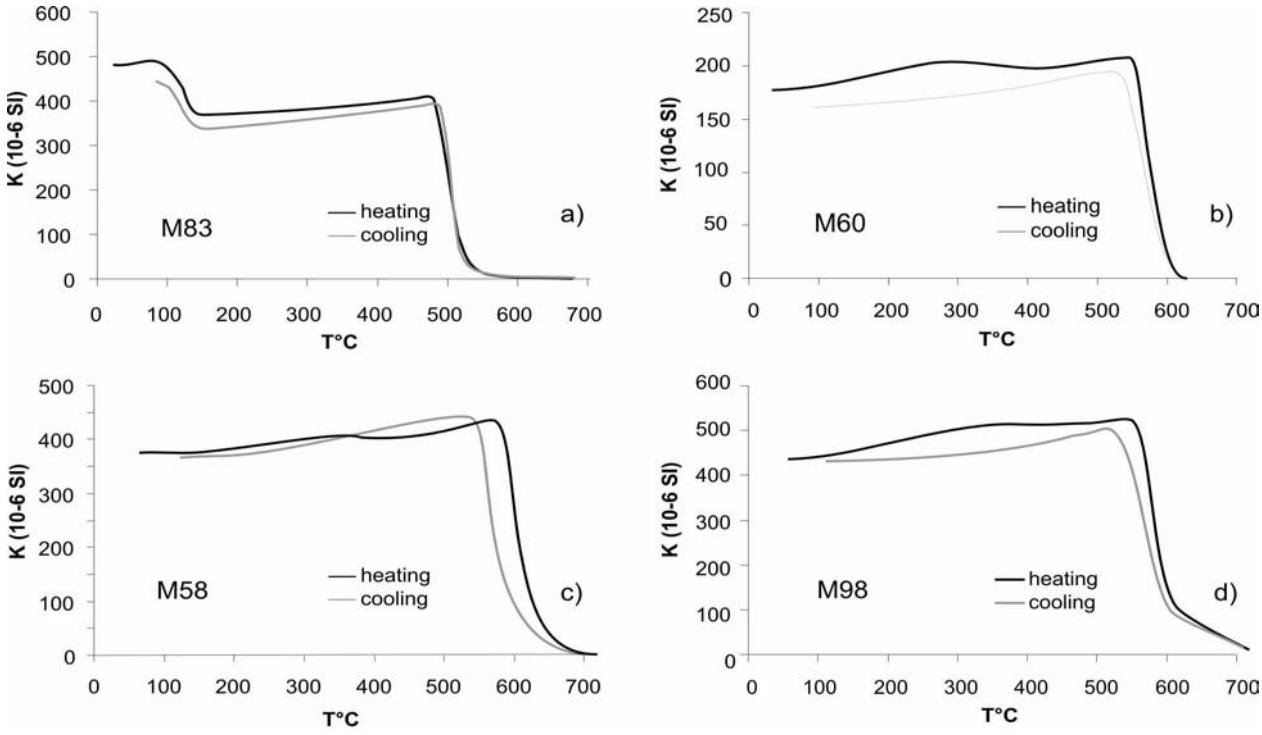

Fig. 5.6 - Representative thermomagnetic curves. Most of the analyzed samples show good correlation between heating and cooling curves, indicating that there is no mineral formation during the heating process; steep decays represent Curie temperatures of magnetic minerals; a) Curie temperatures at 550°C indicate the presence of Ti-magnetite; b) Curie temperatures at 580°C indicate the presence of magnetite c-d) Curie temperature at about 620°C indicate the presence of hematite. In d) the presence of hematite is more relevant

Curie temperatures again address to Ti-magnetite (Fig 5.6a), magnetite (Fig 5.6b), and some hematite (Fig 5.6c and 5.6d)

The magnetic fabric is therefore due prevalently to paramagnetic minerals, mostly biotite, and secondary by ferromagnetic minerals, i.e. ilmenite and magnetite with various amount of Ti in solid solution.

5.4. Anisotropy of magnetic susceptibility data

As reported in the sampling section, the study of the anisotropy of magnetic susceptibility was carried out on the Cerro Galàn ignimbrite, and not on the ignimbrites of the Toconquis Group, as the outcropping extent of the older ignimbrites is limited to Vega Real Grande section, west to the caldera.

5.4.1. Low field AMS Results for the Cerro Galàn ignimbrite

The mean magnetic susceptibility (K_m in Tab 5.1), which estimates the sum of the paramagnetic and ferromagnetic contribute, range from 1.06 to 14.8 x 10^{-3} SI. The instrumental error is 0.08 on average, mostly less than 0.01%. The statistical distribution of the K_m reveal three peaks at 4, 7 and 11 x 10^{-3} SI.

The shape of the anisotropy ellipsoid is mostly triaxial to oblate-triaxial (the shape parameter T ranges from 0.147 to 0.753) with well-defined foliation (Fig 5.7). The anisotropy degree (P) ranges between 1.021 and 1.214. Magnetic foliation is always well defined, while magnetic lineation is either clustered (E_{1-2} < 30° in 25 sites, Tab. 5.1) or dispersed along the foliation plane (E_{1-2} > 30° in 10 sites) (Fig 8). At site 41, two orthogonal population of L were measured. The lineation is parallel to the foliation dip in most cases, while in a few sites is dispersed along the foliation or orthogonal to dip direction.

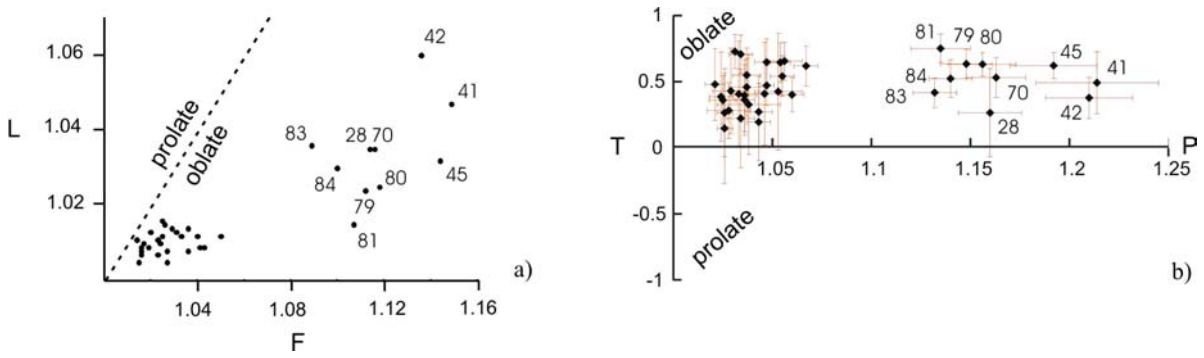

Fig. 5.7 - Anisotropy parameters of the 35 site. *Site numbers are specified only where higher values are found. a) L-F diagram; b) T-P diagram. All the analyzed samples are oblate in shape.*

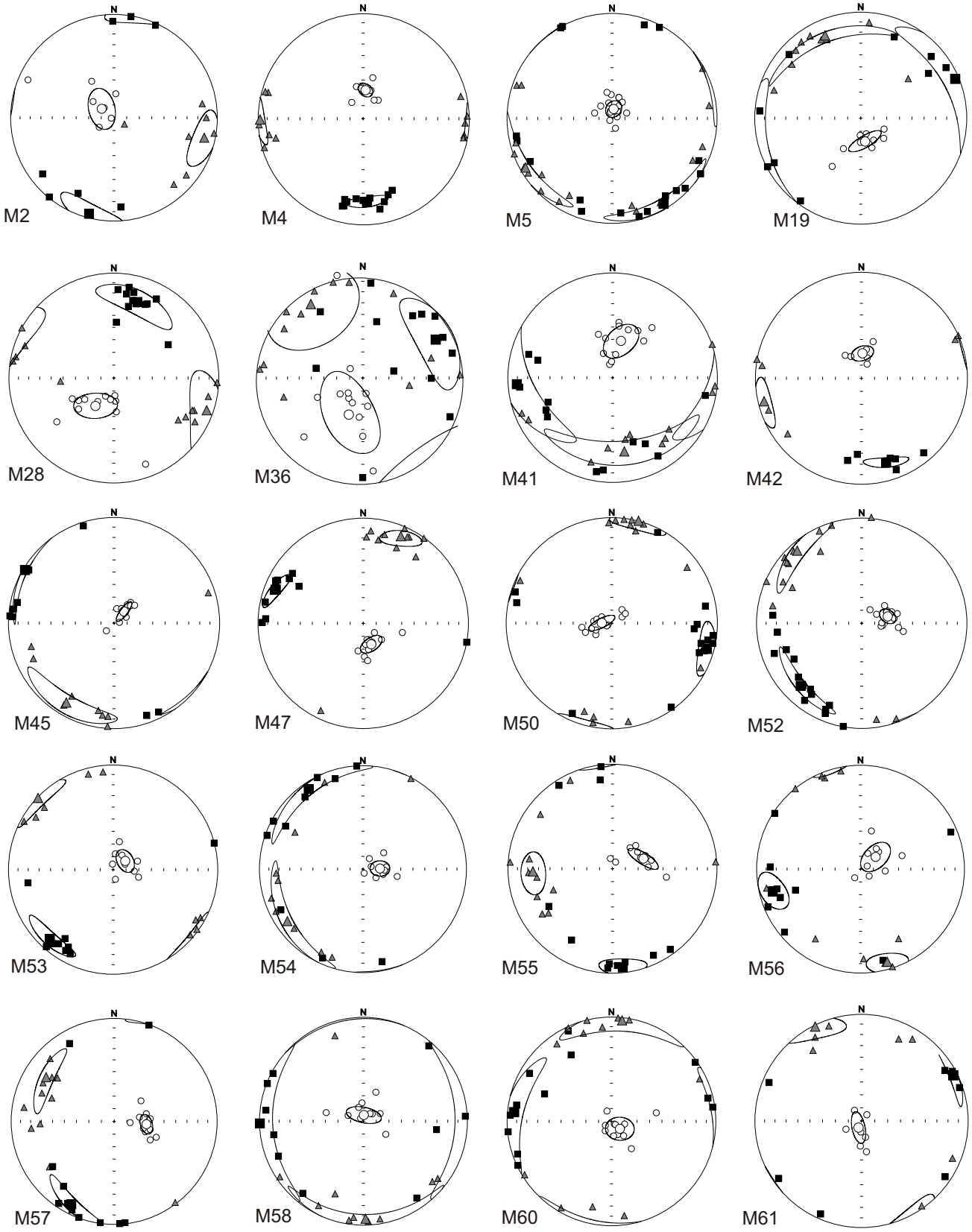

Fig. 5.8 - Stereonets of the AMS ellipsoids from the Cerro Galàn ignimbrite. Equal area projection in geographic coordinates.

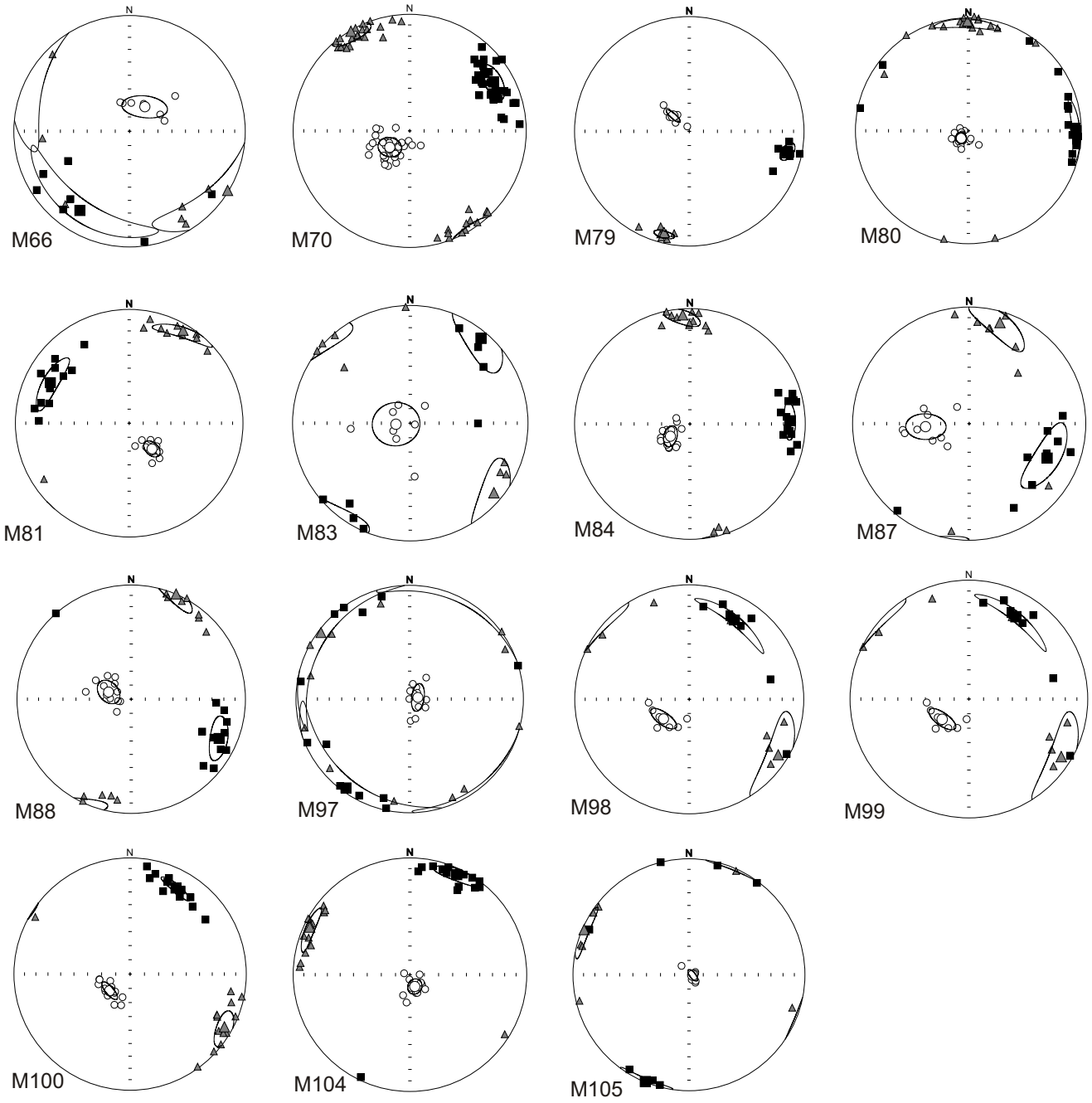

Fig. 5.8 - continued

5.4.2. High field AMS Results for the Cerro Galàn ignimbrite

The AMS_{HF} results show that both paramagnetic and ferromagnetic fractions contribute to the amagnetic susceptibility of the Cerro Galàn matrix. In all the analyzed samples the paramagnetic fraction (mainly biotite) is predominant, varying between 66% and 85%, 72% on average. The ferromagnetic fraction contributes for a minimum of 14% and a maximum of 34%, 26% on average.

The minimum susceptibility axes (K_{min}) of both paramagnetic and ferromagnetic fraction obtained by the high field analysis, coincide in all samples with the K_{min} of the low-field AMS, while the K_{max} and K_{int} appear coincident (between them and with the low-field axes) or dispersed on the foliation plane in few cases (Tab. 5.2 and Fig. 5.9). Clustered and girdle axes can be found at the same site, within a distance of few centimeters, as specimens 50_01A and 50_04B (Fig.5.9). The low field anisotropy orientation is therefore related to both paramagnetic and ferromagnetic minerals, as they show coaxial susceptibility.

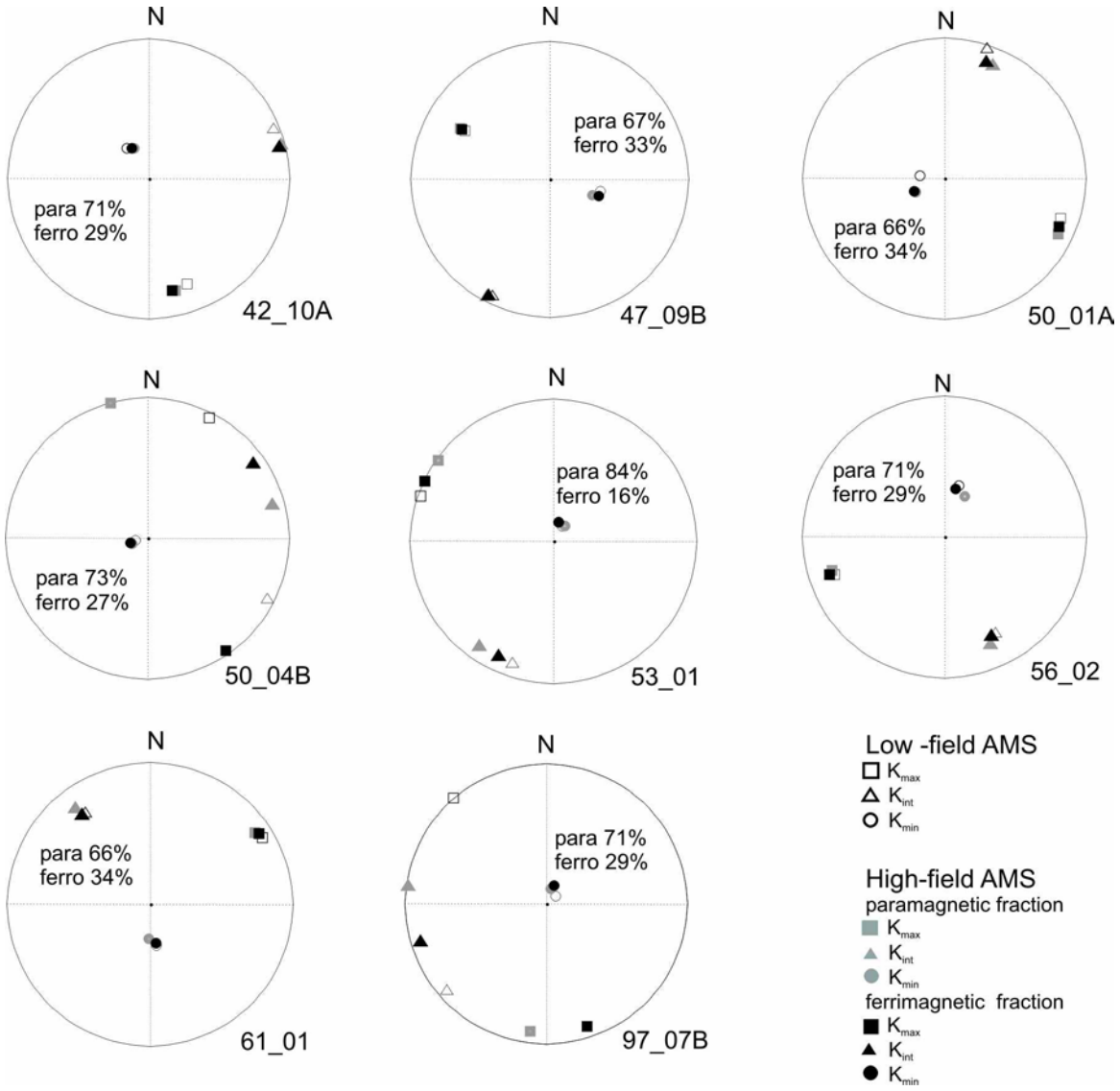

Fig 5.9 - High field AMS results. Equal area projection (lower hemisphere) of the principal axes of the low field AMS (white symbols) and high field paramagnetic and ferromagnetic fractions (gray and black respectively). Paramagnetic (para) and ferromagnetic (ferro) contribution are reported in the inset. Data are projected onto the lower hemisphere of an equal area projection in geographic coordinates.

5.5. Image analysis

Image analysis was performed on ten representative matrix specimens. Thin sections were made along the magnetic foliation plane in order to identify preferential crystals alignment, if any, produced during emplacement. As reported in the previous section, both paramagnetic and ferromagnetic contribute to the AMS_{LF}. For this reason we can apply image analysis on one single mineral component as representative of the mineralogical fabric to explore the relationship between magnetic and mineralogical lineation. The image analysis was performed on the biotite grains. Besides being the paramagnetic component that gives the highest contribute to the magnetic anisotropy, the biotite grains are also good indicator of the mineralogical fabric due to the higher shape anisotropy respect to the other macro-crystals of the ignimbrite (quartz, plagioclase). In Fig 10 are reported for each analyzed specimen, the thin section image, the b/w image, and the result of the intercept application; finally are plotted the site AMS_{LF} results and the alignment direction obtained by the intercept application. In most cases the magnetic lineation correspond with the principal alignment direction. The comparison between the magnetic lineation and the mineralogical lineation shows that there is always strong correspondence, in the range of 10-20° between the two lineations. In the sample 02_02A the principal direction of the biotite grains is N53°, followed by a second N-S alignment. The main direction corresponds to the larger biotite grains and it is at fifteen degrees from the magnetic lineation, while the second direction is relative to the smaller grains. In sample 42_09B only one principal direction is identified on the biotite grains at N140° and magnetic an mineralogical lineation is almost perfectly correspondent. This is valid also for the specimen 28_07A. In sample 19_05A two directions of the biotite grains are identified, with almost the same intensity. In this case there is a stronger correspondence of the magnetic lineament with the less frequent direction. The same pattern is shown in the 41_06B specimen. The specimen 47_09B shows less biotite grains alignment, and three main directions are identified, with almost the same intensity. Anyhow there is a good correspondence with the average direction at N65°.

The strong correspondence between the magnetic and mineralogical lineation indicates that the AMS_{LF} field it is a good representation of the fabric of the ignimbrite.

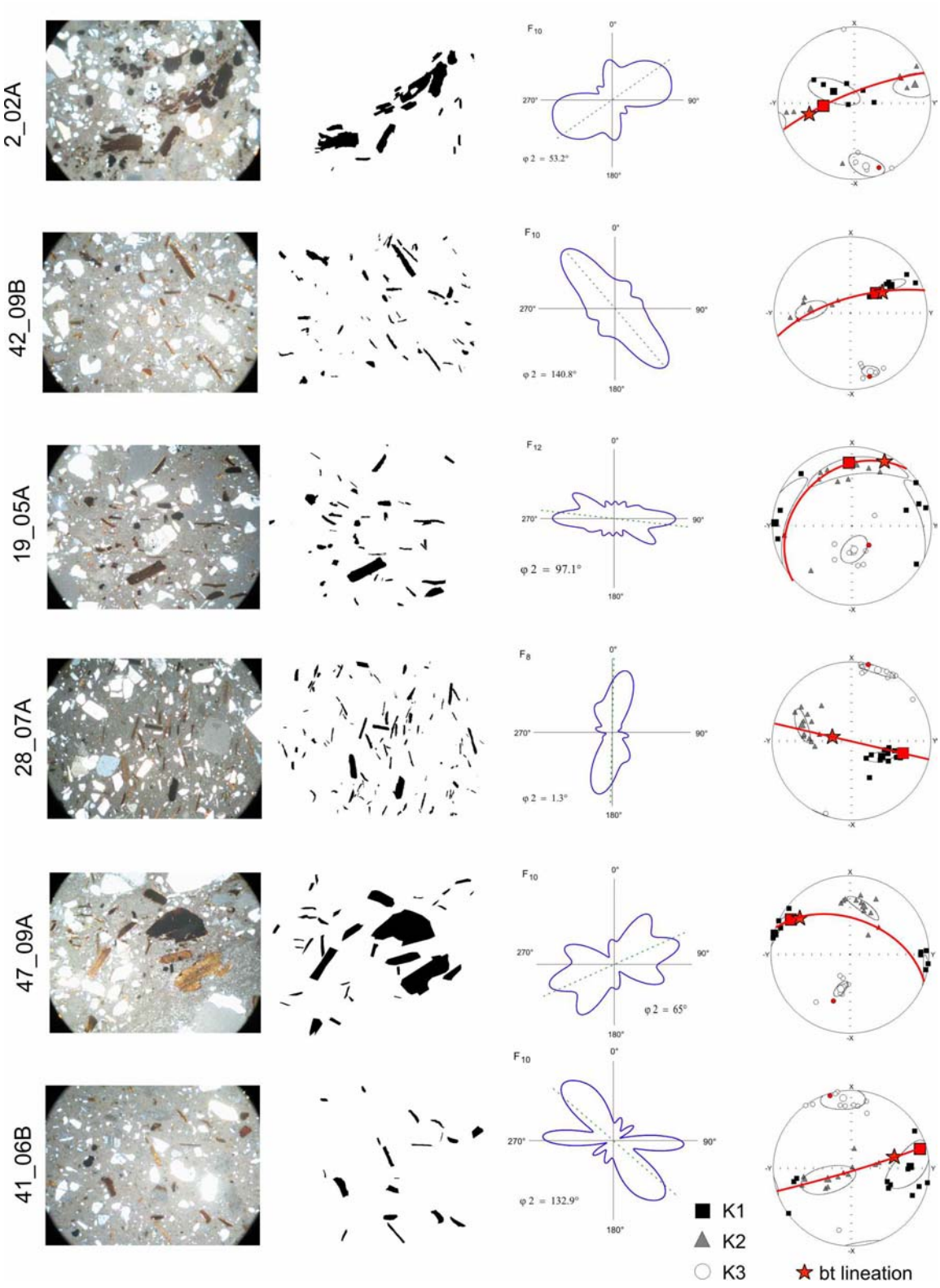

Fig. 5.10 - Image analysis on thin section along magnetic foliation. For each analysed specimen it is illustrated the thin section image, the b/w interpreted image (in black are outlined the biotite grains), and the result of the Intercept application; the resulting angle is projected together with the site AMS_{LF} results on an equal area projection in specimen coordinates. Highlighted in red are the principal axes of the specimen analyzed in thin section.

5.6. Definition of flow directions

The magnetic foliation is always well defined, and subhorizontal. Generally the foliation planes show a few degree of inclination, which are proved to be at an angle respect to the inclination of the local paleotopography. The analysis in thin section of oriented samples illustrates that the AMS foliation plane actually replicates the physical organization of magnetic grains within the ash matrix. This observation allows relating the AMS signal to the sedimentological texture of the matrix and therefore to use the AMS foliation plane as an indicator of the microscopic fabric. On this basis it is possible to interpret the dip of the foliation as the mechanical imbrication, and therefore infer the AMS data in terms of ignimbrite flow direction.

The variability of the magnetic parameters is indicative of changes or evolutions in the ignimbrite fabric, and can give some clues on the general flow evolution along its path.
The foliation values are distributed into two main clusters, which are even better defined by the anisotropy degree. Comparing the anisotropy degree with the susceptibility, three clusters appear well defined (Fig. 5.11).

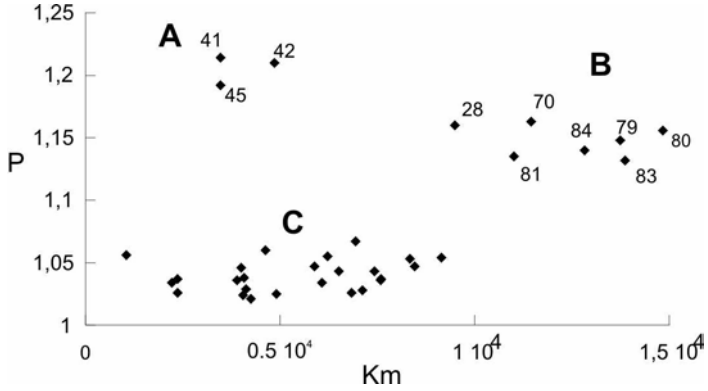

Fig. 5.11 - Site P-K_m diagram. Site numbers are reported only for group A and B. Differences in K_m (in 10^{-6} SI units) between group A and group B are probably related to the amount and lithology of accidental clasts.

There is not great variation in the parameters values at different azimuth around the caldera, except in the case of the anisotropy degree P. In Fig. 5.12 is shown the anisotropy parameters variability with the distance from the caldera. The P parameter is analysed in four sectors (N; E; S and W). Differences in anisotropy degree are higher within section (sites 52-54), and less in top/bottom valley facies (sites 79-80 and 34-33). A strong gap is evident in the two eastern and western sites. At the same distance, 40-50 km from the caldera, the variability is higher in the eastern and western sectors, than in the northern and southern sectors. This difference is less evident for the other parameters, which are shown only in function of the distance.

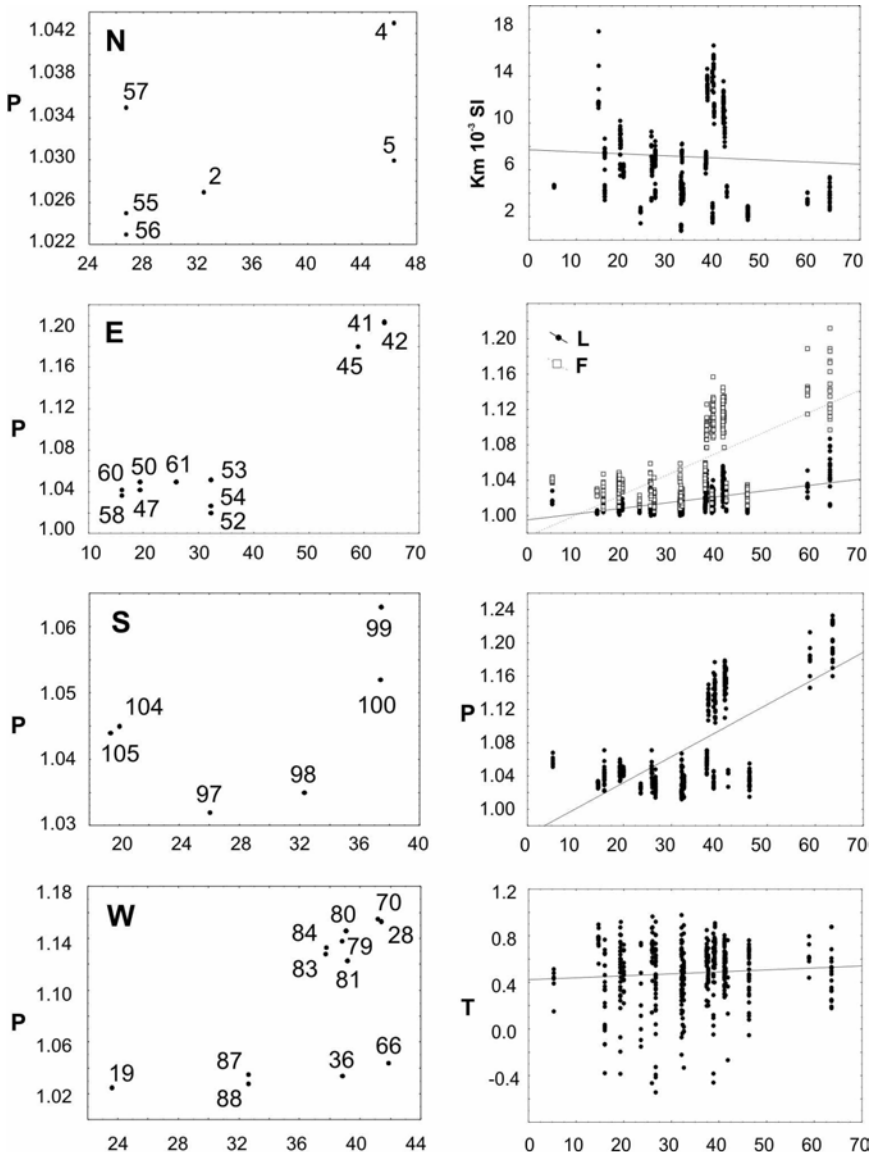

Fig. 5.12 - Anisotropy parameters variation with distance. In the first column the site variability (35 sites) of the P parameter is shown along the north, east, south and west direction. In the second column is shown the specimen variability (420 specimens) of magnetic susceptibility K_m (10^{-3}SI); lineation L (k_{max}/k_{int}); foliation F (k_{int}/k_{min}); anisotropy degree P: (k_{max}/k_{min}) and shape parameter T ($2\eta_2 - \eta_1 - \eta_3)/(\eta_1 - \eta_3$), where $\eta_2 = lnk_{int}$; $\eta_1 = lnk_{max}$; $\eta_3 = lnk_{min}$. note that the horizontal and vertical scales are different in each plot.

The values of the magnetic susceptibility K_m are fairly constant and show no systematic variation with distance from the caldera. The highest values are encountered in Paicuqui-Curuto area, west of the caldera, probably relating to the type and abundance of accidental lithics.

There is a slight positive trend in the lineation with the distance. To note is the higher lineation values between top and bottom of the same section. The lineation at the base is always higher at sites 4 (base) and 5 (top), 99 (base) and 100 (top), and also at valley floor (80 and 83) than at ridge top (79 and 84) (Tab 5.1). As for the foliation, a strong increment is evident in the two medial-distal groups to the E and to the W, while to the north and to south

there is no trend with the distance. Differences from top and base section are less evident, and absent at 99-100 sites (Tab 5.1). On the contrary, a distinction in the shape (prolate/oblate) is evident more at the section scale than with the distance, though is opposite between sites 4 - 5 and 99 - 100. To note that there is no shape differences between top ridge and valley floor at sites 79-80 (Tab 5.1).

In summary there are not evident trends of the anisotropy parameters with the distance, except a strong increment in the anisotropy degree in the Paicuqui-Curuto and Tacuil-Hualfin sites. Furthermore, the magnetic paragenesis appears to be constant from proximal to distal sites, as no variations occurred in the paramagnetic and ferromagnetic content along the ignimbrite path.

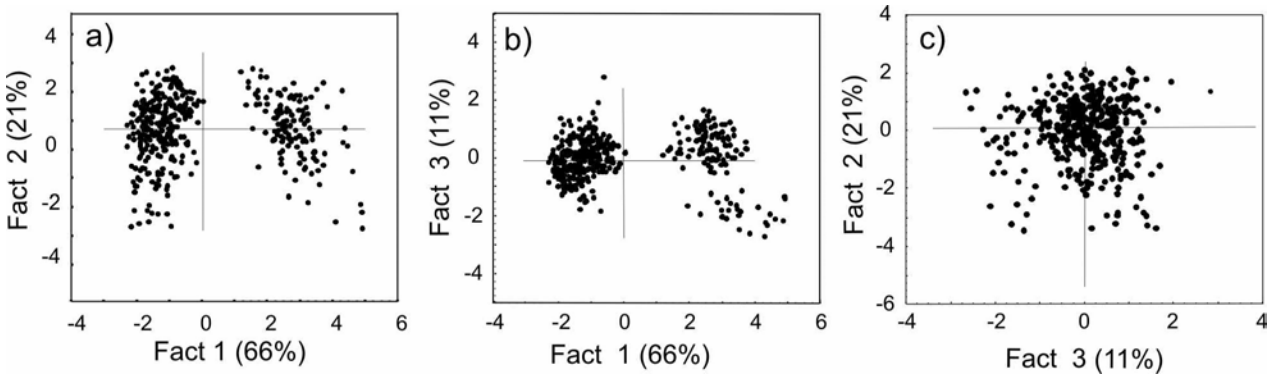

Fig. 5.13 - Factor analysis on the anisotropy parameters. The distance from the caldera is the independent value; factor 1 represent the 66% of the total variability, while factor 2 and 3 represent the 21% and 11%, respectively. b) factor1 - factor2 diagram; c) factor1 – factor3 diagram; d) factor2 – factor3 diagram;

A factor analysis was additionally carried out to define which are the parameters that mostly contribute to the variability of magnetic properties between sites, taking the distance as the independent value (Fig 13).

The first three factors comprise 98% of the total variability, and further factors were therefore discarded. The anisotropy degree P gives the higher contribution to the first factor, which contributes for the 66% to the overall variability, while the shape factor T and the susceptibility K_m give the higher contribution to the second and third factors, respectively (Tab 5.3). Two clusters are present when comparing factor 1 with both factor 2 and 3, that are not well defined when comparing factor 2 and 3

parameter	*Fact. 1*	*Fact. 2*	*Fact. 3*
Km	0.59	0.3	0.74
L	0.8	-0.53	0
F	0.97	0.11	-0.14
P	0.99	-0.05	-0.12
T	0.21	0.93	-0.24

Table 5.3 - Factor analysis. Anisotropy parameters weights in each factor. Negative values indicate inverse correlation

(Fig. 5.13).

The higher variability between sites is due to the anisotropy parameter P, by which sites can be grouped in low-anisotropy (P = 1.020-1.058) and high-anisotropy (P = 1.138-1.204) degree. Sites with high anisotropy degree are localised in the Tacuil-Hualfin area, NE to the caldera, and in Paicuqui-Curuto area, west to the caldera. These are the areas where it is strongest the paleotopography control on the flow, where the ignimbrite found its path trough the paleovalleys.

Two different settings are in fact derived from the analysis of the imbrication of the magnetic foliation: proximal and medial-distal facies (Fig. 5.14). In proximal areas, within about 15 km around the present caldera rim, the ignimbrite follows a radial path. Sites 58, 61 and 97, characterized by a sub horizontal fabric, as the dip of the foliation is very low and the height in the section is unknown (the base is not visible), the lineation was taken as the flow direction indicator. Also 55 and 57, where a high NNE-SSE basement ridge borders the flow, the lineation is taken as flow direction indicator. The distal facies, more than 15 km away from the present caldera rim, are instead characterized by a strong influence of the paleotopography on the flow. There is anyway a distinction between the northern and southern sectors, and western and eastern sectors. NNE-SSW trending relief that borders the caldera to the east and to the west dominates the structural framework of the area. A high basement outcrop is also bordering the ignimbrite to the north, proximal to the caldera, as mentioned above. So, while to the north and south the flow persisted following a radial path, to the east and to the west was strongly deflected by the paleotopography.

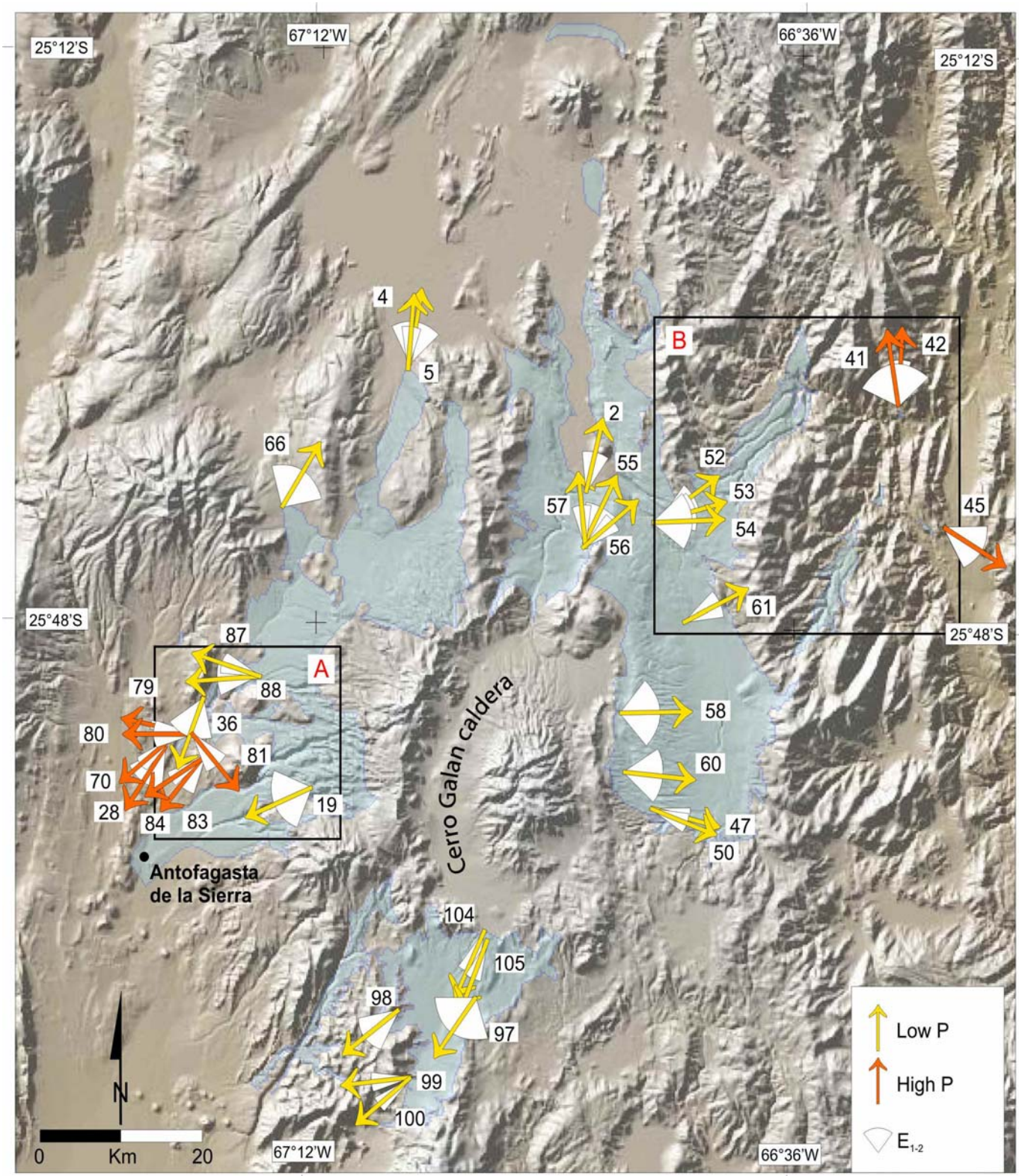

Fig. 5.14 - Map of interpreted flow directions of the Cerro Galàn ignimbrite. In light blue is the CGI extent; arrows are the CGI interpreted flow direction; arrows color indicate low-anisotropy (P = 1.020-1.058) and high-anisotropy (P = 1.138-1.204) degree; white sector is the E_{1-2} error on the magnetic foliation plane. A and B insets are enlarged in Fig. 5.15.

The ignimbrite is limited toward the west by the Tebenquicho Formation relief, where there are traces of the ignimbrite on the Rio Punilla right hand slop. At Cerro Beltràn the flow is deflected to the north, toward the present Salar del Hombre Muerto (site 66). More to the south, the ignimbrite is deflected to the SW (Fig 15a), from a proximal direction toward the west (Puntas Negras sites 87 and 88), through the paleovalleys traced by Rio Punilla (site 36) and its left hand affluents Rio Toconquis and Rio Merihuaca. In the Paicuqui-Curuto area the general paleotopography gradient is to the SSW and again, from a westward direction at Ojo

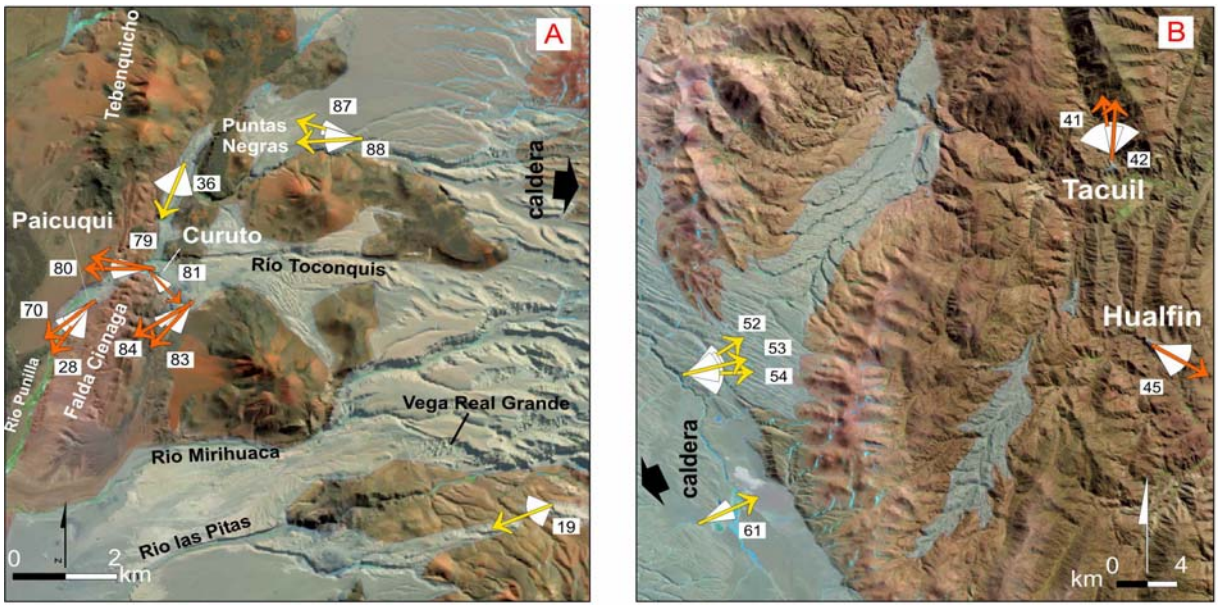

Fig. 5.15 - Enlargements of map in Fig 5.14. A: Paicuqui-Curuto area, west to the caldera; B: Tacuil-Hualfin area, NE to the caldera.

de Curuto (sites 83 - 84) and at Curuto (sites 79 - 80), the flow is deflected to the south at Paicuqui (sites 28 and 70). At Curuto, site 81, the flow is directed to the south, choosing a valley parallel to the Rio Punilla, following the structures of the low metamorphic Falda Cienaga Formation.

On the other side of the caldera, in the northeastern area of Tacuil-Hualfin (Fig 15b), the distal facies are influenced by the paleotopography in the same way as in the western side area. From a direction toward the E and ENE in proximal-medial facies (site 61 and sites 52-54) the ignimbrite is canalized through the valleys of the Calchaquì area, west to the Rio Calchaquì. The ridges are N-S trending and the flow follows the valley upslope to the north at Tacuil (site 41-42), and a transversal valley toward the SE at Hualfin (site 45).

In summary, the AMS of the Cerro Galàn ignimbrite records radial paths in proximal facies and, in distal facies, as far as about 80 km from the caldera rim, the AMS show how the deposition was strongly influenced by the paleotopography.

6. Emplacement mechanism – a model

The results of the TRM analysis carried out on the Cerro Galán and Toconquis Group ignimbrites revealed emplacement temperatures higher than 600°C in most cases.

High emplacement temperatures in pyroclastic flow deposits were found worldwide, both by mean of direct measurement and indirect analysis. In Guadeloupe, in the 37 ka *nuée ardente* of La Créte à Bambous, Zlotnicki et al. (1984) found emplacement temperatures up to 530°C. For the 1993 eruption of Volcán de Láscar in Chile, Paterson et al. (2010) retrieved emplacement temperatures of the pyroclastic flow exceeding the Curie temperature of magnetic minerals (>400°C) up to 8.5 km from the source. At Soufriere Hills, Montserrat, Calder et al. (1999) directly measured temperatures up to 650°C, while Scott et al. (2008) found temperatures in the range of 400-610°C by the analysis of vitrinite reflectance. Direct measurements of Mt. St. Helens 1980 deposits (Banks and Hoblitt 1981) indicated a settling temperature of the 22 July eruption of 705°C, 6.9 km far from the vent. Moreover, numerical simulations of small to large volume pyroclastic flows also indicate that the deposits may retain high temperatures (Giordano and Dobran 1994; Todesco et al. 2006).

TRM data constrain the thermal structure of the Cerro Galán ignimbrite immediately after deposition at T>580-620°C, along the entire extent of the preserved deposit (maximum distance investigated is 52 km from caldera rim), and also along vertical sections (max 60 m thick).

In addition, the TRM analysis of specimens obtained from the core and the rim of a single large lithic clast shows that the thermal behaviour is homogeneous throughout the clast. Using the heat transfer model of Carslaw and Jaeger (1959), Bardot (2000) estimated that clasts sized between 2 and 10 cm, initially at ambient temperature, will reach thermal equilibrium with the medium after 10^2 - 10^4 sec respectively, i.e. within hours. Minimum estimates of cooling rate prior to emplacement reported in Wright et al. (this issue-a) vary between $3*10^{-3}$ and $8.5*10^{-2}$ °C/min, based on the lack of welding textures.

Since the analyzed clasts comprised between 2 and 10 cm in diameter are completely remagnetized in the Cerro Galàn ignimbrite, we can argue that the minimum emplacement temperature required to remagnetize the clast at the cooling rates calculated by Wright et al. (this issue-a), varies between 621° and 635°C.

We can constrain the T dissipation path of the Cerro Galán eruption first assuming that the initial temperature was the magmatic temperature (T_m), which is inferred by Fe-Ti oxide geothermometry to be 790-810°C (c.f. Folkes et al.2010b). Adopting this estimated temperature as the T_m at the fragmentation level, the maximum temperature drop from

fragmentation to emplacement is ~200°C. Furthermore we can use the areal distribution of the partial welding in the CGI (Fig. 4.13) to define the distance at which the deposit temperature crossed the glass transition temperature (T_g) prior to emplacement. The welding ranks were determined on the basis of field occurrences, following the Quane and Russell (2005) classification. Thin section analysis carried out on 35 matrix cores did not allow a ranking attribution, since the extensive recrystallization obliterated the glassy shards structures in most of the samples. Most of the sites are rank II, while the maximum welding encountered is classified rank V, since some vesciculation could be still detected in some *fiamme*. Figure 4.13 shows how welding is unevenly distributed in the CGI, being more extensively present East of the caldera compared to the West, North and South. The maximum distance to which the welding degree of the deposit can be ranked higher than Rank II is 23 km, and this defines, given the compositional and loading characteristics, an emplacement temperature close to T_g. The maximum T_g calculated for an anhydrous rhyodacitic magma is ~780°C, decreasing to less than 550°C with 2% of dissolved H_2O, and decreasing also at increasing strain rates (Giordano et al. 2006).

Figure 6.1 summarizes the reconstructed thermal structure of the CGI and the implications of this thermal structure on the mechanism of transport and deposition of the CGI pyroclastic flows. Based on high temperature estimates throughout the ignimbrite, we derive that the CGI pyroclastic flow was very conservative in terms of temperature dissipation.

Cooling of the pyroclastic flow, containing a mixture of gas, lithics and juvenile fragments, is related to several processes which include: convective heat transport, radiative heat transfer, gas adiabatic expansion and heat conduction (e.g. Bardot 2000 and references therein).

Cooling by adiabatic decompression is usually relatively small and estimated to be about 90°C for the 1.8 ka Taupo ignimbrite, produced after the collapse of a plinian eruption column (McClelland et al. 2004 and references within). Air ingestion during an explosive eruption mainly occurs within the sustained column phase and, to a minor extent, during the collapsing phase, the area most subjected to air entrainment being the flow front (Cas and Wright 1987). In the CGI case, the absence of a basal fall-out deposit excludes the occurrence of an early plinian phase, and drives to boiling-over processes or low fountaining to produce pyroclastic flows (Cas et al., this issue). Both erupting conditions are favorable to poor heat loss above the vent region. Consequently, we take the estimate at Taupo as an absolute maximum for temperature loss accompanying decompression of the Cerro Galán eruptions.

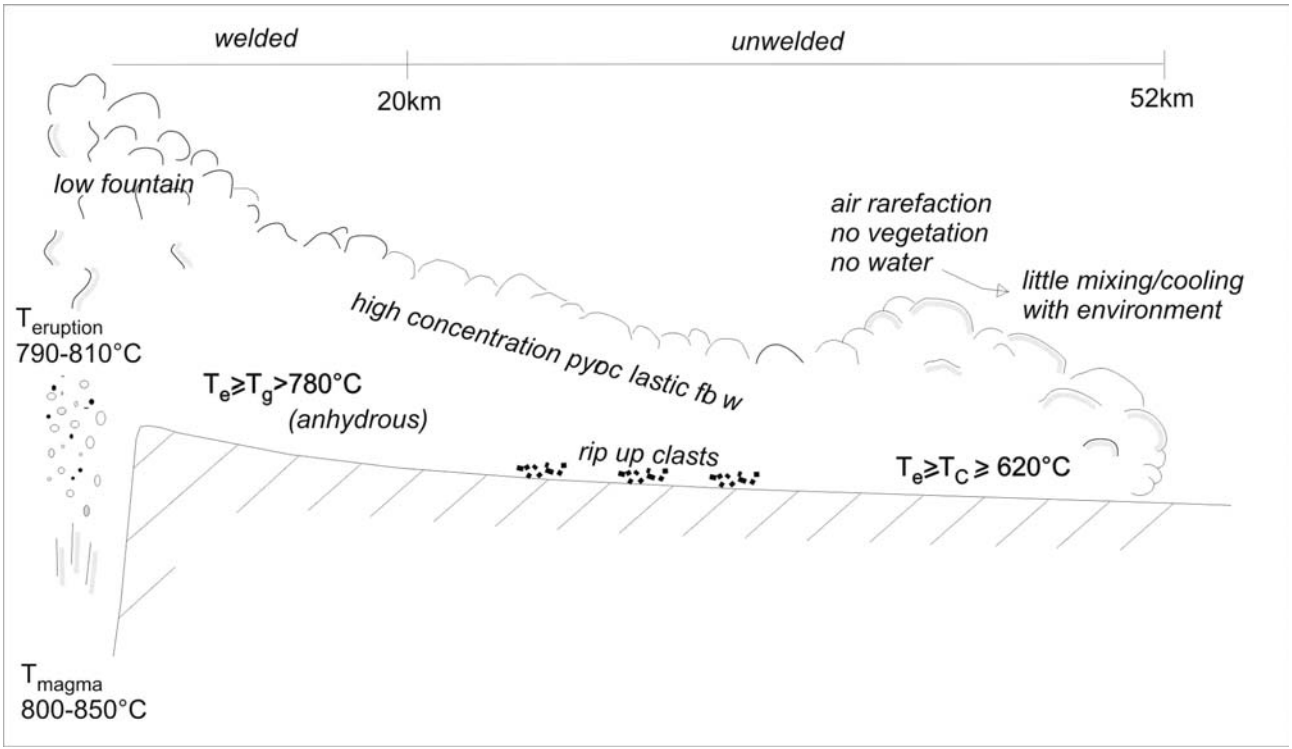

Fig. 6.1 - Schematic ignimbrite temperature profile from the vent to distal sites

Perhaps more significantly, the amount of convective, radiative, and conductive heat dissipation is largely function of the density of the flow. Convective and radiative heat loss can be considered as surface phenomena (Martì et al. 1991); therefore, the contribution of convective and radiative heat transfer increases as the dilution of the density current increases. In contrast, heat conduction is a more efficient heat transfer mechanism in dense flows and in presence of accidental clasts >1 cm in size (Bardot 2000).

The process of convective heat transfer in a pyroclastic flow depends on the temperature disequilibria between the pyroclasts, the lithics, and the gas (T_{gas}) (Bardot 2000). The T_{gas}

drives the cooling of the pyroclastic flow, being gases able to convectively admix with ambient air, cooling much quicker than pyroclasts. The T_{gas} decreases progressively from the conduit/vent into the uprising jet and down to the collapsing ground-hugging flow. T_{gas} further decreases with increased air entrainment (Todesco et al. 2006) or interaction with water and incorporation of vegetation and cold accidental lithic clasts (McClelland et al. 2004; Cioni et al. 2004).

The desert environment of the Puna Plateau, characterized by 5-10% humidity and 65mm/y of precipitation on annual average (Bianchi and Yañez 1992; Arias and Bianchi, 1996), excludes the possibility of significant incorporation of surface water or vegetation also in the past, further reducing the chances of an effective bulk mixing of the pyroclastic flow with the environment.

Additionally, McClelland et al. (2004) inferred at Taupo that the incorporation of 16% in weight of lithics at the source, with temperatures of 20°C and heat capacities similar to the juvenile material, would reduce the temperature of the pyroclastic flow from the magmatic temperature by 210°C. In the Cerro Galán ignimbrite, the lithic content is generally very low (<1-5%) and therefore cannot account for significant cooling.

The low degree of heat loss along the pyroclastic flow path is evaluated also in the context of the altitude of the area, ranging between ~3000 m and ~5000 m a.s.l. At these elevations the atmosphere is more rarefied and is likely to offer lower frictional resistance on the spreading pyroclastic flow, effectively lowering the extent of the mixing and air entrainment. Air density, without taking into account air moisture (almost negligible in the Puna Plateau), is about 0.6 kg/m^3 at 5000m a.s.l., i.e. a half of that at sea level.

The air entrainment plays therefore a major role in determining the emplacement temperature in distal facies. As widely recognised (e.g. Cas and Wright 1987), air entrainment occurs mostly in the eruption column, and subsequently at the head and in the body of the pyroclastic flow, where turbulent eddies may incorporate overlying air (Bursik and Woods 1996). In the Cerro Galàn ignimbrite, a low eruption column inhibited a noticeable heat exchange at that stage. Moreover, the absence of veneer facies on ridges indicates low level of dilution and low air entrainment in the body. Point counting on co-existing ash matrix glass and pumice glass (Folkes et al.2010a) showed that at distal localities of the ignimbrite outflow sheet, there is depletion in matrix ash of 17-34%. The authors adopt a conservative value of 30% in ash depletion to evaluate the volume of the elutriated material. On the other hand, the matrix crystal content (35-45%, Folkes et al.2010a) is comparable to the pumices crystal

content (35-49% in gray pumices, 44-57% in white pumices, Wright et al.2010b) indicating a very low degree in ash depletion, which in turns indicate low level of air ingestion.

In addition, again heat dissipation widely depends on bulk degree of fragmentation and overall grain size. The larger the proportion of fine-grained particles, the easier and faster the heat exchange with the fluid (gas/atmosphere) environment during flow (Cas and Wright 1987). The CGI ignimbrite is a fine-grained deposit (Wright et al.2010b). The fine-grained nature of the deposit would provide more favorable conditions for an efficient convective and radiative heat exchange with the environment. The low degree of cooling experienced by the CGI ($\leq$ 200°C as said above) cannot therefore be related to the grain size of the pyroclasts and must be interpreted instead as a result of the high particle concentration and the limited interaction with the external environment.

In summary, the constant high emplacement temperature of the flow, both along section and at increasing distance from the caldera, involving a maximum temperature drop from magmatic temperature of less than 200°C, is indicative of a very conservative flow. Temperature conservation can be attributed mainly to the high particle concentration in the flow, which met a very low interaction with the environment as testified also by the high fine particles content. Low fountaining, deduced by the absence of a basal fall deposit, inhibited the main factor of cooling, i.e. the air entrainment in the eruption column; the density of the flow itself further inhibited body air entrainment during the flow emplacement, as also supported by the lack of veneer facies. Lithics embedding did not act as a cooling factor, as lithic content is very low. Water and vegetation played no role, or a very small one if any, due to the peculiar local environmental condition.

The results of the analysis of the anisotropy of magnetic susceptibility, give interesting clues on the transport and deposition mechanism of this large volume ignimbrite.

The main results of the study came from the wide spreading of the sampled sites, covering a radial area of about 3000 km^2 around the caldera, giving the possibility of analyze the ignimbrite fabric in different paleotopographic settings.

The magnetic fabric of the Cerro Galàn ignimbrite is well defined as it is typical of fine-grained pyroclastic deposits (MacDonald and Palmer 1990; Gurioli et al. 2002). The organization of the magnetic fabric is inferred to reflect the deposition and transport mechanism of the pyroclastic flow, and, at different degrees, the influence of external factors like paleotopography or post-depositional processes.

The first output from the analysis of the flow directions, is that the ignimbrite is always directed outward with respect to caldera and that follows passively the paleotopography in

distal sites. This pattern appears clearly in the NE area where the flow, from a radial direction in the proximal sites, found a way in the ranges of the Calchaquì to east and then turn again to the north and to the south in Tacuil and Hualfin.

Another major output from the AMS analysis is the increase in magnetic anisotropy with distance the caldera, particularly in presence of paleotopography.

The enhancement of magnetic lineation with distance is reported in other density current; in the Bloodgood Canyon and Shelley Peak Tuffs, south western New Mexico, Seaman et al. (1991) state that the greater distance traveled by ash before deposition may enhance lineation development; in the volcanic debris avalanche of Cantal volcano in central France, Schneider and Fisher 1998) found that the magnetic fabric is better organized in distal deposits, where magnetic carriers are imbricated, respect to proximal deposits where AMS measurements indicate absence of a preferentially oriented matrix fabric.

In the Cerro Galàn ignimbrite an enhance of the magnetic fabric with distance is present, with the increment of magnetic lineation and foliation, but the higher increment is found in the anisotropy degree with a contemporaneous increase in lineation and decrease of the k_{min}. This increment is more evident in presence of paleovalleys, where the flow was forced to pass through a narrower path. This pattern can be related to an increase in shear stress provoked by an increase in velocity (Branney and Kokelaar 1992), due to the narrowing of the topographic flow boundary.

Subhorizontal fabric, where the k_{min} is oriented proximal to the vertical and k_{max} dispersed on the foliation may be related to compaction (Pioli et al. 2008) or to a depositional process that is dominated by particle settling in progressive aggradation (Schneider and Fisher 1998). In the Cerro Galàn ignimbrite subhorizontal fabric is common in the eastern and southern proximal sites. In these areas the welding rank is higher respect to distal and northern and western areas (Lesti et al. this issue), and the fabric can be therefore ascribed to the compaction acquired during welding.

This pattern indicates also that the welding occurred *in situ*, without post-emplacement flowing, i.e. the ignimbrite did not behave as a rheomorphic flow, as indicated also by the subhorizontal pattern of the *fiamme,* where present. On the other hand, subhorizontal fabric can also be interpret as due to imbrications respect to the paleotopography, which is steeper in proximal sites, and therefore to be related to a process that occurred before the secondary *in situ* welding.

Where welding is absent, subhorizontal fabric could be ascribed to progressive aggradation settling (e.g. Schneider and Fisher 1998). At Dique Trapiche, 30 km from the caldera rim, the

basal site 4 shows an imbricated fabric with well-grouped lineation, indicating a dense flow able to impress shear stresses in a non-rheomorphic flow. The upper site 5 shows a subhorizontal fabric, with the lineation dispersed on the foliation plane. Here the fabric cannot be ascribed to welding as it is absent, and the paleotopography is subhorizontal itself.

Changes in flow direction within a single section are proved to be a common feature, as the ignimbrite is capable of developing separated sheets meandering in the down current direction (MacDonald and Palmer 1990; Hughes and Druitt 1998; Porreca et al. 2008; LaBerge et al. 2008), recording temporal changes in flow boundary shear direction during the sustained passage of a current (Branney and Kokelaar 1992). In base and top sections of the CG ignimbrite, the magnetic fabric shows iso-oriented directions. The distinctive feature is that in the basal portion the lineation is strongly clustered, while in the top section the lineation is dispersed on the foliation plane. The direction of imbrication gives anyhow the same direction (e.g. sites 4 and 5). Upward decrease of the degree of anisotropy, lineation and foliation within ignimbrite flow units has already been described (Cagnoli and Tarling 1997; LaBerge et al. 2008; Paquereau-Lebti et al. 2008). Though the sampling sites along a single section are not enough to derive a detailed evolution of the flow, the concordant directions encountered at the base and top section in the Cerro Galàn ignimbrite, can be indicative of a steadiness of the overall flow direction. The presence of particle iso-orientation can be related to continuous sedimentation from a concentrated basal layer, which is also coherent with the massive fabric of the deposits.

In the aggradational model, the fabric of the deposit is considered to reflect the behaviour of the basal boundary layer irrespectively of the flow condition away from the basal layer (Branney and Kokelaar 2002). In the Cerro Galàn ignimbrite the low heat dissipation, revealed by the emplacement temperature distribution (Lesti et al. this issue), indicates that entire flow-depositional system is highly concentrated and very conservative. The role of the flow temperature in defining the mobility of the flow is still in debate. While in Montserrat, by direct measurements, Calder et al. (1999) found that the mobility of pyroclastic flows is independent from its temperature, the experiments on sand carried out by Mc Taggart (1960) show clearly that the higher the temperature of the sand, the higher is the *runout* distance. In any case, in the CGI the conservative character in terms of temperature up to distal sites can be interpreted as indicative of the homogeneity of the flow.

This is also confirmed by the facies characteristic of the deposit. The behavior of the flow in presence of paleotopography is *on-lap*, with clusters of ripup clasts that trail away horizontally into the ignimbrite body (Cas et al. this issue). The presence of trailing lithics

clusters at different heights along the same slope can be indicative of discrete pulses in the flow, that are empathized with the distance; discrete units separated by surges can be indeed identified at distal sites, e.g. at Tacuil, NE to the caldera, where six units were found. The ignimbrite shows the same behavior along the valley floor and at the ridge top and there are no evidences of veneer facies, both in the field and as deduced by the magnetic fabric. There are no evidences of vertical elutriation of fines after deposition, as pipes were not encountered in the field. This is again indicative of low gas content in the ignimbrite and of a high concentration of the flow.

Moreover, in the CGI there are no evidences of pyroclastic surges, but there are some similarities with secondary pyroclastic flows described by Calder et al. (1999) in Montserrat, showing high mobility yet being highly topographically constrained (in Montserrat also no surge deposits were found associated with the secondary flow deposit; Druitt et al. 2002). Secondary pyroclastic flows derive from segregation from pyroclastic surges, which produce mobile concentrated underflows with low frictional resistance, characterized also by fine-grained components (Calder et al. 1999), a common character of the CGI.

The formation of high concentration and high mobile flows can be ascribed to a high sedimentation rate, which can generate excess pore pressures, reducing the intergranular

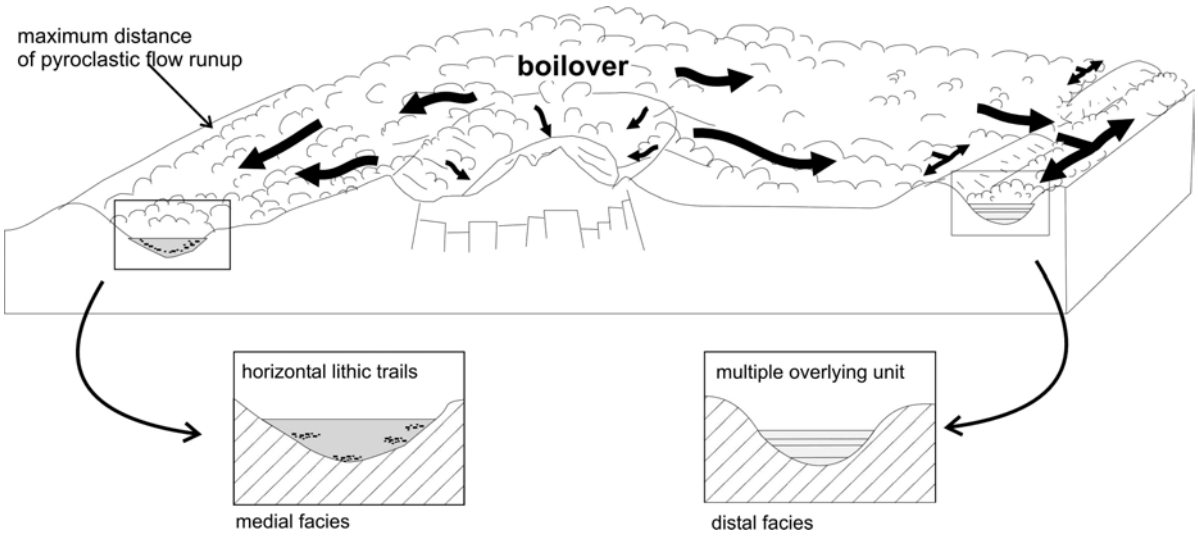

Fig. 6.2 - Schematic emplacement model of the Cerro Galàn ignimbrite. In distal sites the ignimbrite is topographically driven. Pulses in the eruption intensities leaded to multiple unit emplacement (right) or to horizontal lithic trails in massive facies (left)

friction (Druitt et al. 2002). In turns, high sedimentation rates are related to a high flow rates at the vent. Numerical simulation of pyroclastic flow dynamics in the Phlegrean Fields and at Vesuvius (Italy) Todesco et al. (2006; 2002) found that the eruption intensity is the main

parameter controlling the propagation of pyroclastic flows. The eruption intensity, associated with the fine-grained characteristic are supposed to be the driving factors of the high mobility of the Cerro Galàn ignimbrite.

In conclusion, the diffuse massive character, together with magnetic fabric imbrication and strong control of the paleotopography on the flow, are distinctive characters that allows to interpret the CG ignimbrite as produced by a 'boiling over' eruption followed by a deposition process dominated by a dense granular flow boundary zone, aggrading upward, from an equally highly concentrated and conservative flow (Fig 6.2).

7. Conclusions

In this study we estimated minimum emplacement temperatures and flow directions on the basis of paleomagnetic analysis and anisotropy of magnetic susceptibility made on lithic clasts and matrix of the ignimbrites of the Cerro Galán.

As for the lithic magnetic minerals characterization and emplacement temperatures the main results are:

1. The main magnetic carriers in accidental lithic clasts in the Cerro Galán ignimbrites are magnetite and to a minor extent hematite, maghemite and titano-magnetite. No significant mineralogical alteration occurred during laboratory heating procedures, confirming the reliability of the TRM analysis;
2. Two classes of paleomagnetic behaviour were identified by TRM analysis: clasts with a single component demagnetization vector (class A) and clasts with two demagnetization vector components (class B).
3. Unblocking temperatures T_{ub} were estimated for each clast and verified in the range 520°-620 °C; where T_{ub} ~580°C, the magnetization is carried by magnetite; when T_{ub} is ~620°C then it is carried by hematite.
4. The Cerro Galán ignimbrite was emplaced at temperatures equal or higher than 620°C throughout. Similar high temperatures characterized the units of the Toconquis Group, being the emplacement temperature set at 580-610°C for the Lower Merihuaca ignimbrite, and equal or higher than 620°C for the other ignimbrites of the Group.

The study of the anisotropy of magnetic susceptibility carried out on the matrix of the Cerro Galán ignimbrite, leaded to the following main results:

1. The main magnetic carrier in the matrix in the Cerro Galán ignimbrite is the paramagnetic fraction represented mainly by biotite grains. The ferromagnetic fraction contributes to 30% of the magnetic signal, and is due to titano-magnetite, magnetite, ilmenite and minor hematite. Ferromagnetic mineral are either dispersed as spherules in the matrix or mimic the paramagnetic shapes. The paramagnetic and ferromagnetic ellipsoids are concordant showing subvertical and clustered k_{min} direction and lineation either clustered or dispersed on the foliation. The paramagnetic and ferromagnetic ellipsoids are coincident also with the low field AMS ellipsoids.
2. The AMS ellipsoids vary from triaxial-oblate to oblate. The magnetic foliation is always well defined and the lineation is either clustered or dispersed along the foliation plane. The low field AMS ellipsoids are coincident with the paramagnetic and ferromagnetic (high field) ellipsoids.
3. The comparison between the magnetic fabric and the mineralogical fabric, carried out by image analysis on thin sections, revealed a good correspondence, allowing relating the AMS signal to the sedimentological texture of the matrix and therefore using the AMS as flow direction indicator.
4. The magnetic anisotropy degree is the parameter that mostly contributes to the variability between sites. The highest anisotropy are encountered where the paleotopography forces the flow through paleovalleys.
5. The directions of the flow are radial in all directions around the caldera up to 45 km in absence of topographic obstacles, while are deviated beyond 35 km in presence of paleovalleys.
6. The pyroclastic flow that emplaced the Cerro Galàn ignimbrite, was characterized by a strong uniformity throughout the flow path, was highly concentrated and topographically driven in distal sites, but the high mobility of the flow allowed the emplacement at distances up to almost 80 km from the topographic caldera rim.

The very large volume Cerro Galàn ignimbrite is a very conservative ignimbrite. A maximum temperature drop of 200°C can be accounted from fragmentation to the emplacement. Such conditions can be explained by a combination of effects, in part related to the low accessory/accidental lithic content, in part to low fountaining at vent(s) and in part to

the high particle concentration of the pyroclastic flow(s), with little air, water and vegetation entrainment along flow favored by the particular high altitude, desert conditions of the Puna Plateau. Such conditions suggest low bulk turbulence level, highlighted also by the absence of veneer facies, of the pyroclastic flow(s), in agreement with the AMS results and field evidence of the strong topographic control on the Cerro Galàn Ignimbrite.

8. References

AGICOInc. (2001) SUSAR

Aramaki S, Akimoto S (1957) Temperature estimation of pyroclastic deposits by natural remanent magnetism. Am. J. Sci. 255:619-627

Aubourg C, Giordano G, Mattei M, Speranza F (2002) Magma flow in sub-aqueous rhyolitic dikes inferred from magnetic fabric analysis (Ponza Island, W. Italy). Physics and Chemistry of the Earth, Parts A/B/C 27:1263-1272

Arias M, Bianchi AR (1996) Estadisticas Climatologicas de la provincia de Salta. INTA, Salta

Baer EM, Fisher RV, Fuller M, Valentine G (1997) Turbulent transport and deposition of the Ito pyroclastic flow: determinations using anisotropy of magnetic susceptibility. Journal of Geophysical Research 102:22565-86

Banks NG, Hoblitt RP (1981) Summary of temperature studies of 1980 deposits. In: Lipman PW and Mullineaux DR (eds) The 1980 Eruptions of Mount St. Helens, Washington, USGS Professional Paper, pp 844

Bardot L (2000) Emplacement temperature determinations of proximal pyroclastic deposits on Santorini, Greece, and their implications. Bulletin of Volcanology 61:450-467

Bardot L, McClelland E (2000) The reliability of emplacement temperature estimates using palaeomagnetic methods: a case study from Santorini, Greece. Geophysical Journal International 143:39-51

Bianchi R, Yañez CE (1992). Las precipitaciones en el Noroeste Argentino. INTA-Estación Experimental Agropecuaria Salta. II Edicion.

Branney MJ, Kokelaar P (1992) A reappraisal of ignimbrite emplacement: progressive aggradation and changes from particulate to non-particulate flow during emplacement of high-grade ignimbrite. Bulletin of Volcanology 54:504-520

Branney MJ, Kokelaar P (2002) Pyroclastic density currents and the sedimentation of ignimbrites Geological Society Memoir. 27, pp 1-138

Bursik MI, Woods AW (1996) The dynamics and thermodynamics of large ash flows. Bull. Volc. 58:175-193

Cagnoli B, Tarling DH (1997) The reliability of anisotropy of magnetic susceptibility (AMS) data as flow direction indicators in friable base surge and ignimbrite deposits: Italian examples. Journal of Volcanology and Geothermal Research 75:309-320

Calder ES, Cole PD, Dade WB, Druitt TH, Hoblitt RP, Huppert HE, Ritchie LJ, Sparks RSJ, Young SR (1999) Mobility of pyroclastic flows and surges at the Soufrière Hills Volcano, Montserrat. Geophysical Research Letters 26:537-540

Cañón-Tapia E, Castro J (2004) AMS measurements on obsidian from the Inyo Domes, CA: a comparison of magnetic and mineral preferred orientation fabrics. Journal of Volcanology and Geothermal Research 134:169-182

Carslaw HS, Jaeger JC (1959) Conduction of heat in solids. Oxford University Press, Oxford, pp 1-510

Cas R, Wright H, Lesti C, Porreca M, Folkes C, Giordano G, Viramonte JG (2010) Understanding the Flow Dynamics of Extremely Large Volume Pyroclastic Flows

Based on Interaction with Basement Topography: the 2.5 Ma Cerro Galan Ignimbrite, northwestern Argentina. submitted Bulletin of Volcanology
Cas RAF, Wright JV (1987) Volcanic Successions. Modern and Ancient. Unwin Hyman, London, pp 1-528
Cioni R, Gurioli L, Lanza R, Zanella E (2004) Temperature of the A.D. 79 pyroclastic density current deposits (Vesuvius, Italy). J Geophys Res 109:B02207 doi:10.1029/2002JB002251
Chadima M, Hrouda F (2006) Remasoft 3.0 a user-friendly paleomagnetic data browser and analyzer. Travaux Géophysiques XXVII:20-21
Chadima M, Jelinek V (2009) Anisoft 4.2 Anisotropy data browser
Cioni R, Marianelli P, Sbrana A (1992) Dynamics of the AD 79 eruption: stratigraphic, sedimentologic and geochemical data on the successions of the Somma-Vesuvius southern and eastern sectors. Acta Vulcanologica 2:109 -124
Cioni R, Gurioli L, Lanza R, Zanella E (2004) Temperatures of the A.D. 79 pyroclastic density current deposits (Vesuvius, Italy). Journal of Geophysical Research 109:B02207, doi:10.1029/2002JB002251
Coira B, Kay SM, J. V (1993) Upper Cenozoic magmatic evolution of the Argentine Puna- A model for changing suabduction geometry. International Geology Review 35:677-720
de Silva SL (1989) Altiplano-Puna volcanic complex of the central Andes. Geology 17:1102-1106
DeRita D, Giordano G, Milli S (1998) Forestepping-backstepping staking pattern of volcaniclastic successions: Roccamonfina volcano, Italy. Journal of Volcanology and Geothermal Research 80:155-178
Druitt TH (1998) Pyroclastic density currents. In: Gilbert JS and Sparks RSJ (eds) The Physics of Explosive Volcanic Eruptions, The Geological Society Special Publication 145, London, pp 145-182
Druitt TH, Calder ES, Cole PD, Hoblitt RP, Loughlin SC, Norton GE, Ritchie LJ, Sparks RSJ, Voight B (2002) Small-volume, highly mobile pyroclastic flows formed by rapid sedimentation from pyroclastic surges at Soufriere Hills Volcano, Montserrat: an important volcanic hazard. Geological Society, London, Memoirs 21: 263-279
Dunlop DJ, Özdemir Ö (1997) Rock Magnetism: Fundamentals and Frontiers. Cambridge University Press, Cambridge, pp 1-573
Ellwood BB (1982) Estimates of flow direction for calc-alkaline welded tuffs and paleomagnetic data reliability from anisotropy of magnetic susceptibility measurements: Central San Juan Mountains, southwest Colorado. Earth and Planetary Science Letters 59:303-314
Fisher RA (1953) Dispersion on a sphere. Proceedings of the Royal Society London 217A:295-305
Fisher RV, Heiken G (1982) Mt. Pelée, Martinique: May 8 and 20, 1902, pyroclastic flows and surges. Journal of Volcanology and Geothermal Research 13:339-371
Fisher RV, Orsi G, Ort M, Heiken G (1993) Mobility of a large volume pyroclastic flow-emplacement of the Campanian ignimbrite, Italy. Journal of Volcanology and Geothermal Research 56:205-220
Folkes C, Wright H, Cas RAF, de Silva SL, Lesti C, Viramonte JG (2010a) A re-appraisal of the stratigraphy and volcanology in the Cerro Galán volcanic system, NW Argentina. submitted Bulletin of Volcanology
Folkes CB, de Silva S, Wright HM, Cas RAF (2010b) Geochemical homogeneity of a long-lived, large silicic system; evidence from the Cerro Galán caldera, NW Argentina. submitted Bulletin of Volcanology
Francis PW, O'Callaghan L, Kretzschmar GA, Thorpe RS, Sparks RSJ, Page RN, de Barrio RE, Gillou G, Gonzalez OE (1983) The Cerro Galan ignimbrite. 301:51-53

Freundt A, Bursik M (2001) From Magma to Tephra Modelling Physical Processes of Explosive Volcanic Eruptions. Elsevier, Amsterdam, pp 1-318

Froggatt PC, Wilson CJN, Walker GPL (1981) Orientation of logs in the Taupo ignimbrite as an indicator of flow direction and vent position. Geology 9:109-111

Giordano D, Mangiacapra A, Potuzák M, Russell JK, Romano C, Dingwell DB, Di Muro A (2006) An expanded non-Arrhenian model for silicate melt viscosity: A treatment for metaluminous, peraluminous and peralkaline liquids. Chem. Geol. 229, 42-56

Giordano G, Dobran F (1994) Computer simulations of the Tuscolano Artemisio's second pyroclastic flow unit (Alban Hills, Latium, Italy). Journal of Volcanology and Geothermal Research 61:69-94

Giordano G (1998) Facies characteristics and magma-water interaction of the White Trachytic Tuffs (Roccamonfina Volcano, southern Italy). Bulletin of Volcanology 60:10-26

Giordano G, De Benedetti AA, Diana A, Diano G, Gaudioso F, Marasco F, Miceli M, Mollo S, Cas RAF, Funiciello R (2006) The Colli Albani mafic caldera (Roma, Italy): Stratigraphy, structure and petrology. Journal of Volcanology and Geothermal Research 155:49-80

Giordano G, Porreca M, Musacchio P, Mattei M (2008) The Holocene Secche di Lazzaro phreatomagmatic succession (Stromboli, Italy): evidence of lateral blast deduced by facies analysis and AMS flow directions. Bulletin of Volcanology doi: 10.1007/s00445-008-0198-x:

Gonzalez OE (1984) La ignimbritas de "Ojo de Ratones" y sus relaciones regionales, provincia de Salta. Noveno Congreso Geologico Argentino, Actas I: 206-220

Gradstein FM, Ogg JG, Smith AG (2004) A Geologic Time Scale 2004. Cambridge University Press, Cambridge, pp 1-610

Grégoire V, Darrozes J, Gaillot P, Nédélec A, Launeau P (1998) Magnetite grain shape fabric and distribution anisotropy vs rock magnetic fabric: a three-dimensional case study. Journal of Structural Geology 20:937-944

Gurioli L, Cioni R, Sbrana A, Zanella E (2002) Transport and deposition from pyroclastic flows over densely inhabited areas: Herculaneum (Italy). Sedimentology 46:1-26

Gurioli L, Pareschi MT, Zanella E, Lanza R, Deluca E, Bisson M (2005) Interaction of pyroclastic density currents with human settlements: Evidence from ancient Pompeii. Geology 33:441–444

Gurioli L, Zanella E, Pareschi MT, Lanza R (2007) Influences of urban fabric on pyroclastic density currents at Pompeii (Italy): 1. Flow direction and deposition. Journal of Geophysical Research 112, B05213, doi:10.1029/2006JB004444:

Herrero-Bervera E, Cañon-Tapia E, Walker GPL, Tanaka H (2002) Magnetic fabrics study and inferred flow directions of lavas of the Old Pali Road, O'ahu, Hawaii. Journal of Volcanology and Geothermal Research 118:161-171

Hillhouse JW, Wells RE (1991) Magnetic fabric, flow directions, and source area of the lower Miocene Peach Springs Tuff in Arizona, California, and Nevada. Journal of Geophysical Research 96:12,443-12,460

Hoblitt RP, Kellogg KS (1979) Emplacement temperatures of unsorted and unstratified deposits of volcanic rock debris as determined by paleomagnetic techniques. Geological Society of America Bulletin 90:633-642.

Hughes SR, Druitt TH (1998) Particle fabric in a small, type-2 ignimbrite fow unit (Laacher See, Germany) and implications for emplacement dynamics. Bulletin of Volcanology 60:125-136

Incoronato A, Addison FT, Tarling DH, Nardi G, Pescatore T (1983) Magnetic fabric investigations of pyroclastic deposits from Phlegrean Fields, southern Italy. Nature 306:461-463

Jelinek V (1978) Statistical processing of anisotropy of magnetic susceptibility measures on groups of specimens. Studia geophisica et geodetica 22:50-62
Kamata H, Mimura K (1983) Flow directions inferred from imbrication in the Handa pyroclastic flow deposit in Japan. Bulletin of Volcanology 46:277-282
Kay S, Coira B, Mpodozis C (2008) Field trip guide: Neogene evolution of the central Andean Puna plateau and southern Central Volcanic Zone. Geological Society of America fl d013:119-181
Kent DV, Ninkovich D, Pescatore T, Sparks SRJ (1981) Palaeomagnetic determination of emplacement temperature of Vesuvius AD 79 pyroclastic deposits. Nature 290:393-396
Knight MD, Walker GPL, Ellwood BB, Diehl JF (1986) Stratigraphy, paleomagnetism, and magnetic fabric of the Toba Tuffs: constraints on the sources and eruptive styles. Journal of Geophysical Research 91:10,355-10,382
LaBerge R, Porreca M, Mattei M, Giordano G, Cas R (2008) Meandering flow of a pyroclastic density current documented by the anisotropy of magnetic susceptibility (AMS) in the quartz latite ignimbrite of the Pleistocene Monte Cimino volcanic centre (central Italy). Tectonophysics doi: 10.1016/j.tecto.2008.09.009.
Lacroix A (1904) La Montagne Pelée et ses éruptions. Paris, Masson et Cie 662
Launeau P, Robin P-YF (1996) Fabric analysis using the intercept method. Tectonophysics 267:91-119
Le Pennec J-L, Chen Y, Diot H, Froger J-L, Gourgaud A (1998) Interpretation of anisotropy of magnetic susceptibility fabric of ignimbrites in terms of kinematic and sedimentological mechanisms: An Anatolian case-study. Earth and Planetary Science Letters 157:105-127
Lipman PW, Mullineaux DR (1981) The 1980 Eruptions of Mount St. Helens, Washington. U.S. Government Printing Office, Washington, DC, pp 1-844
Lipman PW (1997) Subsidence of ash-flow calderas; relation to caldera size and magma-chamber geometry. Bulletin of Volcanology 59:198-218
Lowrie W (1990) Identification of ferromagnetic minerals in a rock by coercivity and unblocking temperature properties. Geophysical Research Letters 17:159–162
MacDonald WD, Palmer HC (1990) Flow directions in ash-flow tuffs: a comparison of geological and magnetic susceptibility measurements, Tshirege member (upper Bandelier Tuff) Valles caldera, New Mexico, USA. Bulletin of Volcanology 53:45-59
MacDonald WD, Palmer HC, Hayatsu A (1998) Structural rotation and volcanic source implications of magnetic data from Eocene volcanic rocks, SW Idaho. Earth and Planetary Science Letters 156:225-37
Mandeville CW, S. C, Sigurdsson H, King J (1994) Paleomagnetic evidence for high-temperature emplacement of the 1883 subaqueous pyroclastic flows from Krakatau Volcano, Indonesia. Journal of Geophysical Research B: Solid Earth 99:9487–9504
Martin-Hernandez F, Hirt AM (2001) Separation of ferrimagnetic and paramagnetic anisotropies using a high-field torsion magnetometer. Tectonophysics 337:209-221
Mason BG, Pyle DM, Oppenheimer C (2004) The size and frequency of the largest eruption on Earth. Bulletin of Volcanology 66:735-748
McClelland E, Druitt TH (1989) Paleomagnetic estimates of emplacement temperatures of pyroclastic deposits on Santorini, Greece. Bulletin of Volcanology 51:16-27
McClelland E, Wilson CJN, Bardot L (2004) Paleotemperature determinations for the 1.8 ka Taupo ignimbrite, New Zealand, and implications for the emplacement history of a high velocity pyroclastic flow. Bulletin of Volcanology 66:492-513
McClelland-Brown E (1982) Discrimination of TRM and CRM by blocking-temperature spectrum analysis. Physics of The Earth and Planetary Interiors 30:405-414

Miller TP, Smith RL (1977) Spectacular mobility of ash flows around Aniakchak and Fisher calderas, Alaska. Geology 5:173-176

Newhall CG, Self S (1982) The volcanic explosivity index (VEI): An estimate of explosive magnitude for historical volcanism. Journal of Geophysical Research 87:1231–1238

Ort MH (1993) Eruptive processes and caldera formation in a nested downsagcollapse caldera: Cerro Panizos, central Andes Mountains. Journal of Volcanology and Geothermal Research 56:221-252

Ort MH, Rosi M, Anderson CD (1999) Correlation of deposits and vent locations of the proximal Campanian Ignimbrite deposits, Campi Flegrei, Itali, based on natural remanent magnetization and anisotropy of magnetic susceptibility characteristics. Journal of Volcanology and Geothermal Research 91:167-178

Palmer HC, MacDonald WD (1999) Anisotropy of magnetic susceptibility in relation to source vents of ignimbrites: empirical observations. Tectonophysics 307:207-218

Paquereau-Lebti P, Fornari M, Roperch P, Thouret J-C, Macedo O (2008) Paleomagnetism, magnetic fabric, and 40Ar/39Ar dating of Pliocene and Quaternary ignimbrites in the Arequipa area, southern Peru. Bulletin of Volcanology 70:977-997

Paterson GA, Roberts AP, Mac Niocaill C, Muxworthy AR, Gurioli L, Viramonte JG, Navarro C (2010) Paleomagnetic determination of emplacement temperatures of pyroclastic deposits: an underutilised tool. Bull Volcanol doi: 10.1007/s00445-009-0324-4

Pioli L, Lanza R, Ort M, Rosi M (2008) Magnetic fabric, welding texture and strain fabric in the Nuraxi Tuff, Sardinia, Italy. Bulletin of Volcanology 10.1007/s00445-008-0194-1:

Plenier G, Camps P, Henry B, Ildefonse B (2005) Determination of flow directions by combining AMS and thin-section analyses: implications for Oligocene volcanism in the Kerguelen Archipelago (southern Indian Ocean). Geophysical Journal International 160:63-78

Porreca M, Mattei M, Giordano G, De Rita D, Funiciello R (2003) Magnetic fabric and implications for pyroclastic flow and lahar emplacement, Albano maar, Italy. Journal of Geophysical Research Solid Earth 108:2264 doi:10.1029/2002JB002102

Porreca M, Giordano G, Mattei M, Musacchio P (2006) Evidence of two Holocene phreatomagmatic eruptions at Stromboli volcano (Aeolian Islands) from paleomagnetic data. Geophysical Research Letters 33,:L21316, doi:10.1029/2006GL027575

Porreca M, Mattei M, MacNiocaill C, Giordano G, McClelland E, Funiciello R (2008) Paleomagnetic evidence for low-temperature emplacement of the phreatomagmatic Peperino Albano ignimbrite (Colli Albani volcano, Central Italy). Bulletin of Volcanology doi:10.1007/s00445-007-0176-8:

Pullaiah G, Irving E, Buchan KL, Dunlop DJ (1975) Magnetization changes caused by burial and uplift. Earth and Planetary Science Letters 28:133–143

Quane SL, Russell JK (2005) Ranking welding intensity in pyroclastic deposits. Bulletin of Volcanology 67:129-143

Rapalini AE, de Luchi ML (2000) Paleomagnetism and magnetic fabric of Middle Jurassic dykes from Western Patagonia, Argentina. Physics of the Earth and Planetary Interiors 120:11-27

Raposo MIB (1997) Magnetic fabric and its significance in the Florianopolis dyke swarm, southern Brazil. Geophysical Journal International 131:159-70

Riller U, Petrinovic I, Ramelow J, Strecker M, Oncken O, (2001) Late Cenozoic tectonism, collapse caldera and plateau formation in the central Andes. Earth Planet Sci Lett 188:299-311

Rochette P, Jackson MJ, Aubourg C (1992) Rock magnetism and the interpretation of anisotropy of magnetic susceptibility. Reviews of Geophysics 30:209–226

Rose WI, Chesner CA (1987) Dispersal of ash in the great Toba eruption, 75 ka. Geology 15:913–917

Salfity JA, Gorustovih S, Moya M, Amengual R (1984) Marco tectónico de la sedimentación y efusividad cenozoicas de la Puna Argentina. In: IX Congreso Geológico Argentino, Actas I, pp 5–515.

Schmincke H-U, Swanson DA (1967) Laminar viscous flowage structures in ash-flow tuffs from Gran Canaria, Canary Islands. The Journal of Geology 75:641-664

Schneider J-L, Fisher RV (1998) Transport and emplacement mechanisms of large volcanic debris avalanches: evidence from the northwest sector of Cantal Volcano (France). Journal of Volcanology and Geothermal Research 83:141-165

Scott AC, Sparks RSJ, Bull ID, Knicker H, Evershed RP (2008) Temperature proxy data and their significance for the understanding of pyroclastic density currents. Geology 143-146

Seaman SJ, McIntosh WC, Geissman JW, Williams ML, Elston WE (1991) Magnetic fabrics of the Bloodgood Canyon and Shelley Peak Tuffs, southwestern New Mexico: implications for emplacement and alteration processes. Bulletin of Volcanology 53:460-476

Sigurdsson H, Carey S, Cornell W, Pescatore T (1985) The eruption of Vesuvius in AD 79. National Geographic Research 3:332-387

Simkin T, Fiske RS (1983) Krakatau 1883 - the volcanic eruption and its effects. 464

Sparks RSJ, Francis PW, Hamer RD, Pankhurst RJ, O'Callahaghan LO, Thorpe RS, Page R (1985) Ignimbrites of the Cerro Galan caldera, NW Argentina. Journal of Volcanology and Geothermal Research 24:205–248

Suzuki K, Ui T (1982) Grain orientation and depositional ramps as flow direction indicators of a large-scale pyroclastic flow deposit in Japan. Geology 10:429-432

Todesco M, Neri A, Esposti Ongaro T, Papale P, Macedonio G, Santacroce R, Longo A, (2002) Pyroclastic flow hazard at Vesuvius from numerical modelling. I. Large scale dynamics. Bull. Volcanol., 64, 155-177

Todesco M, Neri A, Esposti Ongaro T, Papale P, Rosi M (2006) Pyroclastic flow dynamics and hazard in a caldera setting: Application to Phlegrean Fields (Italy). Geochem Geophys Geosys 7:11. doi:10.1029/2006GC001314

Viramonte JG, Galliski MA, Araña Saavedra V, Aparicio A, García Cacho L, Martín Escorza C (1984) El finivulcanismo básico de la Depresión de Arizaro, provincia de Salta, República Argentina. IX Congreso Geológico Argentino, Actas III:234-254

Wayne R (2008) ImageJ - image processing and analysis in java

Weaver R, Roberts AP, Barker AJ (2002) A late diagenetic (syn-folding) magnetization carried by pyrrhotite: implications for paleomagnetic studies from magnetic iron sulphide-bearing sediments. Earth and Planetary Science Letters 200:371-86

Wright HMN, Cas RAF, Folkes CB, Lesti C, Porreca M, Giordano G (2010a) Columnar jointing in vapor phase altered, non-welded Cerro Galan ignimbrite, Paycuqui, Argentina. submitted Bull Volcanol

Wright HMN, Folkes CB, Cas RAF, Cashman K (2010b) Heterogeneous pumice populations in the 2.56 Ma Cerro Galán ignimbrite: implications for magma recharge and ascent preceding a large volume silicic eruption. submitted Bull Volcanol

Wright JV (1978) Remanent magnetism of poorly sorted deposits from the Minoan eruption of Santorini. Bull. Volcanol. 41:1-5

Wright JV (1980) Stratigraphy and geology of the welded air-fall tuffs of Pantelleria, Italy. Geologische Rundschau 69:263-291

Zanella E, Gurioli L, Pareschi MT, Lanza R (2007) Influences of urban fabric on pyroclastic density currents at Pompeii (Italy): Temperature of the deposits and hazard implications. J. Geophys. Res. 112, B05214:doi:10.1029/2006JB004775.

Zijderveld JDA (1967) A. C. demagnetization of rocks: analysis of results. In: Collinson DW, Creer KM and Runcorn SK (eds) Methods in Palaeomagnetism, Elsevier, Amsterdam, New York, pp 254–286

Zlotnicki J, Pozzi JP, Boudon G, Moreau MG (1984) A new method for the determination of the setting temperature of pyroclastic deposits (example Guadeloupe: French West Indies). . Journal of Volcanology and Geothermal Research 21:297-312

unit	Site (ID)	lat	long	Locality	Facies	h asl (m)	distance (km)	N	Nr	class		T_{ub} (°C)	T_e
										A	B		
Vega	0264	679052	7125434	Vega Real Grande	proximal	4470	12	5	5	5		>580	
Real Grande	0192	682369	7122876	SE Rio las Pitas	proximal	4710	9	2	2	2		>580	
	0263	679052	7125434	Vega Real Grande	proximal	4423	9	3	3	3		>600	
	0262	679052	7125434	Vega Real Grande	proximal	4383	9	6	6	6		>600	
	0261	679052	7125434	Vega Real Grande	proximal	4363	12	3	3	3		>580	
	0305	676765	7126380	NW Rio las Pitas	proximal	4323	15	1	1	1		>580	
	0303	676765	7126380	NW Rio las Pitas	proximal	4341	15	1	1	1		>580	
	0302	676765	7126380	NW Rio las Pitas	proximal	4357	15	2	2	2		>580	
	0171	676290	7125803	NW Rio las Pitas	proximal	4229	15	2	2	2		>580	
	0620	717467	7201067	The Ratone's Saddle	distal	4050	55	6	6	6		>600	
Pitas	0251	679052	7125434	Vega Real Grande	proximal	4343	12	4	4	4		>620	
	0215	678932	7124869	Vega Real Grande	proximal	4333	12	6	6	6		>600	
	0770	679034	7124976	Vega Real Grande	proximal	4320	12	8	8	8		>610	
	0241	678842	7125054	Vega Real Grande	proximal	4284	12	6	6	6		>620	
	0780	678842	7125054	Vega Real Grande	proximal	4280	12	1	1		1		610-630
Upper merihuaca	0750	679034	7124976	Vega Real Grande	proximal	4305	12	8	7	6	1	>610	530-560
	0231	678842	7125054	Vega Real Grande	proximal	4303	12	4	3	3		>620	
	0214	678932	7124869	Vega Real Grande	proximal	4295	12	4	3	3		>580	
	0222	678661	7125002	Vega Real Grande	proximal	4290	12	4	3	3		>640	
Middle Merihuaca	0221	678661	7125002	Vega Real Grande	proximal	4286	12	3	3	3		>600	
	0740	679034	7124976	Vega Real Grande	proximal	4275	12	10	10	10		>610	
	0161	678822	7124946	Vega Real Grande	proximal	4260	12	5	5	5		>580	
	0162	678822	7124946	Vega Real Grande	proximal	4255	12	2	2	2		>580	
	0213	678932	7124869	Vega Real Grande	proximal	4245	12	6	5	4	1	>600	360-480
Lower Merihuaca	0212	678932	7124869	Vega Real Grande	proximal	4230	12	6	6	4	2	>630	580-600
	0730	678932	7124869	Vega Real Grande	proximal	4230	12	10	10	4	6	>610	590-610
Blanco	0211	678932	7124869	Vega Real Grande	proximal	4226	12	7	7	7		>580	

Table 4.1 - Toconquis Group site TRM results. Sampled sites are ordered from the lowest to the highest in the stratigraphic section, for each Toconquis unit. Included are: site (ID), coordinates, locality name, distal/proximal facies, height a.s.l., distance from the present caldera margins (measured at the intersection with the site-caldera centre connecting line), number of analyzed samples, number of reliable samples, number of samples classified as class A or class B, unblocking temperatures, and temperature interval between LT component and HT component in class B samples. In the case of more than one B sample at the same site, the reported values are the lowest and higher measured temperatures

Site (ID)	lat	long	Locality	Facies	h asl (m)	distance (km)	N	Nr	class		T_{ub} (°C)
									A	B	
0012	715162	7198326	Hombre Muerto	distal	4025	52	2	2	2	/	>610
0013	715162	7198326	Hombre Muerto	distal	4043	52	3	3	3	/	>580
0021	714430	7159589	Rio de los Patos	proximal	4250	14	1	1	1	/	>520
0031	713403	7160446	Aguas Calientes	proximal	4112	10	5	5	5	/	>520
0032	713403	7160446	Aguas Calientes	proximal	4135	10	4	4	4	/	>580
0033	713403	7160446	Aguas Calientes	proximal	4151	10	6	6	6	/	>600
0034	713403	7160446	Aguas Calientes	proximal	4172	10	3	3	3	/	>520
0035	713403	7160446	Aguas Calientes	proximal	4190	10	3	2	2	/	>580
0041	691417	7172849	Dique Trapiche	medial	4122	28	1	1	1	/	>580
0042	691417	7172849	Dique Trapiche	medial	4141	28	1	1	1	/	>520
0051	692242	7167984	Stonhenge	medial	4434	24	3	3	3	/	>580
0201	663963	7132027	Paicuqui	medial	3619	27	9	5	5	/	>600
0202	663963	7132027	Paicuqui	medial	3629	27	5	5	5	/	>580
0203	663963	7132027	Paicuqui	medial	3632	27	8	8	8	/	>580
0204	663963	7132027	Paicuqui	medial	3640	27	3	3	3	/	>580
0205	663963	7132027	Paicuqui	medial	3619	27	3	2	2	/	>580
0271	657459	7118286	NW Antofagasta	distal	3463	34	4	4	4	/	>580
0272	657459	7118286	NW Antofagasta	distal	3400	34	4	4	4	/	>600
0281	664646	7132471	Paicuqui	medial	3650	27	7	7	7	/	>620
0282	664646	7132471	Paicuqui	medial	3606	27	6	5	5	/	>580
0283	664646	7132471	Paicuqui	medial	3645	27	6	1	1	/	>580
0284	664646	7132471	Paicuqui	medial	3630	27	3	3	3	/	>580
0285	664646	7132471	Paicuqui	medial	3645	27	5	3	3	/	>600
0342	663447	7143733	Los Nacimientos	distal	3879	30	6	2	2	/	>600
0343	663447	7143733	Los Nacimientos	distal	3879	30	5	4	4	/	>580

Table 4.2 - Cerro Galán site TRM results. Fields are the same as in Tab 2

Site (ID)	lat	long	Locality	Facies	h asl (m)	distance (km)	N	Nr	class		Tub (°C)
									A	B	
0344	663447	7143733	Los Nacimientos	distal	3879	30	4	4	4	/	>580
0351	675484	7150230	Puntas Gordas	distal	4295	22	5	5	5	/	>610
0352	675484	7150230	Puntas Gordas	distal	4295	22	6	6	6	/	>610
0353	675484	7150230	Puntas Gordas	distal	4300	22	3	3	3	/	>610
0371	659131	7116841	Antofagasta	distal	3445	33	4	4	4	/	>580
0372	659132	7116842	Antofagasta	distal	3450	33	2	2	2	/	>610
0373	659133	7116843	Antofagasta	distal	3458	33	5	4	4	/	>580
0374	659134	7116844	Antofagasta	distal	3465	33	5	2	2	/	>630
0381	674833	7091114	Rio el Jote	distal	3504	31	4	4	4	/	>600
0382	674833	7091114	Rio el Jote	distal	3520	31	4	3	3	/	>550
0420	753733	7169457	Tacuil	distal	2718	44	4	3	3	/	>630
0430	753733	7169457	Tacuil	distal	2718	44	6	5	5	/	>600
0440	753733	7169457	Tacuil	distal	2718	44	8	8	8	/	>600
0460	757643	7155690	Hualfin	distal	2930	43	3	3	3	/	>630
0660	676278	7158826	Beltran Runup	distal	4410	27	7	7	7	/	>600

Table 4.2 (continued)

site	dist	N	Km (Km sd)	L (L sd)	F (F sd)	P (P sd)	T (T sd)	K_{max}		K_{min}		E_{1-3}	E_{1-2}
								D	I	D	I		
2	32	7	7112 (802)	1.010 (0.007)	1.017 (0.006)	1.027 (0.011)	0.282 (0.210)	194	,4	306	,78	10	20
4	46	11	2560 (328)	1.014 (0.005)	1.029 (0.005)	1.043 (0.006)	0.346 (0.191)	177	,21	5	,67	5	14
5	46	17	2242 (274)	1.007 (0.003)	1.023 (0.006)	1.030 (0.007)	0.532 (0.207)	149	,5	10	,82	6	36
19	24	9	2364 (373)	1.009 (0.005)	1.016 (0.004)	1.025 (0.004)	0.266 (0.334)	67	,4	169	,71	8	46
28	41	12	9493 (897)	1.035 (0.007)	1.114 (0.016)	1.153 (0.014)	0.266 (0.334)	17	,25	214	,64	10	29
36	39	13	2222 (554)	1.013 (0.008)	1.020 (0.006)	1.034 (0.007)	0.223 (0.374)	62	,23	201	,59	18	34
41	64	12	3469 (525)	1.047 (0.021)	1.149 (0.036)	1.203 (0.025)	0.492 (0.235)	266	,9	13	,60	12	56
42	64	6	4858 (386)	1.060 (0.019)	1.136 (0.019)	1.204 (0.022)	0.379 (0.156)	164	,18	3	,70	5	15
45	59	9	3469 (356)	1.032 (0.009)	1.144 (0.019)	1.180 (0.019)	0.622 (0.098)	301	,2	41	,78	3	32
47	19	11	6514 (693)	1.016 (0.006)	1.025 (0.007)	1.042 (0.006)	0.196 (0.292)	291	,12	159	,72	5	14
50	19	14	9149 (539)	1.009 (0.004)	1.041 (0.004)	1.050 (0.005)	0.644 (0.149)	105	,7	272	,82	6	16
52	32	14	4247 (558)	1.005 (0.003)	1.015 (0.005)	1.020 (0.005)	0.479 (0.272)	224	,18	75	,69	5	28
53	32	10	1059 (216)	1.009 (0.004)	1.043 (0.008)	1.052 (0.008)	0.655 (0.144)	326	,7	88	,76	6	40
54	32	10	4906 (464)	1.008 (0.003)	1.016 (0.005)	1.024 (0.007)	0.362 (0.182)	222	,11	55	,78	6	19
55	27	11	6838 (379)	1.011 (0.006)	1.014 (0.006)	1.025 (0.004)	0.147 (0.416)	174	,8	72	,64	6	14
56	27	10	4052 (345)	1.007 (0.006)	1.016 (0.005)	1.023 (0.005)	0.387 (0.336)	256	,14	51	,74	10	14
57	27	11	7592 (391)	1.008 (0.004)	1.027 (0.006)	1.035 (0.006)	0.550 (0.204)	207	,10	95	,64	5	24
58	16	10	4071 (391)	1.012 (0.006)	1.025 (0.012)	1.037 (0.015)	0.327 (0.375)	269	,1	4	,85	10	50
60	16	12	7434 (613)	1.015 (0.006)	1.026 (0.007)	1.042 (0.007)	0.273 (0.267)	276	,7	131	,81	9	38
61	26	7	8332 (714)	1.014 (0.009)	1.036 (0.015)	1.050 (0.011)	0.425 (0.442)	64	,4	204	,84	5	19
66	42	7	4001 (476)	1.013 (0.009)	1.031 (0.011)	1.044 (0.008)	0.411 (0.387)	212	,20	32	,69	8	47
70	41	35	11454 (859)	1.035 (0.012)	1.116 (0.014)	1.155 (0.015)	0.531 (0.150)	60	,18	231	,72	7	11
79	39	8	13738 (510)	1.024 (0.008)	1.112 (0.011)	1.138 (0.013)	0.634 (0.111)	102	,13	314	,74	3	6
80	39	18	14839 (1004)	1.025 (0.006)	1.118 (0.016)	1.146 (0.015)	0.632 (0.090)	90	,5	224	,82	4	18
81	39	11	11014 (492)	1.015 (0.007)	1.107 (0.011)	1.123 (0.014)	0.753 (0.107)	297	,23	139	,65	6	18
83	38	8	13862 (415)	1.036 (0.008)	1.089 (0.011)	1.128 (0.010)	0.416 (0.113)	40	,7	266	,80	14	22
84	38	14	12825 (522)	1.030 (0.009)	1.100 (0.012)	1.133 (0.010)	0.523 (0.142)	88	,14	238	,73	5	11
87	33	12	3900 (198)	1.011 (0.006)	1.023 (0.005)	1.035 (0.005)	0.363 (0.268)	114	,17	288	,73	7	14
88	33	9	4126 (402)	1.009 (0.006)	1.019 (0.006)	1.028 (0.009)	0.430 (0.324)	114	,28	266	,59	10	22
97	26	12	6074 (427)	1.005 (0.003)	1.027 (0.004)	1.032 (0.006)	0.707 (0.145)	216	,4	79	,84	7	53
98	32	8	7580 (241)	1.010 (0.005)	1.024 (0.006)	1.035 (0.005)	0.396 (0.271)	30	,21	233	,67	4	26
99	37	14	6943 (344)	1.012 (0.005)	1.050 (0.006)	1.063 (0.005)	0.619 (0.152)	28	,17	231	,71	3	11
100	37	10	6220 (223)	1.012 (0.005)	1.040 (0.005)	1.052 (0.006)	0.543 (0.155)	85	,11	264	,78	5	13
104	20	14	5886 (326)	1.012 (0.003)	1.033 (0.004)	1.045 (0.003)	0.473 (0.151)	25	,6	158	,81	5	12
105	19	7	8464 (461)	1.008 (0.004)	1.036 (0.006)	1.044 (0.005)	0.649 (0.175)	202	,1	98	,87	2	14

Table 5.1 - Mean anisotropy factors for each site (standard deviation in parenthesis). dist: distance from the caldera topographic rim; N: measured samples; K_m : (k_{max} +k_{int} +k_{min})/3 (magnetic susceptibility, in 10^{-6} SI units); L: lineation (k_{max}/k_{int}); F: foliation (ki_{nt}/k_{min}); P: anisotropy degree (k_{max} /k_{min}); T: shape parameter ($2\eta_2 - \eta_1 - \eta_3$)/($\eta_1 - \eta_3$), where $\eta_2 = lnk_{int}$; $\eta_1 = lnk_{max}$; $\eta_3 = lnk_{min}$; D: azimuth; I: inclination; E_{1-3}, E_{1-2}: semi-angles of the 95% confidence ellipses around the principal susceptibility axes.

specimen	% para	% ferro	para K max		para K min		ferro K min		ferro K max		KLY-3 K max		KLY-3 K min	
			D	I	D	I	D	I	D	I	D	I	D	I
41_03A	77	23	269	34	36	42	37	43	270	33	283	28	38	39
41_07A	72	28	155	29	360	58	347	61	144	27	162	36	342	54
42_10A	71	29	167	19	335	71	332	70	168	20	160	21	325	68
45_10	77	23	141	2	266	86	240	85	334	0	342	4	225	82
47_09B	67	33	300	27	110	63	109	59	301	30	300	30	103	59
50_01A	68	32	116	11	244	72	246	71	113	13	109	14	277	76
50_04B	73	27	345	0	252	81	254	80	145	3	27	4	262	83
53_01	84	16	305	2	44	79	29	79	295	1	289	2	31	80
53_02	84	16	347	3	88	73	255	13	73	77	357	0	88	73
53_05A	86	14	345	5	92	74	87	77	351	2	343	9	123	78
53_05B	86	14	262	14	108	74	132	84	279	5	244	13	105	74
55_03A	68	32	178	3	75	78	56	81	178	5	183	5	25	84
56_02	71	29	253	19	26	64	13	61	252	16	251	19	16	59
56_05	77	23	161	9	41	72	9	75	162	14	166	11	25	76
61_01	66	34	56	12	182	70	169	66	57	10	59	9	171	66
70_01A	72	28	72	17	293	68	296	68	72	16	75	9	283	80
70_16A	73	27	43	19	231	71	235	72	136	3	53	16	239	73
97_03B	70	30	209	0	119	80	217	5	308	12	219	2	118	77
97_07B	71	29	187	9	16	81	23	78	162	9	319	0	51	83
100_08A	72	28	106	6	0	68	4	69	98	2	86	16	238	72
105_01A	68	32	214	0	118	86	97	89	211	1	212	4	67	85
105_01B	70	30	251	25	24	55	23	53	267	18	294	6	141	83

Table 5.2 High field anisotropy results for selected sites. Specimens are identified by site number, core number and specimen (letter). Para: paramagnetic; ferro: ferromagnetic; LF: low field AMS results.

Appendix I

unit	sample	litho	single comp	2 comp		class	T_{ub} (°C)
				LT	HT		
Blanco	02111	ppd	n			A	>580
	02112	ppd	n			A	>580
	02113	ppd	n			A	>580
	02114A	ppd	n			A	>580
	02114B	ppd	n			A	>580
	02115	ppd	n			A	>580
	02116	ppd	n			A	>580
Lower Merihuaca	02121	ppd		n	rand	B	580-600
	02122	ppd	n			A	>630
	02123	ppd	n			A	>580
	02124	ppd	n			A	>580
	02125	ppd	n			A	>630
	02126	ppd		n	rand	B	580-600
	07301	ppd		n	rand	B	590-610
	07302	ppd	n			A	>530
	07303	ppd	n			A	>560
	07305	ms		n	rand	B	590-610
	07306	ppd		n	rand	B	590-610
	07307	ppd		n	rand	B	590-610
	07308	ppd	n			A	>560
	07309	ppd		n	rand	B	590-610
	07310	ppd	n			A	>610
	07311	ppd		n	rand	B	590-610
Upper Merihuaca	01611	lava	n			A	>580
	01612	lava	n			A	>580
	01614	lava	n			A	>580
	01615	lava	n			A	>580
	01616	ppd	n			A	>580
	01621	lava	n			A	>580
	01625	lava	r			A	>580
	02131	ppd	\	\	\	\	\

unit	sample	litho	single comp	2 comp		class	T_{ub} (°C)
				LT	HT		
Middle Merihuaca	02132	ppd		n	rand	B	360-480
	02133	ppd	n			A	>580
	02134	ppd	n			A	>600
	02135	ppd	n			A	>580
	02136	ppd	n			A	>580
	02211		n			A	>600
	02213	ppd	n			A	>580
	02214	ppd	n			A	>580
	07401	bppd	n			A	>560
	07402	ig	n			A	>560
	07403	ppd	n			A	>610
	07404	ppd	n			A	>610
	07405	ppd	n			A	>610
	07406	ppd	n			A	>610
	07407	ppd	n			A	>610
	07408	ig	n			A	>590
	07409	ig	n			A	>590
	07410	ppd	n			A	>610
Upper Merihuaca	02141	\	\	\	\	\	\
	02142	riolite	r			A	>480
	02143	ppd	r			A	>580
	02146	ppd	r			A	>580
	02222	ppd	r			A	>620
	02223	ppd	r			A	>580
	02225	ppd	r			A	>580
	02226	ppd	\	\	\	\	\
	02313	ppd	r			A	>620
	02314	ppd	r			A	>580
	02315	ppd	r			A	>580
	02316	ppd	\	\	\	\	\

Appendix I (continued)

unit	sample	litho	single comp	2 comp		class	T_{ub} (°C)
				LT	HT		
Upper Merihuaca	07501	ppd	n			A	>610
	07502			r	rand	B	530-560
	07503	mvo	\	\	\	\	\
	07504	mvo	r			A	>340
	07505	mvo	r			A	>460
	07506		r			A	>590
	07507		r			A	>420
	07508		r			A	>590
Pitas	02151		n			A	>600
	02152	ppd	n			A	>600
	02153	ppd	n			A	>580
	02154		n			A	>600
	02155		n			A	>600
	02156		n			A	>580
	02411	ppd	n			A	>620
	02412	ppd	n			A	>620
	02413	ppd	n			A	>580
	02414	ppd	n			A	>580
	02415	ppd	n			A	>580
	02416		n			A	>580
	02511	ppd	r			A	>620
	02512		n			A	>580
	02513	ppd	n			A	>600
	02516		n			A	>580
	07701	ppd	n			A	>610
	07702	ppd	n			A	>590
	07703	ppd	n			A	>590
	07704	ppd	n			A	>590
	07705	ppd	n			A	>560
	07706	ppd	n			A	>590
	07707	ppd	n			A	>560
	07708	ppd	n			A	>590
Pitas	07801	ppd	n			A	>610
Real Grande	01712	ppd	n			A	>580
	01722	ppd	n			A	>580
	01921	fms	n			A	>580
	01925	ppd	n			A	>580
	02611	ppd	n			A	>480
	02612	ppd	n			A	>580
	02613	ppd	n			A	>580
	02621	ppd	n			A	>600
	02622	ppd	n			A	>600
	02623	ppd	n			A	>520
	02624	ppd	n			A	>620
	02625	ppd	n			A	>600
	02626	ppd	n			A	>580
	02631	ppd	r			A	>580
	02632	ppd	n			A	>580
	02633	ppd	n			A	>600
	03021	ppd	n			A	>580
	03026	ppd	n			A	>580
	03031	ppd	n			A	>580
	03052	ppd	n			A	>580
	06201	ms	n			A	>600
	06202	ppd	n			A	>600
	06204	ppd	n			A	>630
	06205	fms	n			A	>630
	06207	ppd	n			A	>600
	06208	ppd	n			A	>600
Vega	02641	ppd	r			A	>520
	02642	ppd	r			A	>520
	02643		r			A	>560
	02644		r			A	>530
	02645		r			A	>530

Appendix II

sample	litho	single comp	2 comp		class	T_{ub} (°C)	sample	litho	single comp	2 comp		class	T_{ub} (°C)
			LT	HT						LT	HT		
00121	ppd	r			A	>610	02012B	mvo	\	\	\	\	\
00122	ppd	r			A	>580	02013	mvo	\	\	\	\	\
00131	ppd	r			A	>580	02014A	qz	r			A	>550
00132	ppd	r			A	>580	02014B	qz	\	\	\	\	\
00133	ppd	r			A	>580	02015	mvo	\	\	\	\	\
00211	ppd	r			A	>520	02016	mvo	r			A	>550
00312	lava	r			A	>520	02017	mvo	r			A	>600
00313	lava	r			A	>520	02021	mvo	r			A	>550
00314	lava	r			A	>520	02022	mvo	r			A	>580
00315	mvo	r			A	>520	02024	fms	r			A	>440
00316	lava	r			A	>520	02025	fms	r			A	>580
00321	mvo	r			A	>580	02026	mvo	r			A	>580
00322	mvo	r			A	>520	02031	mvo	r			A	>580
00323	lava	r			A	>520	02032	\	r			A	>580
00324	lava	r			A	>520	02034	\	r			A	>580
00331	lava	r			A	>520	02035	qz	n			A	>550
00332	lava	r			A	>520	02036A	\	r			A	>580
00333	lava	r			A	>520	02036B	\	r			A	>580
00334	lava	r			A	>520	02037	mvo	r			A	>580
00335	lava	r			A	>600	02039	mvo	r			A	>580
00336	lava	r			A	>520	02041	ms	n			A	>580
00342	amph	r			A	>520	02042	ms	r			A	>580
00343	\	r			A	>520	02043	ms	r			A	>520
00344	amph	r			A	>520	02051	mvo	/	/	/	/	/
00351	lava	r			A	>520	02052	mvo	r			A	>580
00352	mvo	\	\	\	\	\	02053	mvo	r			A	>550
00353	lava	r			A	>520	02711	mvo	r			A	>580
00415	lava	r			A	>580	02712	mvo	r			A	>580
00422	ms	r			A	>520	02713	mvo	r			A	>550
00511	qbs	r			A	>580	02714	mvo	r			A	>580
00514	ms	r			A	>580	02721	mvo	r			A	>550
00515	mvo	r			A	>580	02723	mvo	r			A	>600
02011	lava	r			A	>600	02724	mvo	r			A	>600
02012	mvo	r			A	>600	02725	mvo	r			A	>580

Appendix II (continued)

sample	litho	single comp	2 comp		class	T_{ub} (°C)	sample	litho	single comp	2 comp		class	T_{ub} (°C)
			LT	HT						LT	HT		
02811	fms	r			A	>520	03426	mvo	r			A	>600
02812	mvo	r			A	>580	03431	lava	r			A	>580
02813	mvo	r			A	>620	03432	ppd	r			A	>580
02814	mvo	r			A	>550	03433	lava	r			A	>580
02815A	mvo	r			A	>600	03435	\	r			A	>520
02815B	mvo	r			A	>600	03436	\	\	\	\	\	\
02816	mvo	r			A	>600	03441	ppd	r			A	>580
02821	fms	\	\	\	\	\	03442	ppd	r			A	>580
02822	mvo	r			A	>580	03443	ppd	r			A	>580
02823	fms	r			A	>520	03444	ppd	r			A	>550
02824	mvo	r			A	>520	03511	mvo	r			A	>580
02825	mvo	r			A	>520	03513	ppd	r			A	>610
02826	mvo	r			A	>580	03514	ppd	r			A	>610
02831	mvo	\	\	\	\	\	03515	mvo	r			A	>580
02832	mvo	\	\	\	\	\	03516	ppd	r			A	>610
02833	mvo	\	\	\	\	\	03521	ppd	r			A	>580
02834	fms	\	\	\	\	\	03522	ppd	r			A	>610
02835	mvo	\	\	\	\	\	03523	ppd	r			A	>580
02836	ppd	r			A	>580	03524	ppd	r			A	>580
02841	ig	r			A	>580	03525	ppd	r			A	>580
02842	mvo	r			A	>580	03526	ppd	r			A	>550
02843	mvo	n			A	>580	03531	ppd	r			A	>610
02852	mvo	r			A	>520	03532	ppd	r			A	>610
02853	\	r			A	>580	03533	ppd	r			A	>580
02854	\	\	\	\	\	\	03711	mvo	r			A	>550
02855	\	\	\	\	\	\	03712	mvo	r			A	>580
02856	\	r			A	>600	03713	mvo	r			A	>550
03421	ppd	\	\	\	\	\	03716	mvo	r			A	>550
03422	ppd	\	\	\	\	\	03721	mvo	r			A	>550
03423	ppd	\	\	\	\	\	03722	ppd	r			A	>610
03424	ppd	\	\	\	\	\	03731	ppd	r			A	>520
03425	bppd	r			A	>580	03732	ppd	r			A	>580

Appendix II (continued)

sample	lithology	single component	2 components LT polarity	2 components HT polarity	class	T (°C)
03733	ppd	r			A	>520
03734	ppd	\	\	\	\	\
03735	ppd	r			A	>550
03741	mvo	r			A	>630
03742	mvo	\	\	\	\	\
03743	mvo	\	\	\	\	\
03744	mvo	r			A	>580
03745	mvo	\	\	\	\	\
03811	gms	r			A	>600
03812	gms	r			A	>550
03813	ppd	r			A	>550
03814	gms	r			A	>600
03821	\	r			A	>550
03822	qbs	\	\	\	\	\
03823	qbs	r			A	>550
03824	qbs	r			A	>550
04201	ms				A	>580
04205	gr	\	\	\	\	\
04206	gr	r			A	>630
04207	gr	r			A	>650
04301	gr	r			A	>560
04302	gr	r			A	>560
04303	gr	r			A	>560
04304	gr	r			A	>560
04305	gr	r			A	>600
04308	gr	\	\	\	\	\
04401	ppd	r			A	>560
04402	ppd	r			A	>560
04404	ppd	r			A	>600
04405	ppd	r			A	>600
04406	ppd	r			A	>560
04407	ppd	r			A	>560
04409	spatterlike	r			A	>560
04410	ppd	r			A	>600
04601	fms	r			A	>600
04602	fms	r			A	>600
04603	ppd	r			A	>560
06601	bppd	r			A	>550
06602	bppd	r			A	>550
06603	bppd	r			A	>550
06604	bppd	r			A	>550
06606	bppd	r			A	>550
06607	bppd	r			A	>550
06608	bppd	r			A	>600